


NUREG/CR-3589 (2 of 4)  
SAND83-2425 (2 of 4)  
R3 and R7  
Printed July 1984

# Reactor Safety Research Quarterly Report April-June 1983 Volume 26

Reactor Safety Research Department 6420

Prepared by  
Sandia National Laboratories  
Albuquerque, New Mexico 87185 and Livermore, California 94550  
for the United States Department of Energy  
under Contract DE-AC04-76DP00789



Prepared for  
**U. S. NUCLEAR REGULATORY COMMISSION**

SF29000 (8-81)

8409180443 840731  
PDR NUREG  
CR-3589 R PDR

**NOTICE**

This report was prepared as an account of work sponsored by an agency of the United States Government. Neither the United States Government nor any agency thereof, or any of their employees, makes any warranty, expressed or implied, or assumes any legal liability or responsibility for any third party's use, or the results of such use, of any information, apparatus product or process disclosed in this report, or represents that its use by such third party would not infringe privately owned rights.

Available from  
GPO Sales Program  
Division of Technical Information and Document Control  
U.S. Nuclear Regulatory Commission  
Washington, D.C. 20555

and

National Technical Information Service  
Springfield, Virginia 22161

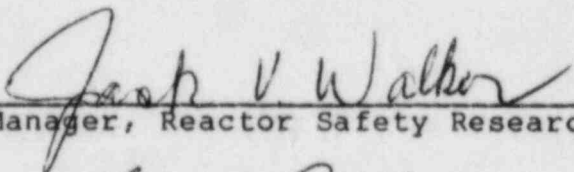
NUREG/CR-3589 (2 of 4)  
SAND83-2425 (2 of 4)  
Vol. 26  
R3 and R7

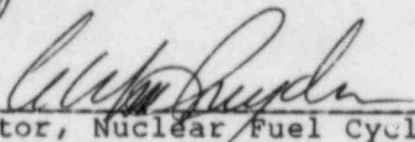
REACTOR SAFETY RESEARCH  
QUARTERLY REPORT  
April-June 1983

Reactor Safety Research Program  
Sandia National Laboratories  
Albuquerque, NM 87185

Printed: July 1984

APPROVED:

  
\_\_\_\_\_  
Manager, Reactor Safety Research

  
\_\_\_\_\_  
Director, Nuclear Fuel Cycle Programs

Sandia National Laboratories  
Albuquerque, New Mexico 87185  
operated by  
Sandia Corporation  
for the  
U.S. Department of Energy

Prepared for  
Division of Accident Evaluation  
Office of Nuclear Regulatory Research  
U.S. Nuclear Regulatory Commission  
Washington, DC 20555

Under Memorandum of Understanding DOE 40-550-75  
NRC FIN Nos.

(A-1016, A-1021, A-1054, A-1172, A-1179, A-1181, A-1182,  
A-1183, A-1198, A-1218, A-1219, A-1227, A-1247, A-1262,  
A-1263, A-1264, A-1333, A-1335, A-1340, A-1341, A-1342,  
A-1344, A-1346, A-1356, A-1361, A-1362, A-1368)

## FOREWORD

Sandia National Laboratories is conducting, under USNRC's sponsorship, phenomenological research related to the safety of commercial nuclear power reactors.

The overall objective of this work is to provide NRC a comprehensive data base essential to (1) defining key safety issues, (2) understanding risk-significant accident sequences, (3) developing and verifying models used in safety assessments, and (4) assuring the public that power reactor systems will not be licensed and placed in commercial service in the United States without appropriate consideration being given to their effects on health safety.

Together with other programs, the Sandia effort is directed at assuring the soundness of the technology base upon which licensing decisions are made.

This report describes progress in a number of activities dealing with current safety issues relevant to both light water and breeder reactors. The work includes a broad range of experiments to simulate accidental conditions to provide the data base required to understand important accident sequences and to serve as a basis for development and verification of the complex computer simulation models and codes used in accident analysis and licensing reviews. Such a program must include the development of analytical models, verified by experiment, which can be used to predict reactor and safety system performance under a broad variety of abnormal conditions.

Current major emphasis is focused on providing information to NRC relevant to (1) its deliberations and decisions dealing with severe LWR accidents and (2) its safety evaluation of the proposed Clinch River Breeder Reactor.

## CONTENTS

	<u>Page</u>
1. Core Debris Behavior	15
1.1 Ex-Vessel Core Debris Interaction	15
1.2 Core Retention Materials Assessment	21
1.3 Sodium Containment and Structural Integrity	24
1.4 Debris Bed Coolability	27
1.5 Dry Debris Melt Progression	31
1.6 References	45
2. High-Temperature Fission-Product Chemistry and Transport	46
3. Containment Analysis	57
3.1 CONTAIN Code Development	58
3.2 CONTAIN Testing and Validation	64
3.3 Clinch River Containment Analysis	66
3.4 LWR Containment Analysis	69
3.5 References	75
4. Elevated Temperature Materials Assessment	76
5. Advanced Reactor Accident Energetics	78
5.1 Initiation Phase	78
5.2 Transition Phase	90
5.3 References	121
6. LWR Damaged Fuel Phenomenology	122
6.1 Melt Progression Phenomenology	123
6.2 LWR Fuel Damage Experiment	125
6.3 LWR Degraded-Core Coolability	130
6.4 References	153
7. Test and Facility Technology	154
7.1 ACRR Status	154

## ILLUSTRATIONS

<u>Figure</u>		<u>Page</u>
1.1-1	Pressure Record from Cavity Transducer (SPIT-17 Test)	19
1.4-1	Instrument Layout of the D10/D13 Experiments	29
1.5-1	Dry Capsule Test Configuration	32
1.5-2	Schematic of DC 1	33
1.5-3	DC 1 Bed Instrumentation	34
1.5-4	DC 1 Reactor Power	39
1.5-5	DC 1 Thermocouple Data	40
1.5-6	Ultrasonic Thermometer Data	41
1.5-7	DC 1 UT1 Temperature Data	42
2.1-1	Reaction Tube in the Fission-Product Reaction Facility	48
2.2-1	Cesium Levels Measured by Electron Microprobe and X-ray Fluorescence on 304 SS Surfaces (Test 15)	50
2.2-2	Electron Microprobe Scans on Coupon 15.13 for Manganese, Nickel, Phosphorous, and Cesium	51
2.2-3	Cesium Levels Measured by Electron Microprobe and X-ray Fluorescence on 304 SS Surfaces (Test 10)	53
2.2-4	Cesium Levels Measured by Electron Microprobe and X-ray Fluorescence on 304 SS Surfaces (Test 19)	55
5.1-1	Schematic of STAR Capsule and Hardware	80
5.1-2	Image of Fuel Pin as Seen from the Camera	82
5.1-3	Multipin Geometries	87
5.1-4	Axial Energy Deposition Profile	88
5.1-5	Radial Energy Deposition Profile	89

ILLUSTRATIONS (continued)

<u>Figure</u>		<u>Page</u>
5.2-1	Blockages Observed in TRAN-2	91
5.2-2	Fuel Crust near the Channel Entrance of TRAN-2	93
5.2-3	Relative Fuel Distribution Data for 0° for TRAN B-1	94
5.2-4	Radiograph of the Channel for TRAN B-1	96
5.2-5	Finite Differential Mesh Used in PLUGM-II Calculations	100
5.2-6	Molten Fuel Slug Position as a Function of Time (15% Film-Deposition Case)	104
5.2-7	Leading-Edge Velocity as a Function of Time (15% Film-Deposition Case)	104
5.2-8	Molten Fuel Slug Position as a Function of Time (25% Film-Deposition Case)	105
5.2-9	Leading-Edge Velocity as a Function of Time (25% Film-Deposition Case)	105
5.2-10	Final Axial Crust Distribution (15% Film-Deposition Case)	106
5.2-11	Final Axial Crust Distribution (25% Film-Deposition Case)	106
5.2-12	Schematic of the GAP Experiment Package	108
5.2-13	Fuel Melting Section of the GAP Experiment	111
5.2-14	Fuel Freezing Channel of the GAP Experiment (Schematic)	113
5.2-15	Pressure Systems To Be Used in the TRAN GAP Experiment Package	115
5.2-16	Radial Fission Energy Deposition Profile (Normalized) through the Annular Fuel Element	117
5.2-17	Radial Thermal Profiles Characterizing the Two-Pulse Strategy	118

ILLUSTRATIONS (continued)

<u>Figure</u>		<u>Page</u>
6.3-1	DCC-1 Thermocouple Locations	132
6.3-2	Internal Energy of the DCC-1 Primary System	134
6.3-3	Primary and Secondary Internal Energies during Adiabatic Blowdown	136
6.3-4	A Schematic of the Bed Crucible Showing the Placement of Thermocouples and Flow Passageways	143
6.3-5	Schematic of the Experiment Capsule	150

TABLES

<u>Table</u>		<u>Page</u>
1-I	Description of Thermocouples for DC 1	36
1-II	Description of Ultrasonic Thermometers	37
1-III	Steady-State Maximum Temperatures	37
1-IV	Steady-State Thermocouple Data	43
1-V	Steady-State UT Temperature Data	44
5-I	Instrumentation for the STAR Experiments	84
5-II	Coupling Factors for 40% and 67% Enriched UO <sub>2</sub>	86
5-III	Properties of Suitable Tagging Elements	98
5-IV	Range of Experimental Parameters	110
6-I	Bed Thermocouple Locations for DCC-1	131



## EXECUTIVE SUMMARY

### 1. CORE DEBRIS BEHAVIOR

#### 1.1 EX-VESSEL CORE DEBRIS INTERACTIONS

If core debris formed during a severe reactor accident is not coolable, the debris will penetrate the reactor vessel and interact with structural material in the reactor cavity. This interaction could lead to gas generation, production of flammable species, and intense emission of radioactive aerosols, in addition to erosion of the reactor basemat. Study of the phenomena associated with ex-vessel interaction of core debris with structural material found in the reactor cavity is the purpose of the Ex-Vessel Core Debris Interactions program. In the recent past, the major part of this program was the study of core debris interaction with concrete. Penetration of core debris through steel liners has also been examined. Other associated phenomena are currently undergoing study.

Two experiments in the System Pressure Injection (SPIT) test matrix have been performed to study the interaction of a high-velocity melt jet and a simulated "water-locked" reactor cavity. The objective of the first test (SPIT-15) was to verify the existence of the steam bubble phenomenon described in the Zion Probabilistic Safety Study (ZPPS). However, the test yielded no energetic interaction between water and the melt, and the steam bubble phenomenon did not occur. The second test (SPIT-17) used a scale model of the Zion cavity to determine the extent of water voiding. Test results show a strong interaction between the melt jet and the water pool and imply that the confinement provided by the structure may influence the magnitude of propagating interactions.

The Transient Urania Concrete (TURC) tests have been initiated to investigate large-scale oxide melt interactions with concrete. They will provide a new data base to be used in conjunction with previous steel/concrete interactions to form comparisons with current models. The experiments will assess various source terms, such as energy partitioning, gas generation rates, combustible gas production, aerosols, and fission-product transport, that may pose a threat to containment. During this quarter, a test matrix was defined for three upcoming TURC tests.

#### 1.2 CORE RETENTION MATERIALS ASSESSMENT

The Core Retention Materials Assessment program is an effort to identify the difficulties and utility of incorporating core retention devices in reactor cavity regions to mitigate the consequences of ex-vessel core-debris interactions. A major goal of this program is the establishment of the Large-Scale Melt Facility (LMF) that allows tests of

## EXECUTIVE SUMMARY

candidate designs exposed to melts of up to 500 kg of fuel oxides. Initial work in this program focuses on final development of the LMF and the engineering of magnesia bricks for core-retention devices and the conceptual development of the thoria rubble-bed core-retention device.

A large-scale test of molten  $UO_2-ZrO_2$  interactions with a magnesium-brick core-retention device was conducted with the LMF. The total weight of the melt was 230 g. A preliminary review of the data and results has been initiated, and indicates that aerosol and gas emission was quite small.

### 1.3 SODIUM CONTAINMENT AND STRUCTURAL INTEGRITY

The Sodium Containment and Structural Integrity program is an investigation of safety phenomena that will develop should molten sodium contact structural or shielding concrete during a reactor accident. Quantitative evaluation of these phenomena, leading to the development of models for use in predicting the ways in which these phenomena might threaten the reactor containment, is a major goal of this program. Quantitative evaluation of structural flaws in reactor cell liners is also sought in this program because these flaws can provide pathways for sodium to contact concrete.

Work during the quarter in the Sodium Containment Structural Integrity program concentrated on documentation of the past research efforts. A topical report describing the computer model of sodium/concrete interactions, SLAM, developed in this program was begun.

Work was initiated on an experimental program to characterize fission-product release during sodium/concrete interactions. A factorial matrix design to study the release of U, Ce, I, Cs, Ba, Te, Zr, Nb, Ru, and La as a function of time, temperature, gas sparging rate and NaOH content of the system has been defined. The test scheme should yield engineering data spanning the parameter range believed to be important and still provide data of sufficient quality for more fundamental model development.

### 1.4 DEBRIS BED COOLABILITY PROGRAM

The objective of the experimental studies of debris beds is to provide information on the behavior of reactor materials following a core-melt accident. In particular, it is necessary to determine if the heat generated by fuel particles after meltdown (decay heat) is satisfactorily dissipated by the coolant; if not, the dynamics of remelt and containment damage must be ascertained. Sandia's debris bed studies consist of a series of experiments using liquid sodium and

## EXECUTIVE SUMMARY

urania to serve as a basis for developing phenomenological models. The experiments are fission-heated in the ACRR to simulate fission-product heating in a debris bed. Results are sufficiently general to be applicable to all liquid-cooled reactor systems.

Debris Bed Experiment D10 is the first experiment designed to study the coolability of particle beds that are cooled by both overlying sodium and structures that support the bed from below. Maximum debris temperatures in excess of 2773 K (2500°C) are planned during the experiment to investigate the phenomena that may occur with relatively large dry zones at elevated temperatures.

A program review meeting was held in April, and the D10 experiment design, instrumentation, design analysis, operating procedures, and the crucible material compatibility program results were reviewed. The results of the materials testing indicated that none of the three candidate materials were affected by sodium exposure. However, more tests will be run to investigate temperature conditions not previously explored. A crucible material was chosen, and investigations are pending for this material's welding feasibility. Structure temperatures around the crucible were determined by two-dimensional-thermal analysis and will be used in the stress analysis. Testing of the ultrasonic thermometer continued, using thoria insulator material. Component fabrication continued with drawings being prepared. A description of experiment components was included in the safety evaluation, which is also in preparation.

### 1.5 DRY DEBRIS MELT PROGRESSION

After a major reactor accident, if the core-material debris is uncoolable it will progress to a molten state. The progression of the debris to a molten state and the interaction of the core melt with structural and core retention material are being investigated experimentally in the Dry Debris Melt Progression program. This program, the follow-on to the Molten Pool Studies, interfaces closely with both the Ex-Vessel Core Debris Interactions and the Debris Bed Coolability programs. High-temperature, laboratory-furnace tests and the first-of-a-kind, neutronically heated experiments are providing significant data on many coolability-related issues, including the thermal response of dry  $UO_2$  and steel particulate beds to internal heating, the formation of crusts and voids in pools of internally heated molten fuel material, and the interaction of hot fuel debris with core structure and retention material. As with other safety research programs, investigators are using the experimental results to develop

## EXECUTIVE SUMMARY

and verify analytical models that will be used to study reactor behavior under a wide variety of accident conditions.

The DC 1 experiment completed this quarter was the first fission-heated dry  $UO_2$  debris bed that achieved a sizeable urania molten pool (0.8 kg) at steady-state conditions. Steady conditions at several powers less than required for melt were also achieved. The purpose of the experiment was to obtain information on high-temperature dry debris heat transfer rates, melt formation, melt migration, and melt heat transfer rates. The data will be used for analysis and model development on coolability and melt behavior of the dry portion of reactor debris for LMFBR accident codes. These data also have applications to light water reactor (LWR) severe accident debris coolability.

### 2. HIGH-TEMPERATURE FISSION-PRODUCT CHEMISTRY AND TRANSPORT

The purpose of the High-Temperature Fission-Product Chemistry and Transport program is to obtain data on the chemistry and processes that affect the transport of fission products under accident conditions. An experimental facility has been built to allow the chemistry of fission products in prototypic steam-hydrogen environments to be studied. The interaction of fission products with reactor materials such as stainless steel is also examined. Results of these experimental studies are compared to predictions of thermochemical models to determine if reaction kinetics play an important role in fission-product transport.

The experiment series to examine the behavior of tellurium vapor over reactor materials continued with the first test to study the reaction of tellurium with stainless steel in a steam-hydrogen environment. The goal is to determine to what extent the presence of steam affects the rate at which tellurium reacts and the importance of temperature and environment on decomposition of the tellurides. Preliminary posttest analysis indicates that the tellurium did not react with the oxidized alloy. Additional analysis of the oxide layer of the alloy in cross section will be further examined for the presence of tellurium.

Analysis continued on the completed test series of  $CsOH$  or  $CsI$  reactions with stainless steel and Inconel in a steam-hydrogen environment. The surface composition of the oxide formed on the alloys had been altered by the presence of  $CsOH$  and  $CsI$  vapors. Some features of the reactions have been studied by electron microprobe and X-ray fluorescence. Detailed results are presented in the main text of this report.

## EXECUTIVE SUMMARY

### 3. CONTAINMENT ANALYSIS

The goal of this task is the development of CONTAIN, a general and comprehensive systems code that will analyze a variety of accident sequences following the breach of the primary containment vessel through the breach of the secondary containment. The code will provide detailed treatments of phenomena such as material interactions, heat transfer, aerosol behavior, and fission-product transport. The models will be sufficiently general to apply to all advanced reactor and LWR containment systems.

The testing and validation of CONTAIN continues. The current version of the CONTAIN code is being evaluated against the performance of previous versions. Of the numerous tests that have been used to test and validate the response of the code in the past, certain ones have been selected and designated as "standard tests." These standard tests are intended to be a routine quality control procedure to check new revisions of the code.

The report describing the results of the CONTAIN test efforts has been completed in final form. All outstanding test reports were received and incorporated into the overall report.

Representatives of the University of Wisconsin (UW) and Sandia met in Madison, WI to discuss progress on the coding of the MEDICI LWR cavity model. Most of the features needed for the first version of MEDICI are either operational or are expected to be operational by August 1. Modules requiring additional work include the expulsion of debris following a steam explosion, pool-atmosphere coupling, hydrogen generation in the exposed debris zone, and entrainment and sweepout in a high-velocity gas stream.

The process of merging the parts of the code developed at UW and at Sandia will be initiated in July and should be completed during a week-long visit by UW personnel to Sandia in August. Project personnel expect that a version of the code will be available for review by other Sandia organizations around October 1.

The necessary input information was assembled for verifying the Simple Sodium Concrete Interaction (SSCI) code with data from tests AA/AB. CONTAIN input data decks were prepared that model the CRBR melt-through scenario. For checkout purposes, the investigators ran cases where the initial sodium pool temperature was specified to be near the boiling point. Boiling phenomena were initiated early in these problems, exercising more of the code subroutines. This was done to

## EXECUTIVE SUMMARY

evaluate the code's handling of this complex accident scenario. Checks indicated that problems in calculations were occurring once boiling started and that the amount of heat transferred was unrealistically high for the specified atmosphere and pool conditions. The code was modified to correct these problems and the results obtained with this revised coding were much more realistic than those obtained prior to the modifications.

The modifications and improvements to the aerosol module obtained over the past few months were adapted to the most recent version of CONTAIN for incorporation into the new (Mod415) base file.

Aerosol calculations were carried out in support of the upcoming ABCOVE AB-6 experiment. The AB-6 test will be a two-component sodium oxide-sodium iodide experiment designed to differentiate between multicomponent codes like MAEROS and MSPEC, and single-component, multimaterial codes like HAA-4 and NAUA. Scoping calculations that compared the multicomponent treatment and the single-component treatment were carried out using CONTAIN. Project personnel found that under the proposed experimental conditions, significant differences in code predictions should result just from the different treatment of components and that the experiment should satisfactorily demonstrate that the multicomponent treatment is needed.

Condensation of water vapor on aerosols and the subsequent enhanced settling of the aerosols can be a significant decontamination mechanism. For the AB sequences, MARCH (with NAUA) predicts a significant amount of condensation on primary aerosols, whereas CONTAIN presently does not, leading to a substantial difference in the resulting aerosol concentration. Because the rate of condensation of aerosols is a strong function of the (usually small) difference between the actual water vapor pressure and the saturation vapor pressure, relatively small uncertainties in thermal hydraulic effects can result in rather large uncertainties in the condensation on aerosols and the resulting suspended mass of aerosols. A calculation of thermal hydraulic behavior sufficient for assessing the temperature and pressure threat to containment may be insufficient for determining the aerosol behavior. The differences between the MARCH and CONTAIN thermal hydraulic predictions are currently being assessed.

A panel of specialists from various laboratories around the country has been established by NRC's Containment Systems Research Branch to apply current phenomenological understanding to the problem of estimating the range of pressures that can occur in an LWR severe accident. The project is in support of the reassessment of source term estimates, and the

## EXECUTIVE SUMMARY

goal is to provide useful input to the Accident Source Term Project Office (ASTPO) by November 1983 by drawing on resources from a variety of NRC activities. The first Working Group meeting is scheduled for the middle of July.

### 4. ELEVATED TEMPERATURE MATERIALS ASSESSMENT

The primary objectives of the Elevated Temperature Materials Assessment studies are to (1) determine how microstructures evolve due to thermomechanical history that results in mechanical property changes, (2) evaluate the validity of material damage rules used in design, and (3) develop and evaluate nondestructive evaluation techniques.

A computer control program developed for the cooperative study with Oak Ridge National Laboratory (ORNL) on the behavior of stainless steels under nonproportional biaxial stress states was completed and verified for elastic deformation. The program controlled tests in which multiple linear paths in stress space were traced out by varying both axial load and internal pressure.

A member of Sandia's staff visited six European research laboratories to exchange information on elevated deformation behavior studies.

### 5. ADVANCED REACTOR ACCIDENT ENERGETICS

The Advanced Reactor Accident Energetics program addresses the key issues in a core-disruptive accident that determine the progression and severity of the accident for current LMFBR designs. This program involves a series of in-pile experiments and analyses that focus on key phenomena in two general areas:

- a. Initiation Phase - Fuel/Clad Dispersal Experiments
- b. Transition Phase - Fuel Freezing and Streaming Experiments

#### 5.1 INITIATION PHASE

The motion of clad and fuel in the initiation phase of a loss of flow (LOF) accident are important considerations in the subsequent progression of the accident. Early fuel dispersal can lead to neutronic termination while limited dispersal and blockage formation continues the accident into the transition phase and the possibility of further neutronic activity. To obtain data on the important phenomena involved in this phase of an LMFBR accident, the USNRC is sponsoring

## EXECUTIVE SUMMARY

the Sandia Transient Axial Relocation (STAR) experiments in the ACRP test facility.

The STAR experiment program is the follow-on series to the Fuel Disruption (FD) experiments. This in-pile program is intended to extend the technology gained in the FD series to the fundamental issues of axial relocation of fuel and cladding. The STAR tests will subject single and multipin bundles of irradiated mixed oxide fuel to reactor power transients. These transients will reproduce the heating conditions of LOF accidents in an LMFBR. In addition to this experimental work, a major portion of this program will develop or modify existing phenomenological models for fuel and clad relocation as well as verify similar models used in accident analysis codes.

The funding for this program will be cosponsored by the USNRC and the German Nuclear Research Center, KfK. Currently, negotiations are underway to define the extent of the exchange program and to determine specific areas in which each research center can contribute to the program.

Six experiments are tentatively planned for the first phase of this program. The details of the fuel heating conditions have not been specified, but a variety of heating conditions to cover the range of uncertainties for LOF accidents in an LMFBR will be investigated. The first two experiments are scoping experiments that will use fresh  $UO_2$  fuel, and one will use a multipin bundle. The following four experiments will probably be performed with irradiated mixed oxide fuel.

During this report period, the experimental design for the program was completed, and most of the hardware was ordered. The design of the STAR capsule and the scoping calculations used to estimate the necessary thermodynamic and neutronic data required to perform such an experiment are found in the main text of this report.

### 5.2 TRANSITION PHASE

Many current LMFBR core designs are characterized by a relatively low-Na void coefficient and incoherent behavior in the initiation phase. These features generally increase the likelihood of a "transition" or "meltout" phase during a core-disruptive accident. The key questions in the transition phase are whether fuel or clad blockages form, leading to a confined or "bottled" core configuration, and the behavior and reactivity implications of this pool of fuel-steel in the core region if the fuel blockages do lead to this state. The TRAN program addresses the question of fuel-inventory reduction by penetration into upper core structure or through subassembly



## EXECUTIVE SUMMARY

(S/A) gaps to the lower core structure. If deep penetrations occur, nonenergetic shutdown is probable while shallow penetration will lead to a transition phase and the possibility of further energetics. First-of-a-kind in-pile experiments are being conducted to provide data to evaluate the various models describing fuel penetration.

Major activities in the TRAN program this report period included the continuation of posttest examination for the TRAN Series I experiment (TRAN 2) and the TRAN B-Series experiment (B-1). Also during this report period, design of the GAP-Series tests and development of the PLUGM-II code continued.

Posttest examination work was done on the TRAN Series I (TRAN-2) test. TRAN-2 continues to be of special interest because it exemplifies the onset of steel melting, yet does not exhibit the complex behavior found in TRAN-4. Blockages were found containing globules of steel surrounded by  $UO_2$ . Implications are that the trailing blockage had been constrained during freezing by the leading blockage and that steel boiling could have occurred in the low-pressure region at the leading edge of the advancing fuel slug.

Posttest examination work was also done on the TRAN B-Series (B-1) test. Findings suggest that fuel deposition from the vapor state occurred or generation of fine solid fuel powder occurred. Two radiographs were taken, one just after the experiment was performed and one after epoxy was drawn out the channel exit to immobilize debris for transverse sectioning. The results showed a nonuniform axial crust distribution. Transverse cross sections were made through the freezing channel and showed a disrupted crust that was consistent with the radiographs.

Preparations have begun for the TRAN B-2 experiment.

The PLUGM-I code user's manual was completed. Development began on the PLUGM-II code, which is based on a finite-difference solution scheme for the crust growth and wall heatup.

Planning has begun for the TRAN Series III "GAP" experiment design. The TRAN-GAP experiments differ from the previous TRAN Series in that a larger mass of fuel is to be driven downward into a rectangular freezing channel. Design has been completed for the fuel melting section, the freezing channel, and the pressure system.

## EXECUTIVE SUMMARY

### 6. LIGHT WATER REACTOR (LWR) DAMAGED FUEL PHENOMENOLOGY

Sandia's LWR Damaged Fuel Phenomenology program includes analyses and experiments that are part of the integrated NRC Severe Fuel Damage (SFD) Research program. Sandia will investigate, both analytically and in separate-effects experiments, the important "in-vessel" phenomenology associated with severe LWR accidents. This investigative effort will provide for three related research programs, the Melt-Progression Phenomenology (MPP) program, the Damaged Fuel Relocation (DFR) program, and the Damaged-Core Coolability (DCC) program. These programs are key elements in the NRC research effort to provide a data base to assess the progression and consequences of severe core-damaging accidents.

#### 6.1 MELT PROGRESSION PHENOMONOLOGY

The objective of this program is to provide balanced perspectives and capabilities applicable to that phase of severe LWR accidents starting with initial core damage and progressing through to breach of the reactor vessel and discharge of core materials into the containment environment.

The formal elements comprising this program are:

- a. Core Damage Sensitivity Studies.
- b. Severe Accident Uncertainty Analysis (SAUNA).
- c. Melt Progression Model (MELPROG) Development.

The core-damage sensitivity studies are directed toward identifying the most influential phenomena that govern the in-vessel core degradation process. A report, tentatively titled "Considerations in the Behavior of LWR Fuel and Coolant Systems During Severe Accidents" will contain material on accident sequence progression, fuel and core damage, RCS flow and heat transfer, fission-product considerations, and the development of test matrices for the DFR fuel damage experiments. This report will incorporate previous studies in those areas.

Work on the draft SAUNA report, Identification of Severe Accident Uncertainties, continued. A draft was reviewed by the working group meeting, and peer review was initiated.

The Melt Progression Model (MELPROG) calculates the in-vessel part of LWR accident sequences from rubble/debris formation through vessel failure. MELPROG includes models to calculate rubble melting by decay heat and oxidation, structural failure including vessel failure, melt/water interactions, and fission-product transport, plateout, and chemistry.

## EXECUTIVE SUMMARY

Coding of the basic structures module for MELPROG was completed on schedule. The package consists of one-dimensional heat transfer routines and creep rupture/melting structural failure models for cylindrical walls, perforated plates supported by columns, and perforated plates supported at the edges. Associated driver, input, and data management routines were also coded. Debugging of the structures module began. An input test deck was set up to facilitate run-time debugging.

### 6.2 LIGHT WATER REACTOR (LWR) FUEL DAMAGE EXPERIMENT PROGRAM

This program is directed toward examining the key phenomena that determine the core-damage configuration during the progression of a core melt sequence in an LWR core-uncovering accident. This program uses the information and perspectives gained in current LWR safety programs and focuses on the design of experiments that can contribute to the resolution of important severe-damage issues.

The two major areas of interest regarding in-vessel phenomena are:

- a. The behavior of fuel and cladding during the stages of major core deformation from rod-bundle geometry to a severely degraded geometry and
- b. The response of the severely damaged fuel to reintroduction of coolant from the emergency core cooling system (ECCS), especially the questions of redistribution of quenched material, short-term cooldown, increased steam generation, and oxidation reaction kinetics.

The safety analysis for the DF experiment plan has been completed. Included are several two-dimensional heat transfer calculations to determine the posttest heat load on the jacket and containment tube. Project personnel have begun reviewing the experiment plan with the ACRR safety committee.

The thermal hydraulic computer code used to predict the behavior of the DFR test section has been improved to account for axial radiant heat losses. This code has also been expanded to predict the behavior of the entire steam system, including the boiler, superheaters, CuO tubes, and condenser.

Fabrication of many of the in-pile components has been completed, and proof testing of these components has begun. The first full-scale out-of-pile steam system test has been successfully completed. No fuel rod simulators were included for this test. All systems performed satisfactorily and

## EXECUTIVE SUMMARY

confirmed the basic approach. These tests have shown, however, that some design modifications and procedures are desirable to eliminate potential noncondensibles from the system. Fabrication and proof testing of all components for the electrically heated rod simulator tests have been completed. Assembly is near completion. Tests with this system will be almost identical to those used in the in-pile system.

Tests have confirmed the feasibility of Raman spectroscopy for measuring  $H_2$  in the in-pile configuration of the DFR experiments. Most of the optical design has been completed and all of the major components needed for the visual diagnostics are either on order or have arrived.

A simple thermal-limit monitor has been designed that will provide an indication that maximum temperatures have been reached in the test section. For this approach, electrical continuity of platinum wires in the test section insulation will be monitored. When maximum allowable temperatures are attained in the test section, the wires will melt and the loss of continuity will be alarmed. This method is preferred since thermocouples (TCs) may not survive the high-temperature corrosive environment of the test section.

### 6.3 LIGHT WATER REACTOR (LWR) DEGRADED-CORE COOLABILITY PROGRAM

The LWR Degraded-Core Coolability (DCC) program investigates the coolability of uranium debris in water. The uranium is fission-heated in the ACRR to simulate the decay heat expected in an LWR severe core-damage accident. The governing phenomenological uncertainties to be investigated are pressure effects, deep bed behavior, particle size distributions, stratified beds, bottom coolant feed, and material effects. Each DCC experiment will determine coolability in three thermal regimes: (1) convection/boiling, (2) dryout, and (3) extended dryout. The staff will use experimental results to confirm and/or modify the present analytical models used to predict degraded-core coolability. Work is proceeding on two in-pile experiments, DCC-1 and DCC-2.

During the reporting period, the DCC program effort focused on the following activities:

1. Preliminary assembly of some DCC-1 hardware was performed, including the crucible, electric heater, primary passthroughs, and TCs. The final experiment assembly was not started due to the delay in receiving the uranium fuel.

## EXECUTIVE SUMMARY

2. The DCC-1 experiment plan was completed and reviewed by the Sandia Reactor Safety Committee. Because DCC-1 contains the most thermal energy and mechanical potential of any experiment performed in the ACRR, the safety analysis in the plan is based on adiabatic energy balances during all credible accident scenarios. The review process concentrated on showing that the assumptions used in this analysis were conservative.
3. A destructive test of an identical (stress equivalent) vessel to the DCC primary containment was performed. The D-test vessel ruptured at 17,700 psi in a hydrostatic test. The test demonstrated that the 3000-psi pressure rating of the primary containment has a safety factor of at least 4 to rupture.
4. Generalized momentum flow equations for separated two-phase flow through porous media were derived for use in the MELPROG from the steady-state momentum equations presently used in the Lipinski dryout model. These equations should provide a basis for a numerical treatment of debris beds, in case debris characterization is not handled in a separate module.
5. Two experiment safety analysis/design calculations were performed. An analysis of the TC placement in the DCC experiments revealed that for DCC-1, the 40 TCs could distort the measurement of the dryout heat flux by as much as 8%. A simple addition to the TC placement design will eliminate this source of error in the dryout heat flux measurement. Analysis of the danger to the DCC capsule caused by radiolysis of water and concomitant H<sub>2</sub> buildup demonstrated that this danger was, at best, minimal, and at worst, detectable at an early stage.
6. The writing of a major topical report was completed. This report delineates and documents remaining uncertainties in LWR degraded-core coolability predictions for accident analysis. It serves as a basis for a paper presented at the Cambridge LWR-SFD meeting (August 1983) but will also be published as a Sandia Report in an expanded and more complete form.
7. An analysis concluded that hot debris from a dry portion of the DCC experiment cannot become intimately mixed with cool water on a time scale of less than hundredths of a second. In that time scale, pressure equilibrium throughout the entire capsule will be maintained, and no large-scale motion of the debris

## EXECUTIVE SUMMARY

or the overlying liquid pool can be induced. Evidence for this conclusion is derived from past experiences with debris beds and simple calculations using basic debris bed properties.

### 7. TEST AND FACILITY TECHNOLOGY

#### 7.1 ACRR STATUS

This section contains comments on the general status of overall ACRR operation and remarks concerning experimental activities involving the ACRR.

The ACRR is operating normally in support of weapons program research and advanced reactor safety experiments.

REACTOR SAFETY RESEARCH  
QUARTERLY REPORT  
April-June 1983

1. CORE DEBRIS BEHAVIOR

1.1 EX-VESSEL CORE DEBRIS INTERACTION

(D. A. Powers, 6422; W. W. Tarbell, 6422;  
J. E. Brockmann, 6422)

If core debris formed during a severe reactor accident is not coolable, the debris will penetrate the reactor vessel and interact with structural material in the reactor cavity. This interaction could lead to gas generation, production of flammable species, and intense emission of radioactive aerosols, in addition to erosion of the reactor basemat.

Study of the phenomena associated with ex-vessel interaction of core debris with structural material found in the reactor cavity is the purpose of the Ex-Vessel Core Debris Interactions program. In the recent past, the major part of this program was the study of core debris interaction with concrete. Penetration of core debris through steel liners has also been examined. Other associated phenomena are currently undergoing study.

1.1.1 High-Pressure Melt Ejection Studies

Several recent safety studies have identified the possibility of reactor pressure vessel failure while the primary system is at elevated pressure. As a result, the ejection of molten core material into the reactor cavity is considered possible. The Zion Probabilistic Safety Study (ZPSS) analyzed the interactions of a molten jet stream ejected at high pressure from the reactor vessel. The analyses considered the consequences when the reactor cavity is completely filled with water ("water-locked"). The ZPSS hypothesizes that the material exiting the vessel would contact the water pool, rapidly quench the insuing vapor generation, and create a "steam bubble" that is that the remainder of the ejected material enters an essentially dry cavity.

Two experiments in the System Pressure Injection (SPIT) test matrix have been performed to study the interaction of a high-velocity melt jet and a simulated "water-locked" reactor cavity. The objective of the first test (SPIT-15) was to verify the existence of the steam bubble phenomenon described in the ZPSS. The second test (SPIT-17) used a scale model of the Zion cavity to determine the extent of water voiding. Subsequent paragraphs describe the results of these two tests.

### 1.1.1 SPIT-15

#### a. Apparatus

Determining the existence of a generated steam bubble required construction of a clear plastic box to house the water pool. A cubical volume, roughly 61 cm on each side, was fabricated and placed directly under the melt generator. Tap water (294.4 K [21.4°C]) filled the box to a depth of 50 cm, directly in contact with the melt plug in the lower generator flange. Two pressure transducers, one in the bottom and a second in the sidewall, were used to monitor pressures in the water pool. High-speed framing cameras focused on the pool were used for studying the interaction.

Ten kilograms of an iron oxide/aluminum thermite powder (yielding a molten iron/alumina mixture) were placed in the melt generator. The generator was charged with nitrogen to an initial pressure of 7.1 MPa that subsequently increased to over 12.9 MPa during the thermite reaction. Ignition of the thermite was induced at the top of the powder bed and required approximately 13 s to reach the bottom and fail the melt plug.

#### b. Observations

Motion picture records show that a steam explosion of a classic nature did not occur (propagating "detonation" waves were not seen). Measurements indicate that the jet propagated vertically downward through the water pool at nominally 20 m/s. This value represents a velocity reduction of nominally 65% from that predicted for a jet through air. The melt in the water pool was surrounded by a "film layer" that moved out and away from the melt. The film layer may have been caused by the rapid expansion of steam, but the velocity of propagation was orders-of-magnitude less than the bulk sound speed of water. Interaction of the film layer and the box sidewalls caused the walls to bulge and fail prior to arrival of the expanding melt.

After contacting the bottom of the water box, the melt rapidly expanded in all directions, eventually "filling" the entire volume. The melt did not have a tendency to move upward toward the free surface. The prompt failure of the box prevented any real confinement of the melt after initiation of the distribution process.

Subsequent events consisted of the dispersal of the melt and water away from the original configuration. The melt appeared to be luminous throughout the event, suggesting only limited water quenching. Gas burning was apparent near the lower edge of the box and was possibly due to the decomposition of water.



The recorded pressure data were inconsistent, with both gauges showing arrival of a pressure pulse corresponding to the film layer. The remainder of the pressure records was not reasonable, possibly because of the early failure of the box.

Following the test, the debris and plexiglass box pieces were found widely distributed about the apparatus. The box bottom remained in-place and undisturbed. Only slight scorching of the bottom piece was noted, indicating that the melt was promptly removed. The pressure transducer placed in the bottom plate, however, was badly damaged. Approximately 1/8 in. of the stainless steel case was ablated, exposing the sensing diaphragm. Thermal radiation through the water may have been significant, but the clear plexiglass was not affected because it is virtually transparent to the incident energy. Radiation-induced temperature effects may also explain the inconsistency of the pressure transducer responses.

The results of this test indicate that a "steam bubble" of the type hypothesized in the ZPSS did not occur. A "gas film" did accompany the melt in the water pool and had sufficient strength to fail the plexiglass water box, however, the velocity of propagation was much lower than that associated with the sound speed of water. A steam explosion did not occur, principally because the high velocity of the melt in the water prevented extensive melt/water mixing. The melt was eventually well distributed throughout the water tank, but most of the water pool was probably displaced ahead of the molten material.

#### 1.1.1.2 SPIT-17

##### a. Apparatus

For this experiment, a 1/20-scale aluminum cavity based on the Zion plant dimensions was fabricated and placed beneath the melt generator. The aperture of the melt generator was located at the scaled reactor pressure vessel (RPV) height. The model was filled with tap water to simulate a "water-locked" cavity. Aluminum was used to give a "rigid" cavity with approximately the same mechanical shock impedance as concrete to simulate the loading on the structure caused by expansion waves in the water pool. Six transducers were placed in the sidewalls and upper surfaces of the cavity to determine the pressure generated in the water pool during the interaction.

The melt generator was initially charged with 10 kg of iron/alumina thermite and pressurized with nitrogen to nominally 1500 psig. Pressure increased to 1600 psig during the thermite reaction. The reaction required just over 31 s to complete and fail the melt plug.

## b. Observations

Melt ejection was detected with a timing TC placed directly under the melt plug. Immediately (<1 ms) following ejection, a water slug began to propagate out of the open end of the slanted keyway. Some water was also lost from the seal between the generator and model. At 13 ms after ejection, melt penetrated the bottom surface of the cavity model and was followed immediately by a tremendous expansion that completely destroyed the structure. The violence of the interaction caused liquid water, steam, debris, and remains of the model to be scattered over a large area.

Five of the six pressure transducers produced records of the form shown in Figure 1.1-1. In this plot, the time is referenced to ejection as zero. The large pressure "spike" occurring at 13.8 ms corresponds to the large expansion seen in the framing camera records. The high-magnitude, rapid risetime, and short duration are all indicative of a strong shock wave propagating through the water pool. The data following the initial pulse are probably not real because structural integrity was lost during the initial transient.

Correlating the velocity of the melt in the water observed in the SPIT-15 test with the dimensions of the aluminum cavity indicates that the interaction occurred when the jet contacted the bottom cavity surface. The pressure pulse arrival times at the various gauge locations are not consistent with the assumption of a point source for the shock wave, suggesting that the melt may have been distributed more through the water pool when "triggering" occurred.

The results from the SPIT-17 test show a strong interaction between the melt jet and water pool, implying that the confinement provided by the structure may significantly influence the potential and magnitude of propagating interactions. The magnitude and intensity of the ensuing pressure pulse pose a serious threat to structures in contact with the water pool. Extrapolating these results to reactor-scale geometries should not be done until additional experiments have been conducted.

### 1.1.2 Transient Urania Concrete (TURC) Tests

The TURC tests have been initiated to investigate large-scale oxide melt interactions with concrete. They will provide a new data base that will be used in conjunction with previous steel/concrete interactions to form comparisons with current models. The experiments will assess various source terms, such as energy partitioning, gas generation rates, combustible gas production, aerosols, and fission-product transport, that may pose a threat to containment.

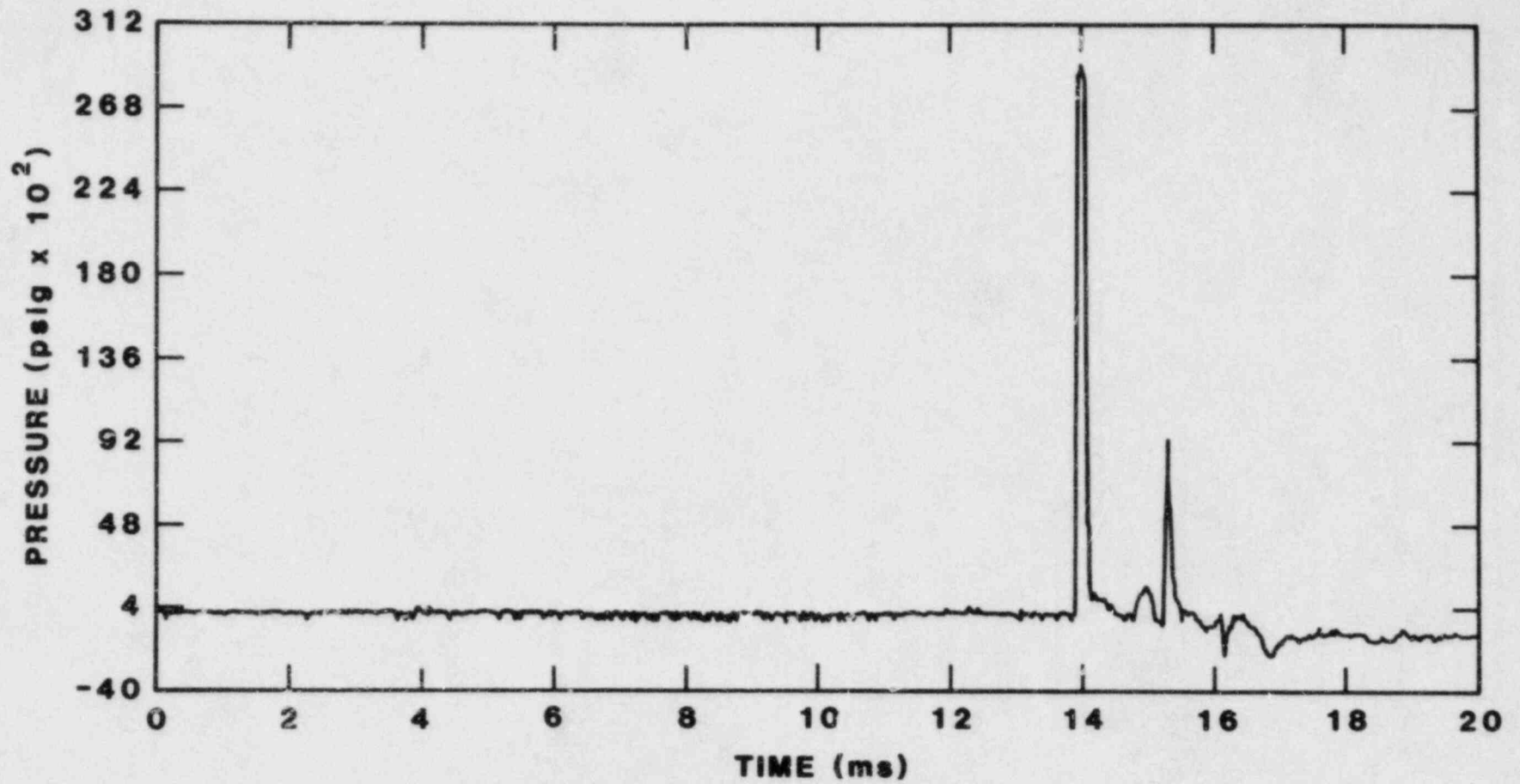


Figure 1.1-1. Pressure Record from Cavity Transducer  
(SPIT-17 Test)

During this quarter, a test matrix was defined:

Test TURC-1: a large-scale test with a thermitic melt

Test TURC 2: a large-scale test with molten  $\text{UO}_2$ -25 w/o  $\text{ZrO}_2$

Test TURC-3: a large-scale test with a molten mixture of  $\text{UO}_2$ - $\text{ZrO}_2$ -Zr

The first test, TURC-1, provides baseline data with a steel  $\text{Al}_2\text{O}_3$  melt that can be used to compare results of subsequent tests and the currently existing data base on melt/concrete interactions that involve steel melts. The test is also a cost-effective way of proof-testing the experimental procedures and diagnostic instrumentation.

The next two tests, TURC-2 and TURC-3, explore core debris/concrete interactions. The need to examine core debris composed of  $\text{UO}_2$  and  $\text{ZrO}_2$  as well as core debris composed of  $\text{UO}_2$ ,  $\text{ZrO}_2$ , and Zr arises because of uncertainty about the metal-water reactions that take place in severe reactor accidents. Analyses of reactor accidents with the MARCH code and similar models have recently indicated that the Zr-water reaction will not be complete at the time melt is expelled into the reactor cavity and concrete interactions begin. Obviously, heat produced by the reaction of Zr in the melt with the gaseous products of concrete decomposition will add to the complexity of core-debris/concrete interactions. VANESA-model analyses of aerosol production during core-debris/concrete interactions have suggested that both aerosol production and fission-product release increase when zirconium is present in the melt as a metal rather than as an oxide. The extent to which  $\text{H}_2\text{O}$  and  $\text{CO}_2$  released from the concrete are converted to  $\text{H}_2$  and  $\text{CO}$  will increase when zirconium metal is present.

Melts for the tests TURC-2 and TURC-3 will be prepared either by melting the material in a refractory crucible or by the embedded susceptor ring method (IRIS). The choice between these techniques will depend on the outcome of the full-scale IRIS-technique test.

Regardless of the melt formation technique, the TURC-series tests will use limestone/common sand concrete configured so that the concrete presents essentially a one-dimensional structure to the melt. The retention of the melt on this structure is accomplished by a castable magnesia ram surrounding the concrete. The design of this type of interaction crucible and testing of the magnesia ram were completed.

## 1.2 CORE RETENTION MATERIALS ASSESSMENT

(E. R. Copus, 6422; T. Y. Chu, 7537; D. A. Powers, 6422)

The Core Retention Materials Assessment program is an effort to identify the difficulties and utility of incorporating core retention devices in reactor cavity regions to mitigate the consequences of ex-vessel core-debris interactions. A major goal of this program is the establishment of the Large-Scale Melt Facility (LMF) that will allow tests of candidate designs exposed to melts of up to 500 kg of fuel oxides. Initial work in this program focuses on final development of the LMF and the engineering of magnesia bricks for core retention devices and the conceptual development of the thorium rubble-bed core retention device.

### 1.2.1 Characterization of Magnesia-Brick Core Retention Devices

Previous work in the Containment Load Mitigation program has shown that magnesia bricks can contain, quite successfully, molten steel and melts produced by the classic thermite reaction. The attention of the program during FY83 was devoted to a large-scale interaction test with molten  $UO_2$  on magnesia bricks.

Most analyses of the potential capabilities of magnesia in the floating nuclear power plant have been based on considering the magnesia to be a monolithic structure. In fact, the structure will be composed of bricks. The analyses of magnesia as a monolithic structure can always be questioned because there are device failure mechanisms peculiar to bricks. For instance, magnesia bricks might float in the  $UO_2$  pool and cause a loss of integrity of one or more layers of the core retention device without the energy expenditure required to ablate material. Molten  $UO_2$  has a low viscosity and wets  $MgO$ , whereas steel does not wet  $MgO$ . The molten  $UO_2$  could penetrate the gaps between bricks and attack the device support structure without being delayed by ablation of the magnesia. All ceramic structures are susceptible to catastrophic failure by thermal shock. Laboratory evidence suggests a gas-producing reaction between  $MgO$  and  $UO_2$ .

To test the performance of the magnesia bricks in the presence of  $UO_2$ , a large-scale test using the LMF heating technology was conducted. A quick-look report containing all test details has been issued.[1-1]

The melt was 234 g of a  $UO_2$ -25 w/o yttria-stabilized  $ZrO_2$ . This mixture approximates closely the oxide phase of a core melt if the zircaloy clad on the  $UO_2$  fuel has been oxidized to  $ZrO_2$ . The liquidus temperature of this mixture is  $2798 \pm 25$  K ( $2525 \pm 25^\circ C$ ). The melt was heated to  $2873 \pm 50$  K ( $2600 \pm 50^\circ C$ ) and drained over a 4-min period into a cylindrical crucible made of high-purity magnesia bricks.

Instrumentation available for the interaction test included:

- a. aerosol detectors,
- b. gas samplers,
- c. temperatures within the magnesia,
- d. crack detectors on the magnesia bricks, and
- e. upward heat flux monitors above the retention device.

Results of the large-scale  $\text{UO}_2$ /magnesia brick test are of recent vintage and have not been fully evaluated. Immediate results indicate clearly that:

- a. Aerosol emissions during teeming of the melt and the melt/magnesia interaction were quite small in comparison to what would be expected if concrete were exposed to melt.
- b. Noncondensable-gas generation was not observed during the  $\text{UO}_2$ /magnesia interaction.
- c. Melt did not enter the gaps between bricks.
- d. The loose brick in the structure did not float.
- e. Fracturing of the bricks caused by sudden exposure to hot melt was confined to a surface spall (<1/4 in. deep) and body cracks at the high thermal-stress points where bricks forming the crucible walls meet bricks forming the crucible bottom.

The test observations support the contention that magnesia bricks would be a material superior to concrete. The test illustrated graphically the capability of magnesia to eliminate aerosol and gas generation during ex-vessel core debris interactions. Catastrophic thermal-shock failure of the device did not occur.

Further analysis of the test results will be necessary to determine the extent to which tools for calculating the performance of magnesia-brick core retention devices can be believed. Clearly, the test did not answer all the major questions concerning magnesia-brick core retention devices. No major gas production was observed in the test, but the frozen  $\text{UO}_2$  pool was not a solid body. It was, in fact, quite porous. Some limited evolution of gas, or more likely vapor, may have been responsible for this porosity. Such gas or vapor generation is obviously insignificant in the context of containment loading. However, it may indicate a chemical

attack on MgO that is not yet understood. Also, the interaction was transient in the sense that once it was deposited, the melt cooled naturally. A test in which the UO<sub>2</sub> pool is sustained at melt temperatures is necessary to characterize major features of UO<sub>2</sub> interactions with magnesia bricks completely.

### 1.3 SODIUM CONTAINMENT AND STRUCTURAL INTEGRITY

(E. Randich, 6422; R. U. Acton, 7537; D. A. Powers, 6422)

The Sodium Containment and Structural Integrity program is an investigation of safety phenomena that will develop should molten sodium contact structural or shielding concrete during a reactor accident. Quantitative evaluation of these phenomena, leading to the development of models for use in predicting the ways in which these phenomena might threaten the reactor containment, is a major goal of this program. Quantitative evaluation of structural flaws in reactor cell liners is also sought in this program because these flaws can provide pathways for sodium to contact concrete.

#### 1.3.1 Sodium/Concrete Interactions

Work proceeded on the documentation necessary to conclude the sodium-concrete interaction portion of the project. Three topical reports were issued this quarter and a fourth, on the subject of the Sodium Limestone Concrete Ablation Model (SLAM) code, will be issued next quarter. Brief summaries of the issued reports are presented below.

##### 1.3.1.1 The NaOH-Rich Corner of the $(\text{Na}^+, \text{Ca}^{2+}) (\text{OH}^-, \text{CO}_3^{2-})$ Reciprocal System[1-2]

The sodium-rich portion of the binary system  $(\text{NaOH})_2 - \text{Ca}(\text{OH})_2$  and the reciprocal system  $(\text{Na}^+, \text{Ca}^{2+}) (\text{OH}^-, \text{CO}_3^{2-})$  are described. The  $(\text{NaOH})_2 - \text{Ca}(\text{OH})_2$  system has a peritectic decomposition at  $603 \pm 5 \text{ K}$  ( $330 \pm 5^\circ\text{C}$ ) and a mole fraction  $\text{Ca}(\text{OH})_2$  of  $0.0055 \pm 0.0020$ . A compound with the apparent stoichiometry  $\text{Na}_6\text{Ca}(\text{OH})_8$  is formed in the system. The compound melts at  $833 \pm 10 \text{ K}$  ( $560 \pm 10^\circ\text{C}$ ). X-ray diffraction data for this compound are presented. Solid-state solubility of the compound in  $\beta$ -NaOH causes a depression in the temperature of the  $\alpha \rightarrow \beta$  phase change.

Liquidus data for 27 compositions in the NaOH-rich portion of the reciprocal system are reported. These data may be interpreted in terms of a ternary peritectic or a semi-eutectic. Ternary invariant temperatures were not measured. An apparent invariant at  $558 \pm 5 \text{ K}$  ( $285 \pm 5^\circ\text{C}$ ) is attributed to a disequilibrium eutectic reaction between NaOH and  $\text{Na}_2\text{CO}_3$ .

The liquidus along the  $(\text{NaOH})_2 - \text{CaCO}_3$  join shows that the apparent solubility of  $\text{CaCO}_3$  in NaOH increases sharply when temperatures exceed  $773 \text{ K}$  ( $500^\circ\text{C}$ ). The apparent solubility of  $\text{CaCO}_3$  in  $(\text{NaOH})_2$  for the temperature range  $623$  to  $773 \text{ K}$  ( $350^\circ$  to  $500^\circ\text{C}$ ) can be described by the expression

$$\ln(x) = -7568/T + 7.36$$



where  $x$  is the mole fraction  $\text{CaCO}_3$  and  $T$  is the absolute temperature. This observation is used to interpret some of the features of sodium interactions with limestone concrete.

#### 1.3.1.2 Intermediate-Scale Tests of Sodium Interactions with Calcite and Dolomite Aggregate Concretes[1-3]

Two intermediate-scale tests were performed to compare the behavior of calcite and dolomite aggregate concretes when attacked by molten sodium. The tests were performed as part of an interlaboratory comparison between Sandia National Laboratories and Hanford Engineering Development Laboratories (HEDL). Results of the tests at Sandia National Laboratories are reported here. The results show that both concretes exhibit similar exothermic reactions with molten sodium. The large difference in reaction vigor suggested by thermodynamic considerations of  $\text{CO}_2$  release from calcite and dolomite was not realized. Penetration rates of 1.4 to 1.7 mm/min were observed for short periods of time with reaction zone temperatures in excess of 1073 K (800°C) during the energetic attack. The penetration was not uniform over the entire sodium-concrete contact area. Rapid attack may be localized due to inhomogeneities in the concrete. The chemical reaction zone is less than 1 cm thick for the calcite concrete but is about 7 cm thick for the dolomite concrete. This difference is apparently caused by the lower thermal decomposition temperature of dolomite. The major chemical reactions of importance are  $\text{Na} + \text{N}_2\text{O} + \text{limestone} \rightarrow \text{Na}_2\text{CO}_3 + \text{CaO} + \text{MgO} + \text{H}_2$  and  $\text{Na} + \text{H}_2\text{O} \rightarrow \text{NaOH} + 1/2 \text{H}_2$ .

#### 1.3.1.3 Laboratory-Scale Sodium-Carbonate Aggregate Concrete Interactions[1-4]

A series of laboratory-scale experiments was made at 873 K (600°C) to identify the important heat-producing chemical reactions between sodium and carbonate aggregate concretes. Reactions between sodium and carbonate aggregate were found to be responsible for the bulk of heat production in sodium-concrete tests. Exothermic reactions were initiated at  $853 \pm 30$  K ( $580 \pm 30^\circ\text{C}$ ) for limestone and dolomite aggregates as well as for hydrated limestone concrete, and at  $813 \pm 10$  K ( $540 \pm 10^\circ\text{C}$ ) for dehydrated limestone concrete but were ill-defined for dolomite concrete. Major reaction products included  $\text{CaO}$ ,  $\text{MgO}$ ,  $\text{Na}_2\text{CO}_3$ ,  $\text{Na}_2\text{O}$ ,  $\text{NaOH}$ , and elemental carbon. Sodium hydroxide, which forms when water is released from cement phases, causes slow erosion of the concrete with little heat production. The time-temperature profiles of these experiments have been modeled with a simplified version of the SLAM computer code that has allowed derivation of chemical reaction rate coefficients.

### 1.3.2 LMFBR Radiological Source Term Assessment

Work continued in defining the scope of the source term project and evaluating different methods for the trace element analysis needed in this project. In the first area, an extensive literature search was initiated and needed experimentation was outlined. A tentative representative list of fission-product and fuel simulants was chosen that includes U, Ce, I, Cs, Ba, Te, Zr, Nb, Ru, and La. A bounding two-level factorial design experiment was chosen with three independent variables: temperature, gas sparging, and NaOH content.

One of the major difficulties in accurately measuring fission-product release rates from a molten sodium pool is the detection limit of the chemical analysis of the released material. If realistic concentrations of fission-product simulants are used in the sodium pool, the released aerosols and vapor contain only minute amounts of the simulants (<1 to 1000 ppm). The analysis scheme used to accurately measure such concentrations, particularly when so many elements are present, must be chosen carefully. Sodium samples containing 20, 200, and 2000 ppm of the simulants have been prepared and are being analyzed by atomic absorption (AA), inductively coupled plasma (ICP), and spark source mass spectroscopy to compare trace element analysis techniques. The results will be used to define experimental collection techniques and sample size for the material released from the pool.

#### 1.4 DEBRIS BED COOLABILITY

(G. W. Mitchell, 6421; C. A. Ottinger, 6421)

The Debris Bed Coolability program addresses issues concerned with the deposition of solid fuel debris on horizontal surfaces within the containment vessel and its subsequent coolability. This debris remains capable of generating significant power through the decay of fission products. Should natural processes fail to provide sufficient cooling, the debris could melt and threaten containment. The Debris Bed Coolability program seeks to determine the conditions required for natural cooling of such debris.

##### 1.4.1 Joint Review Meeting

A 3-day program review meeting was held for program sponsors during the first week in April. Representatives from JRC (Euratom), PNC (Japan), and USNRC attended. The overall D10/D13 experiment design, instrumentation, design analyses, expected operating procedures, and the results of the crucible material compatibility program were reviewed.

The results of the crucible material compatibility low-temperature tests were reviewed. The tests were conducted at temperatures of 573, 823, and 1073 K (300°, 550°, and 800°C), sodium oxygen content of 2, 50, and 100 ppm, and exposure times of 10, 70, and 130 hr. The results were in the form of the material samples' toughness and strength before and after exposure to sodium. Weight change of the samples was reported to be less than  $\pm 0.1\%$ . The data indicated that Ta-10W, Mo-41Re and T-111 alloys were not significantly affected by sodium exposure under the conditions tested. These materials were further tested at Los Alamos National Laboratory to temperatures up to 2423 K (2150°C). In these tests, a 1-in.-diameter tube was filled with 85 g UO<sub>2</sub> and 12 g of sodium. The bottom of the sealed tube was then heated in a vacuum to high temperatures. Since the top of the tube remained at temperatures below 1273 K (1000°C), a temperature gradient was established along the tube. Following the tests, the tubes were sectioned and polished. Photomicrographs of the tube walls were examined at the review meeting. Although substantial grain growth was apparent in the tube walls, none of the three candidate materials indicated significant interactions or degradation. A considerable amount of discussion followed the presentation of the materials testing results. Concern was expressed, especially for Ta-10W, about the limited range over which the tests were conducted and potential interactions that might occur with sodium or UO<sub>2</sub> outside this range. Additional tests were proposed to investigate the concern.

A preliminary crucible design was also presented at the review meeting. Because of availability, Ta-10W was selected as the preferred crucible material. Discussion of crucible design concepts centered around welding and the interface of the bottom crucible structure, which will allow for bottom

cooling. Investigation will be done to determine the feasibility of diffusion bonding the bottom of the crucible and the susceptibility of Ta-10W to liquid metal embrittlement. Procurement will be initiated of Ta-10W material for the crucible with the final design depending on the results of these investigations. Orders were placed for these components at the end of April.

Draft copies of the review meeting minutes were sent to program sponsors in May. Action items generated during the meeting were forwarded to the sponsors in June.

#### 1.4.2 Thermal Analyses

Two-dimensional thermal analyses of the experiments were performed to determine expected temperatures around the crucible. These results will be used in the containment stress analysis and for the optimization of instrumentation locations. Also, they will be used to refine the crucible thermal and structural analysis. The calculations indicated a more uniform temperature distribution in the lower containment structure than had previously been assumed. This uniform temperature distribution will reduce thermal gradient-induced stresses. Further, TCs located in the heat flux block below the crucible should be adequate to measure downward heat removal from the bed to within  $\pm 10\%$  for most flow conditions. Heat removal at low helium flow rates will be difficult to measure accurately because of small temperature gradients.

#### 1.4.3 Instrumentation

A test of the ultrasonic thermometer (UT) was conducted in June utilizing thoriated tungsten sensor wire and low-density thoria insulator material. This combination of materials appeared to provide improved uniformity of signals at temperatures up to 2773 K (2500°C), due to reduced material transport. Undesirable coil and remender temperature effects were still apparent and remain to be resolved. Additional tests are planned to quantify these effects.

Because of the uncertainty of successful resolution of the UT temperature effects, the project staff decided to replace one of the three UTs planned for the experiment with a high-temperature TC assembly, increasing the number of C-type junctions in the bed from two to six. The revised instrumentation layout based on this decision is shown in Figure 1.4-1.

Development and fabrication of the C-type TC assemblies continued. Because of the extremely successful operation of these TCs in the DC-1 experiment accomplished in May, insulators were procured for use in the D10/D13 TCs. With this insulator, HEDL would attempt to qualify these TCs to 2673 K (2400°C).

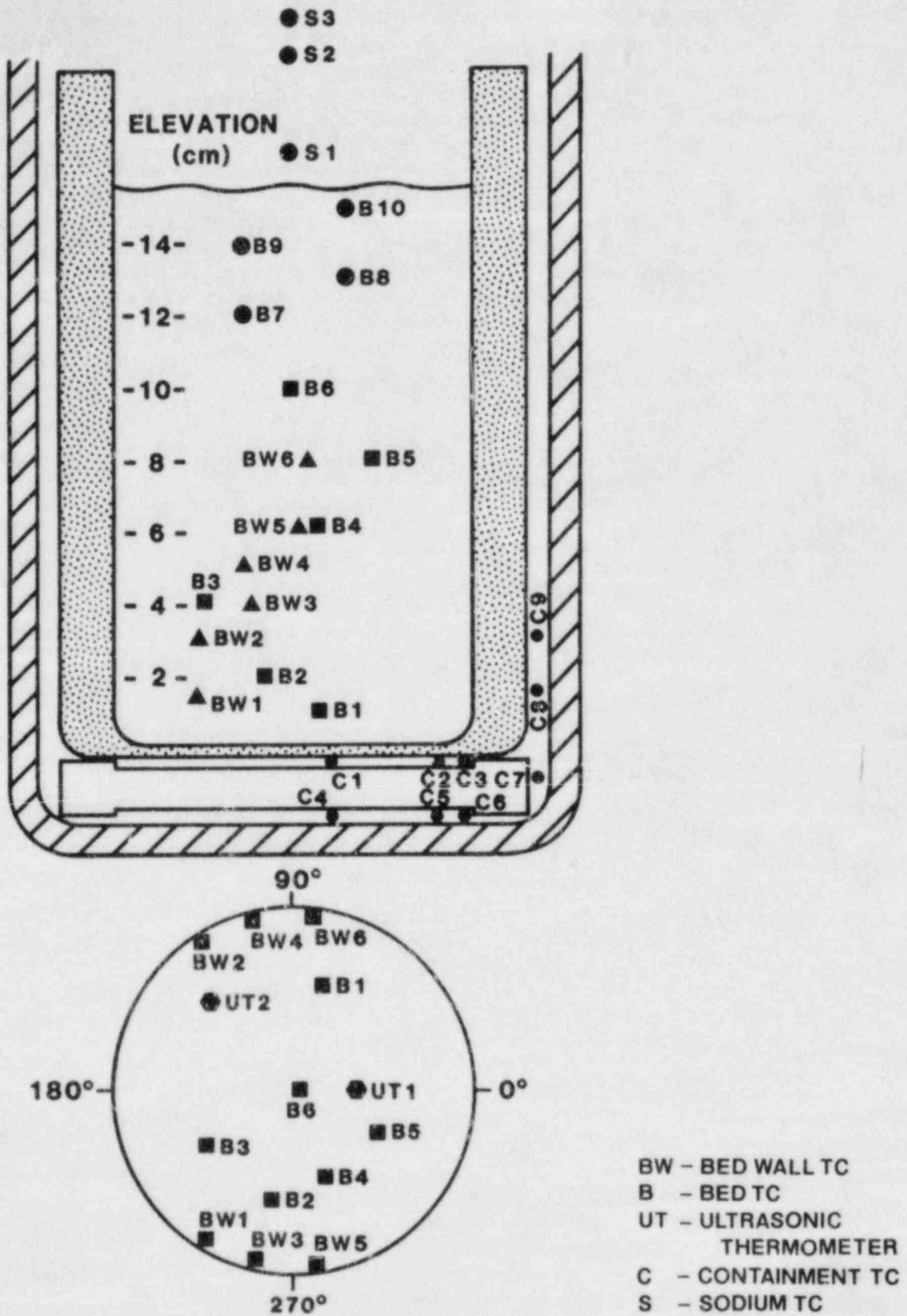


Figure 1.4-1. Instrument Layout of the D10/D13 Experiments

#### 1.4.4 Component Fabrication

Fabrication of all experiment components continued. The first helium flow divider was delivered in June under inspection agreements in the fabrication contract. Fabrication of all other components in this contract (outer helium container, neutron filter, and nitrogen flow divider) was initiated upon acceptance of the helium flow divider. Delivery of these components is expected in August. Fabrication of the containment components was initiated with a first article inspection in August and delivery of one set of components in September. Drawings for all access section components were prepared. A purchase order was also prepared for these components.

#### 1.4.5 Experiment Plan

The experiment safety evaluation was begun in preparation for the presentation to the ACRR safety committee. The safety evaluation includes a description of experiment components and an evaluation of their capabilities to function as containment components under normal and accident conditions.

## 1.5 DRY DEBRIS MELT PROGRESSION

(J. T. Hitchcock, 6421; J. E. Kelly, 6425)

The Dry Debris Melt Progression study, a follow-on to the Molten Pool program, uses prototypic reactor materials to investigate experimentally the progression of a debris bed from dryout to melt and the interaction of the melt with structural and core retention material.

The DC 1 experiment completed May 25, 1983, was the first fission-heated dry  $UO_2$  debris bed that achieved a sizeable urania molten pool (0.8 kg) at steady-state conditions. Steady conditions at several powers lower than required for melt were also achieved. The purpose of the experiment was to obtain information on high-temperature dry debris heat transfer rates, melt formation, melt migration, and melt heat transfer rates. The data will be used for analysis and model development on coolability and melt behavior of the dry portion of reactor debris for LMFBR accident codes. These data also have applications to LWR severe accident debris coolability.

### 1.5.1 Experiment Description

The bed was composed of a homogeneous mixture of 2138 g of fully enriched  $UO_2$  particulate 70 mm high and 80 mm in diameter. The particle size varied from 100 to 1000  $\mu m$  with a bed porosity of 0.39. The bed was contained in a tungsten crucible with an 8-mm-thick internal  $ThO_2$  liner. Argon at 5 psia was used as the cover gas to simulate the heat transfer characteristics of sodium vapor.

The debris was cooled at the top and bottom and insulated radially. Heat from the bottom of the bed was conducted downward through two containment vessels and was removed to a helium heat transport loop with a constant flow rate, allowing for steady-state operation. A liquid indium bond (melting point 423 K [150°C], boiling point 2273 K [2000°C]) was used to couple the crucible thermally to the inner containment and to couple the inner and outer containments. The top of the bed was cooled by radiation to a tee-shaped tantalum heat transfer plate. The heat was shunted through this plate to the containment sidewalls and to the He coolant. The bed was radially insulated, by the  $ThO_2$  sleeve inside the crucible and by low-density  $ZrO_2$  between the crucible and the sidewalls. The DC 1 assembly is illustrated in Figure 1.5-1. A dimensioned schematic of the bed and adjacent material is shown in Figure 1.5-2.

The instrumentation in the bed included four UTs and three TCs as illustrated in Figure 5.1-3. The UTs consisted of a W sensor, an inner  $ThO_2$  sheath, and an outer protective W sheath. Each sensor had five intervals of 10 mm that gave temperature measurements at five axial locations at 10 mm

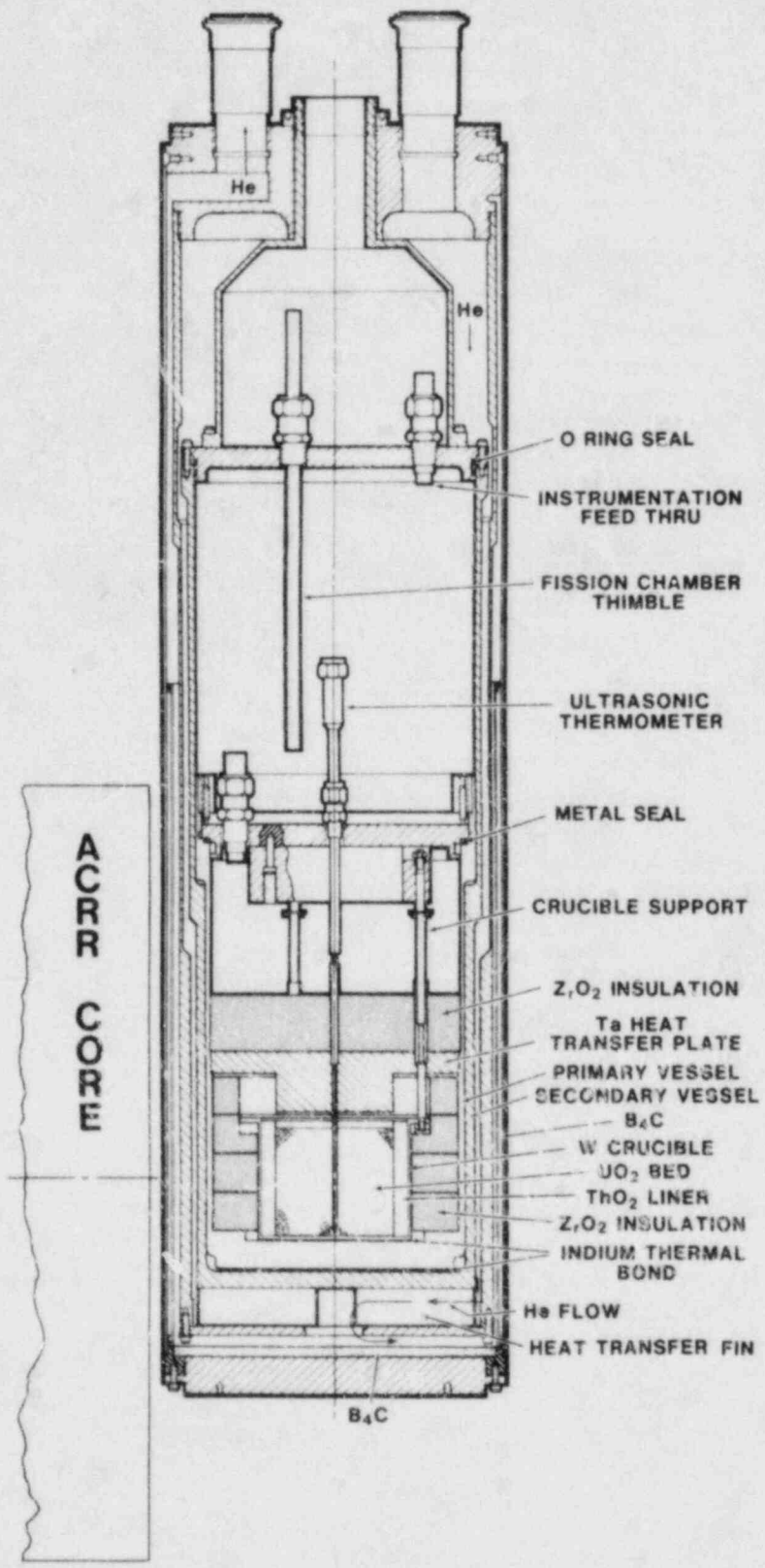


Figure 1.5-1. Dry Capsule Test Configuration



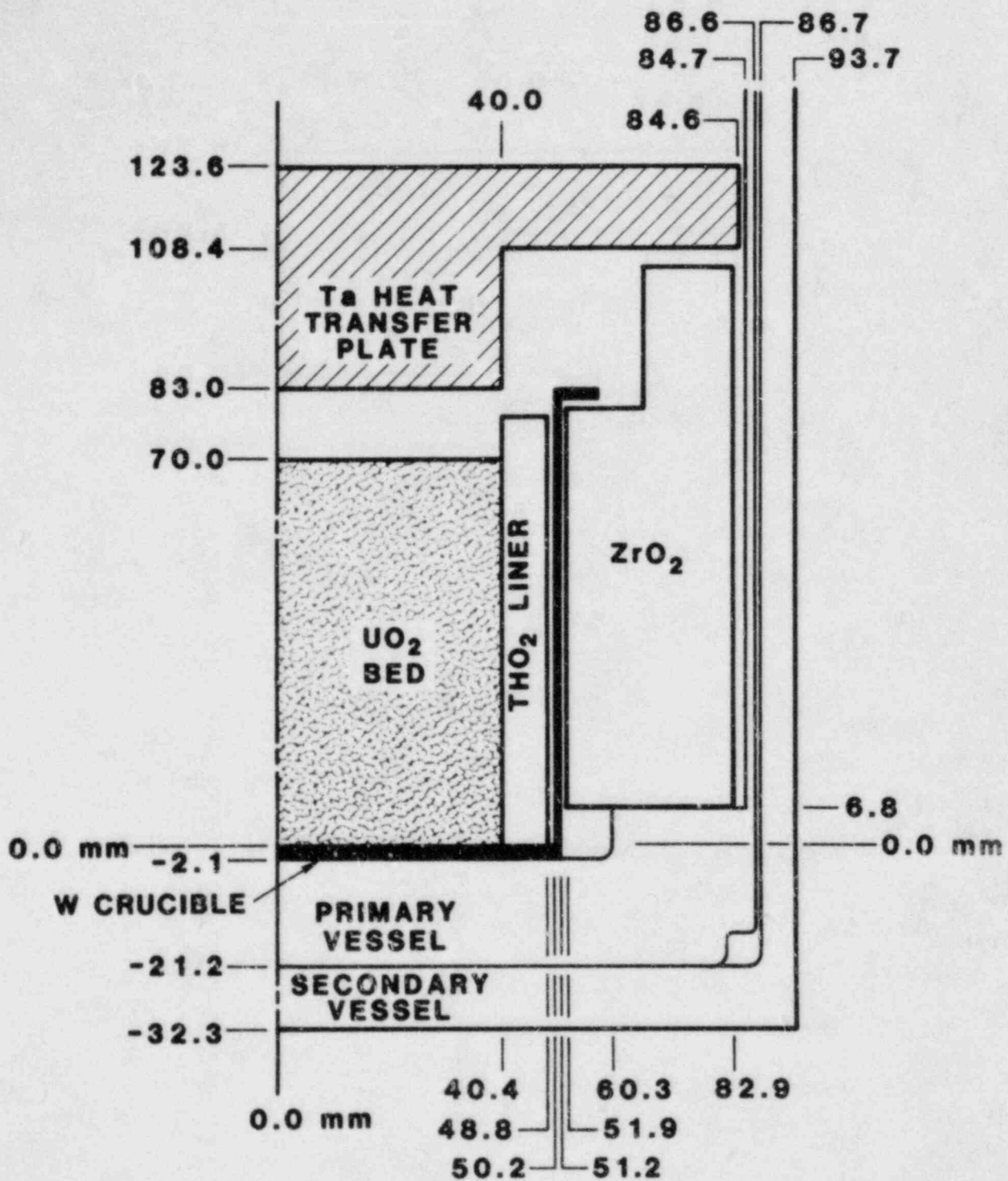
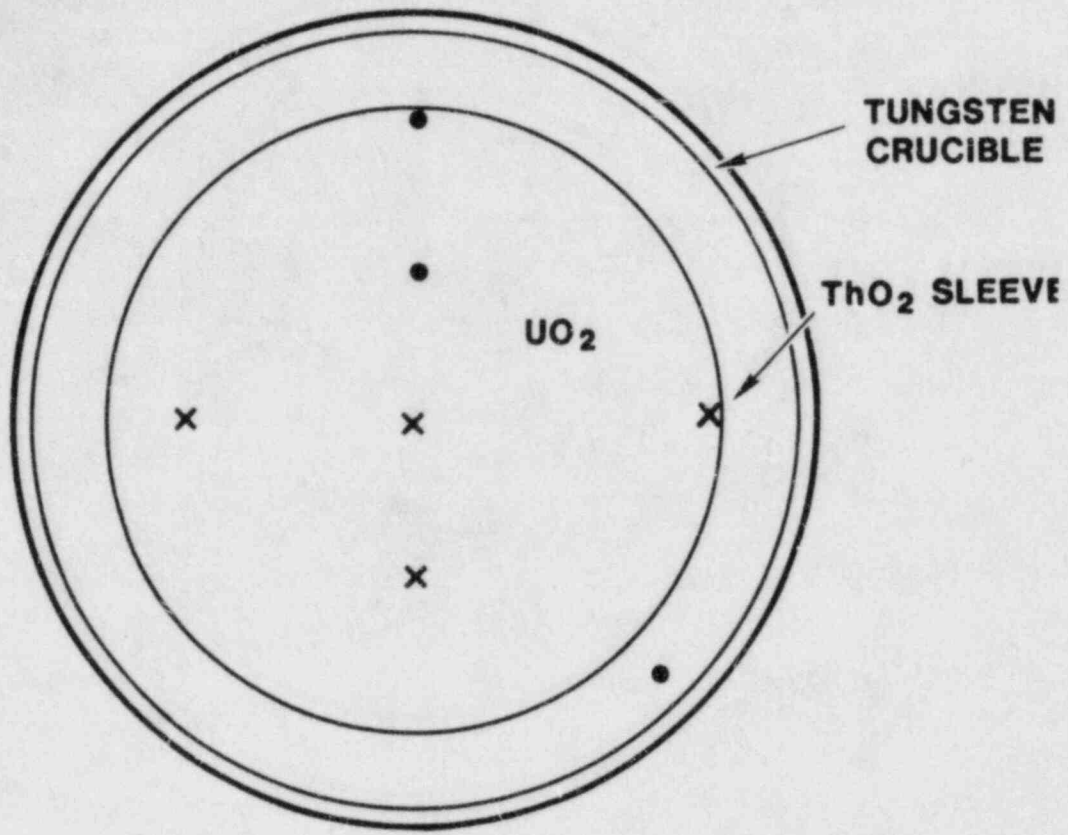


Figure 1.5-2. Schematic of DC 1



- x 4 UT's  
AT R = 0, 20, 30,  
40 mm
- 3 TC's  
AT R = 20, 40 mm  
1 IN ThO<sub>2</sub> SLEEVE

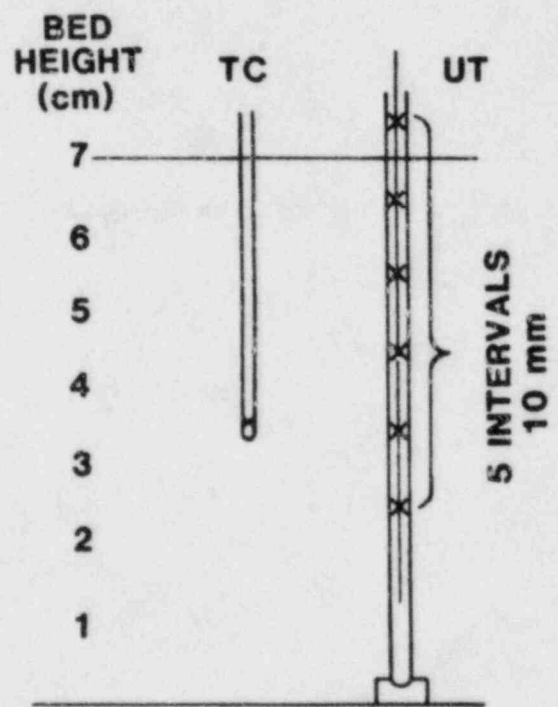


Figure 1.5-3. DC 1 Bed Instrumentation

centerline. The TCs had a W sheath,  $\text{HfO}_2$  insulation, and W 5% Re/W 26% Re thermal element wires that had been performance tested to 2473 K (2200°C). Above this temperature, the  $\text{HfO}_2$  insulation deteriorates and eventually melts, but the W sheaths contain all of the components. Two of these TCs were placed in the bed and used during the heatup portion of the experiment to confirm the response of the UTs. The junctions were placed at the midplane of the bed at radial locations of 20 and 40 mm. The third TC was located within the  $\text{ThO}_2$  liner.

Within the experiment capsule, R-type TCs were used in the Ta heat transfer plate to measure the heat flux out of the top of the bed and through the side  $\text{ZrO}_2$  insulation. K-type TCs were used to measure the downward heat flux in the containment vessels and the helium and containment boundary temperatures. A tabulation of the DC 1 instrumentation along with its location is shown in Tables 1-I and 1-II.

The objective of the first part of the DC 1 experiment was to determine the thermal characteristics of dry reactor debris. The bed was stepped to three power levels and held for equilibration. Steady-state maximum temperatures measured by the centerline UT and by TCs in and around the bed are given in Table 1-III.

The Ta and steel temperatures are centerline values at the surface of the Ta heat transfer plate above the bed and at 3.8 mm into the steel containment below the W crucible, respectively. These measured temperature distributions will be used to provide accurate information on the effective thermal conductivity of dry debris beds. This information will be presented as the experiment temperature data are analyzed.

In the second part of the experiment, the phenomenology and thermal characteristics of melt formation were studied. The bed power was increased to 2.5 W/g and maintained for 80 min. Approximately 40% of the bed (0.8 kg) melted, forming a molten pool about 20 mm high and 70 mm in diameter with a peak measured temperature of 3273 K (3000°C). The Ta surface and steel containment temperatures were 1639 and 993 K (1366° and 720°C), respectively. At the steady-state condition, upward and downward heat partitioning was determined. After equilibration, bed power was reduced to 0.45 W/g to compare postmelt conditions to premelt conditions. The experiment was then terminated.

### 1.5.2 Experimental Results

The DC 1 test has provided data needed for modeling the coolability of melt formation in dry reactor core debris. Initial results provide information on the thermal characteristics of dry debris and on the formation of and heat transfer in molten pools. Radiography, to be performed after

Table 1-I

## Description of Thermocouples

	Type	Location	
		Radius (mm)	Height (mm)
TC1	W 5 Re/W 26 Re	Bed	35
TC2	W 5 Re/W 26 Re	Bed	35
TC3	W 5 Re/W 26 Re	ThO <sub>2</sub>	35
TA11	R	Ta	87.3
TA12	R	Ta	87.3
TA13	R	Ta	87.3
TA21	R	Ta	107.6
TA22	R	Ta	107.6
TA23	R	Ta	107.6
TA3	R	Ta	116.3
TA4	R	Ta	116.3
TA5	K	Ta	116.3
TA6	K	Ta	116.3
SS11	K	Primary	-5.9
SS12	K	Primary	-5.9
SS13	K	Primary	-5.9
SS14	K	Primary	-5.9
SS21	K	Secondary	-26.8
SS22	K	Secondary	-26.8
SS23	K	Secondary	-26.8
SS24	K	Secondary	-26.8
PC1	K	Primary	6.8
PC3	K	Primary	6.8
PC4	K	Primary	6.8
PC5	K	Primary	105
PC6	K	Primary	105
HE1	K	He outlet	510
HE3	K	He inlet	510
ZR1	R	ZrO <sub>2</sub>	35
ZR2	R	ZrO <sub>2</sub>	35
ZR3	K	ZrO <sub>2</sub>	35
ZR4	K	Primary	35
OC1	K	On Validyne pressure transducer outside primary	
OC2	K	On primary vessel lid r=15	
OC3	K	On primary vessel lid r=78	
OC4	K	On UT1 housing	

the package has cooled several months, will provide preliminary data on the phenomenology of melting debris: sintering and void and crust formation. Final detailed information on the phenomenology will be obtained upon disassembly and microscopic examination of the bed.

Table 1-II

Description of Ultrasonic Thermometers

	<u>Radial Position (mm)</u>
UT 1	0.0
UT 2	20.0
UT 3	30.0
UT 4	38.9

<u>Element</u>	<u>Axial Location of Measurement Interval (mm)</u>
1	65 - 75
2	55 - 65
3	45 - 55
4	35 - 45
5	25 - 35

Table 1-III

Steady-State Maximum Temperatures

Bed Power (W/g)	Central UT (°C)	Bed Thermocouples		Ta Plate (°C)	Steel Containment (°C)
		(r = 20 mm) (°C)	(r = 20 mm) (°C)		
0.18	975	925	529	133	114
0.45	1699	1656	960	290	206
0.72	2230	2141	1277	426	282

In addition to meeting the test objectives, the experiment hardware, including the liquid indium heat transfer bonds, performed as designed. The in-bed W/Re TCs performed to and possibly far beyond their rated temperature limit of 2473 K (2200°C). For although the measured integral parameter

of loop-to-sheath resistance indicated electrical shunting above 2473 K (2200°C), the EMP continued to increase to a value corresponding to 2773 K (2500°C). Three of the four UTs survived to the final step and, as expected, failed successively as the temperature increased. The central UT survived at temperature in excess of uranium melt for 1800 s.

The bed temperature and reactor power traces for the test are illustrated in Figures 1.5-4 through 1.5-7. The reactor power history (proportional to the bed power) is shown in Figure 1.5-4. A graph of the bed TC data is shown in Figure 1.5-5. These W/Re thermocouples show the thermal response of the bed and steady-state conditions used to investigate the dry debris and the progression into melt. Figure 1.5-6 gives the temperature profiles for elements 4 and 5 of each UT. These are the bed midplane measurements and correspond with the TC data. Data from the five elements of the central UT are shown in Figure 1.5-7.

The steady-state TC measurements are tabulated in Table 1-IV. These values represent 1-min time averages of the actual temperatures. The times selected for this tabulation correspond to the times at which the bed and capsule had reached steady-state conditions. A similar tabulation of the steady-state UT temperature measurements is given in Table 1-V.

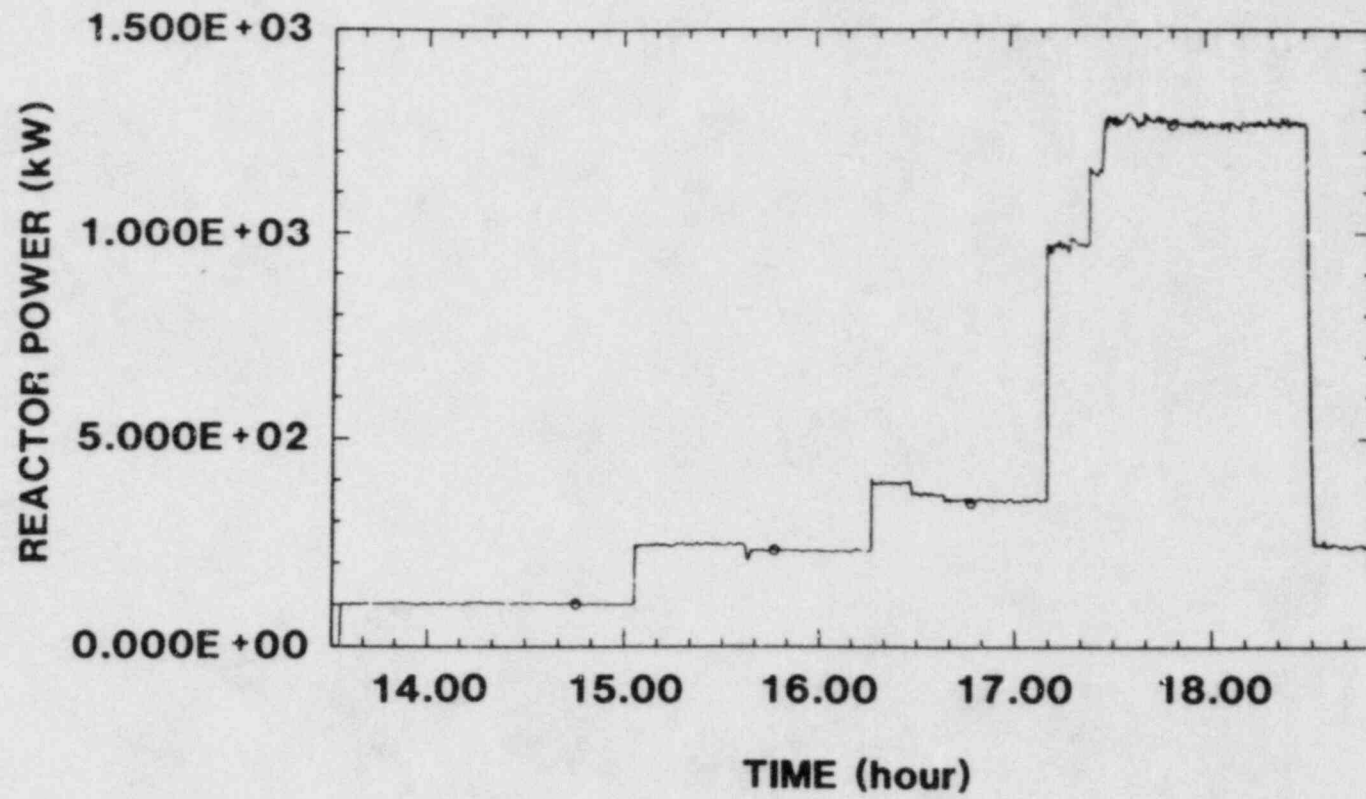


Figure 1.5-4. DC 1 Reactor Power

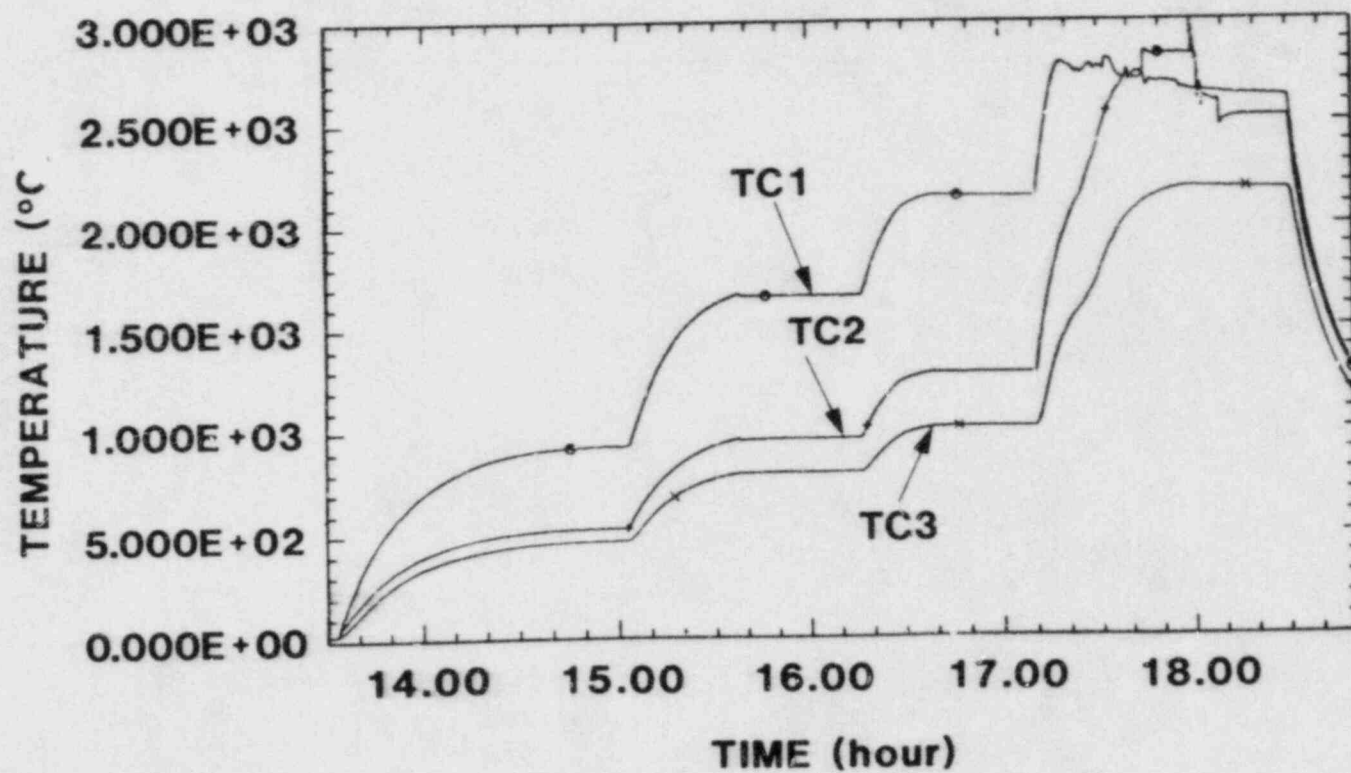


Figure 1.5-5. DC 1 Thermocouple Data



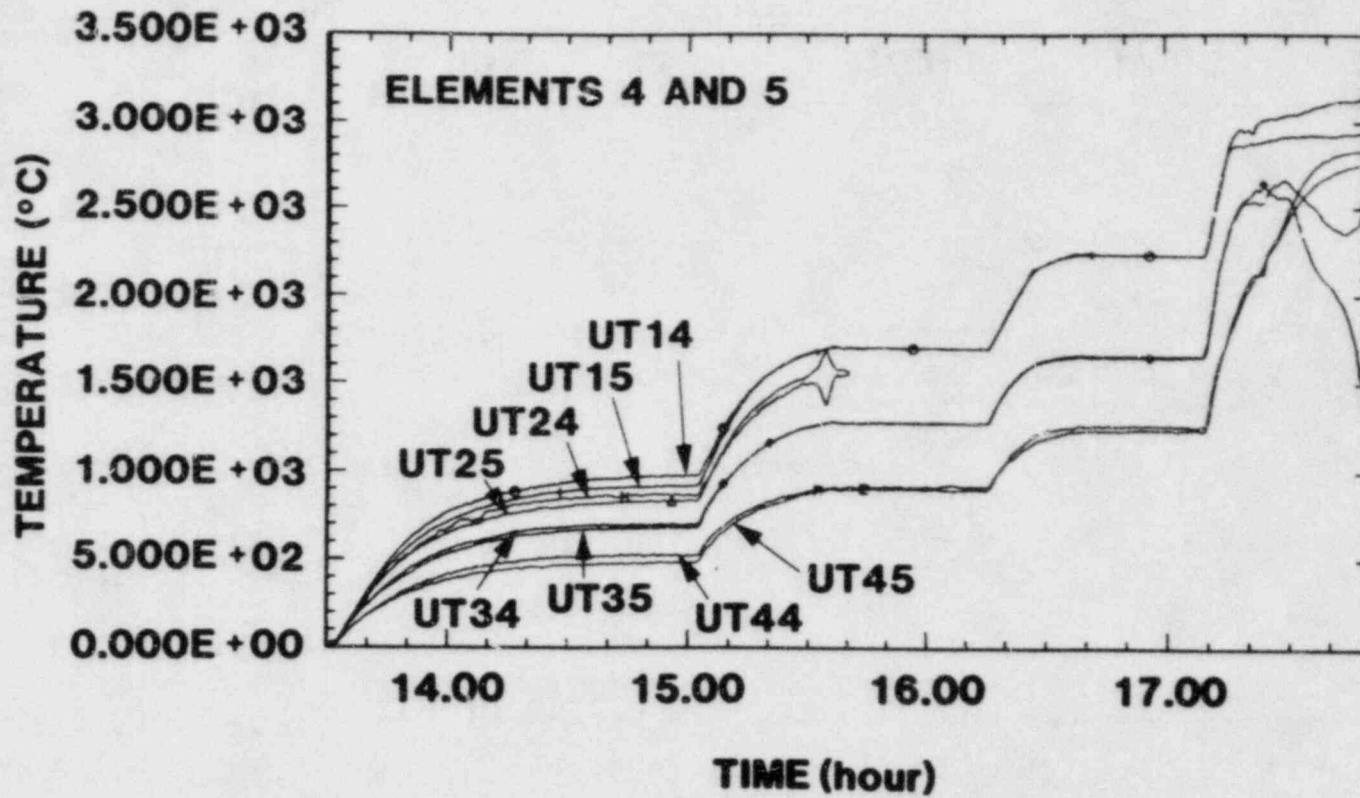


Figure 1.5-6. Ultrasonic Thermometer Data

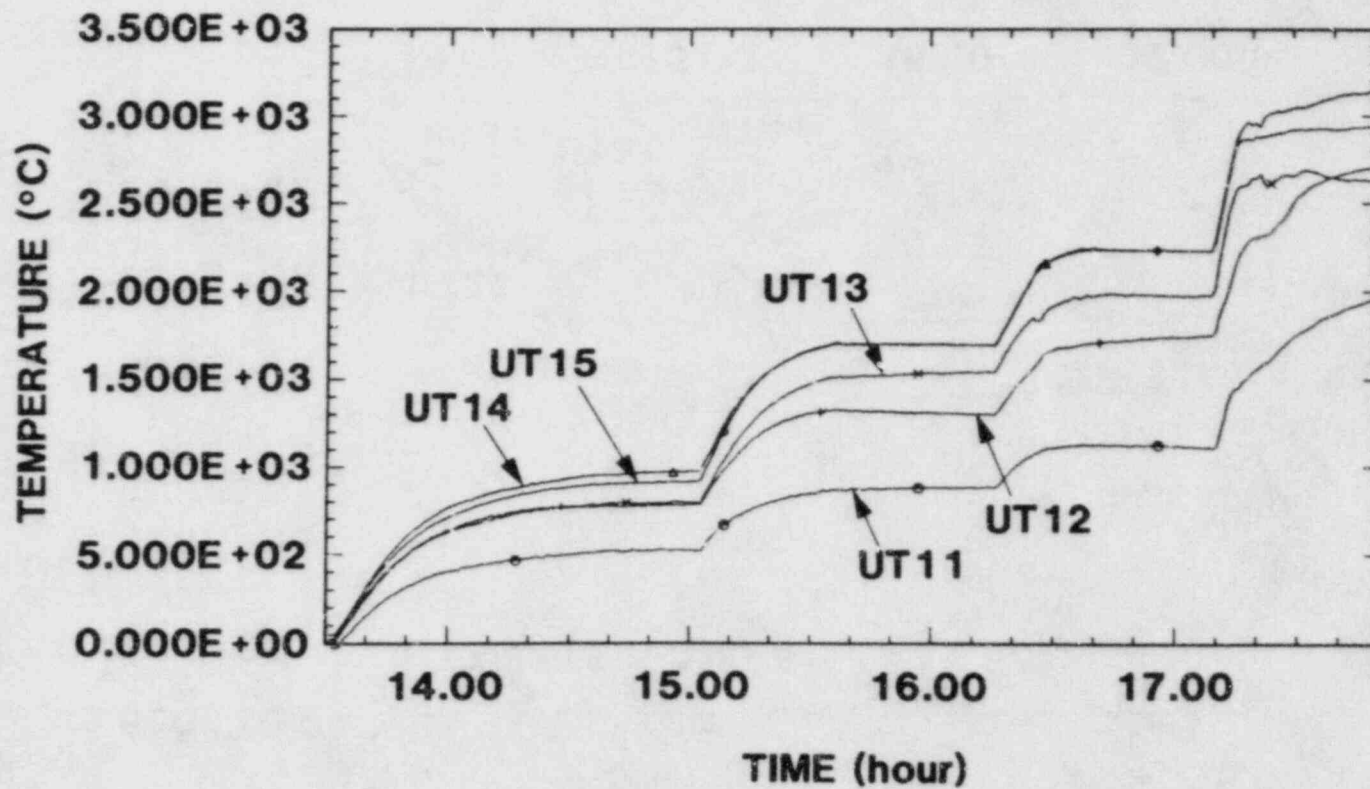


Figure 1.5-7. DC 1 UT1 Temperature Data

Table 1-IV  
Steady-State Thermocouple Data

Time (hr)	Thermocouple Temperatures (°C)				
	15:00	16:10	17:04	18:30	19:55
Reactor Power (kW)	100	225	345	127C	225
Bed Power (kW)	0.39	0.97	1.55	5.46	0.97
TC No.					
TC1	925	1656	2141	--	--
TC2	529	960	1277	--	--
TC3	468	797	1013	2172	831
TA11	133	290	426	1366	253
TA12	132	289	425	1365	253
TA13	133	289	424	1356	253
TA21	127	275	402	1287	241
TA22	128	275	403	1288	242
TA23	127	271	396	1257	238
TA3	121	257	373	1188	226
TA4	117	245	354	1122	216
TA5	115	227	321	963	198
TA6	115	229	328	995	206
SS11	114	206	282	720	200
SS12	109	197	267	683	191
SS13	108	196	266	671	191
SS14	95	173	238	641	175
SS21	88	158	215	564	154
SS22	80	142	191	504	137
SS23	76	133	179	488	129
SS24	74	128	170	450	124
PC1	78	132	175	494	132
PC3	75	130	172	482	132
PC4	73	128	171	495	131
PC5	60	107	148	486	99
PC6	67	120	165	528	115
HE1	32	36	37	64	32
HE3	44	66	83	202	62
ZR1	132	288	424	1364	329
ZR2	170	341	494	1412	354
ZR3	83	146	205	614	144
ZR4	55	91	122	363	87
OC1	42	62	76	180	70
OC2	49	77	98	249	83
OC3	43	62	77	190	65
OC4	44	67	83	190	75

Table 1-V

## Steady-State UT Temperature Data

Time (hr)	UT Temperatures (°C)			
	15:00	16:10	17:04	17:40 <sup>a</sup>
Reactor Power (kW)	100	225	345	1270
Bed Power (kW)	0.39	0.97	1.55	5.46
UT No.				
UT11 <sup>b</sup>	526	880	1120	1870
UT12	782	1303	1741	2650
UT13	796	1534	1971	2653
UT14	975	1699	2230	3106
UT15	914	1696	2230	2927
UT21	485	--	--	--
UT22	700	--	--	--
UT23	796	--	--	--
UT24	864	--	--	--
UT25	830	--	--	--
UT31	448	752	963	1750
UT32	558	960	1273	2371
UT33	635	1166	1555	2890
UT34	695	1273	1646	2440
UT35	677	1270	1655	2100
UT41	400	668	880	1770
UT42	440	785	1070	2256
UT43	483	831	1142	2680
UT44	522	917	1234	2780
UT45	480	893	1253	2680

<sup>a</sup>UTs failed shortly after this time.

<sup>b</sup>Indicates element 1 of UT1.

## 1.6 REFERENCES

- 1-1. T. Y. Chu et al, Quick-Look Report on a Large-Scale Test of  $UO_2$  Melt Interactions with Magnesia, NUREG/CR-3438, SAND83-1692 (Albuquerque, NM: Sandia National Laboratories, 1983).
- 1-2. R. A. Sallach, The Sodium Hydroxide-Rich Corner of the  $(Na^+, Ca^{2+}) (OH^-, CO_3^{2-})$  Reciprocal System, NUREG/CR-3269, SAND82-1980 (Albuquerque, NM: Sandia National Laboratories, 1983).
- 1-3. E. Randich and R. U. Acton, Intermediate-Scale Tests of Sodium Interactions with Calcite and Dolomite Aggregate Concretes, NUREG/CR-3401, SAND83-1054 (Albuquerque, NM: Sandia National Laboratories, 1983).
- 1-4. H. R. Westrich, H. W. Stockman, and A. Suo-Antilla, Laboratory-Scale Sodium Carbonate/Concrete Interactions, NUREG/CR-3401, SAND83-1502 (Albuquerque, NM: Sandia National Laboratories, 1983).

## 2. HIGH-TEMPERATURE FISSION-PRODUCT CHEMISTRY AND TRANSPORT

(R. M. Elrick, 6422; R. A. Sallach, 1846)

The purpose of the High-Temperature Fission-Product Chemistry and Transport program is to obtain data on the chemistry and processes that effect the transport of fission products under accident conditions. An experimental facility has been built to allow the chemistry of fission products in prototypic steam-hydrogen environments to be studied. The interaction of fission products with reactor materials such as stainless steel is also examined. Results of these experimental studies are compared to predictions of thermochemical models to determine if reaction kinetics play an important role in fission-product transport.

The experiment series to examine the behavior of tellurium vapor over reactor materials continued with the first test to study the reaction of tellurium with stainless steel in a steam-hydrogen environment. Also, analysis continued on the series of completed experiments with cesium hydroxide or cesium iodide vapor over 304 stainless steel or Inconel 600 in the presence of steam and hydrogen.

## 2.1 REACTIONS OF TELLURIUM VAPOR WITH STAINLESS STEEL

As shown in earlier studies, when tellurium vapor is exposed directly to the alloy 304 SS, the tellurium reaction still proceeds at a rapid rate, although slower than that between the vapor and Inconel 600. These experiments were conducted in a microbalance apparatus with the tellurium vapor, in an argon carrier, flowing over a 304 SS coupon suspended from the balance. Slight preoxidation of the coupon slowed the reaction rate. The goal of the present study is to determine to what extent the presence of steam with the concurrent oxidation of the alloy surfaces affects the rate at which tellurium reacts and the importance of temperature and environment on the decomposition of the tellurides.

The experimental arrangement for these steam tests is shown in Figure 2.1-1. Steam heated to 1100 K (827°C) entered the reaction chamber, mixing with tellurium vapor from a crucible heated to 970 K (697°C) (~15-torr vapor pressure of tellurium). The entrance section of the reaction tube was lined with alumina to allow the steam and tellurium vapor time to mix before bringing them into contact with the stainless steel. Preweighed steel bands and coupons lined the remaining 40-cm length of the reaction tube. At an average flow velocity of 10 cm/s, the reaction or residence time in the tube was about 4 s. The test lasted about 3 hr with the tellurium at temperature; previously, steam flowed through the system for about 1 hr.

Posttest analysis of the coupons by X-ray fluorescence gave no indication of the presence of tellurium. Either tellurium did not react with the oxide layer, or the reaction was so slight or so deep within the oxide that the fluorescence was not recorded. Additional analysis will examine the oxide layer in cross section for the presence of tellurium.

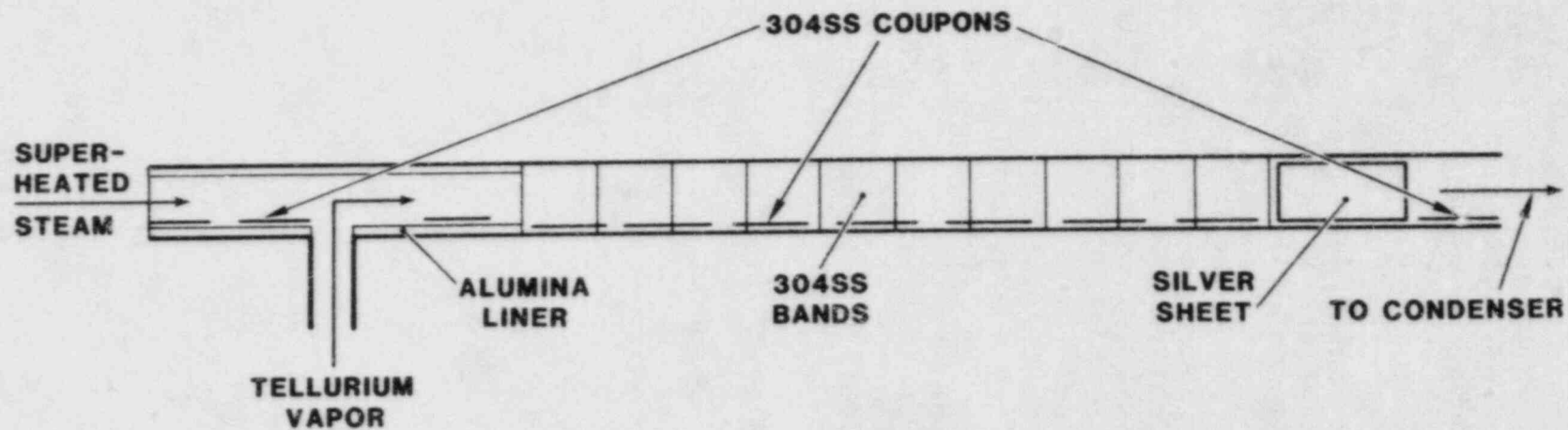


Figure 2.1-1. Reaction Tube in the Fission-Product Reaction Facility Configured To Examine the Interaction between Tellurium Vapor and 304 SS in Steam at 1100 K (827°C)



## 2.2 REACTIONS OF CsOH WITH STAINLESS STEEL

In the vapor experiments with CsOH in steam, the surface composition of the oxide formed on 304 SS had been altered by the presence of the vapor. Some features of this reaction have been studied by electron microprobe and X-ray fluorescence. Results of the analysis from the CsOH-over-304 SS tests are discussed below.

In a series of three experiments, CsOH was vaporized and injected into steam that flowed through the uniformly heated 304 SS reaction tube. Coupons of 304 SS, positioned along the reaction tube and lined with a 304 SS sheet, were removed after the test. Their surfaces were examined by electron microprobe and X-ray fluorescence for elemental composition of the surface and near surface. The experiments were performed at steam temperatures of 970, 1120, and 1270 K (697°, 847°, and 997°C); reaction tube temperatures were the same as steam temperatures.

Observed deposits of cesium on the 304 SS surface are divided into three categories: concentrations or particles containing cesium that can be resolved in elemental scans by the microprobe (>3  $\mu\text{m}$  in size); deposits of cesium that appear uniformly distributed on the surface and can be removed by a water wash; and uniform deposits of cesium that have been retained on or in the surface layer and are not removed by a water wash. These amounts of cesium are referred to as P, U, and R, respectively.

Since the X-ray fluorescence signal is averaged over an 8-mm-diameter area of the sample, the recorded cesium level represents all the cesium on the sample, before a water wash, from P, U, and R. Sample areas without apparent particles were chosen for microprobe counts to give a measure of the R and U cesium levels. The washed sample gives a measure of the retained or reacted cesium, R. Figure 2.2-1 summarizes the amounts of cesium detected in the three categories for the 1120 K (847°C) test (Test 15). As-received coupons placed along the reaction tube as shown in the figure were analyzed for these data. The middle coupon was washed before microprobe analysis. A small amount of cesium was found to have reacted with the steel. Several times this amount was absorbed but was easily removed with a water wash. Large area surface scans by microprobe for element composition (Figure 2.2-2) show particle-like concentrations on the coupon (15.13) farthest downstream that contain cesium, phosphorus, manganese, and nickel. The last three elements are found in the stainless steel. No particles at all were found on the coupons upstream of the injection point of CsOH, indicating that the cesium is an essential ingredient for the formation of particles. Particle number density (Figure 2.2-2) is  $2 \times 10^3$  particles/cm<sup>2</sup>; the particles range in size from about 3 to 12  $\mu\text{m}$ . If particles were initially present on the middle

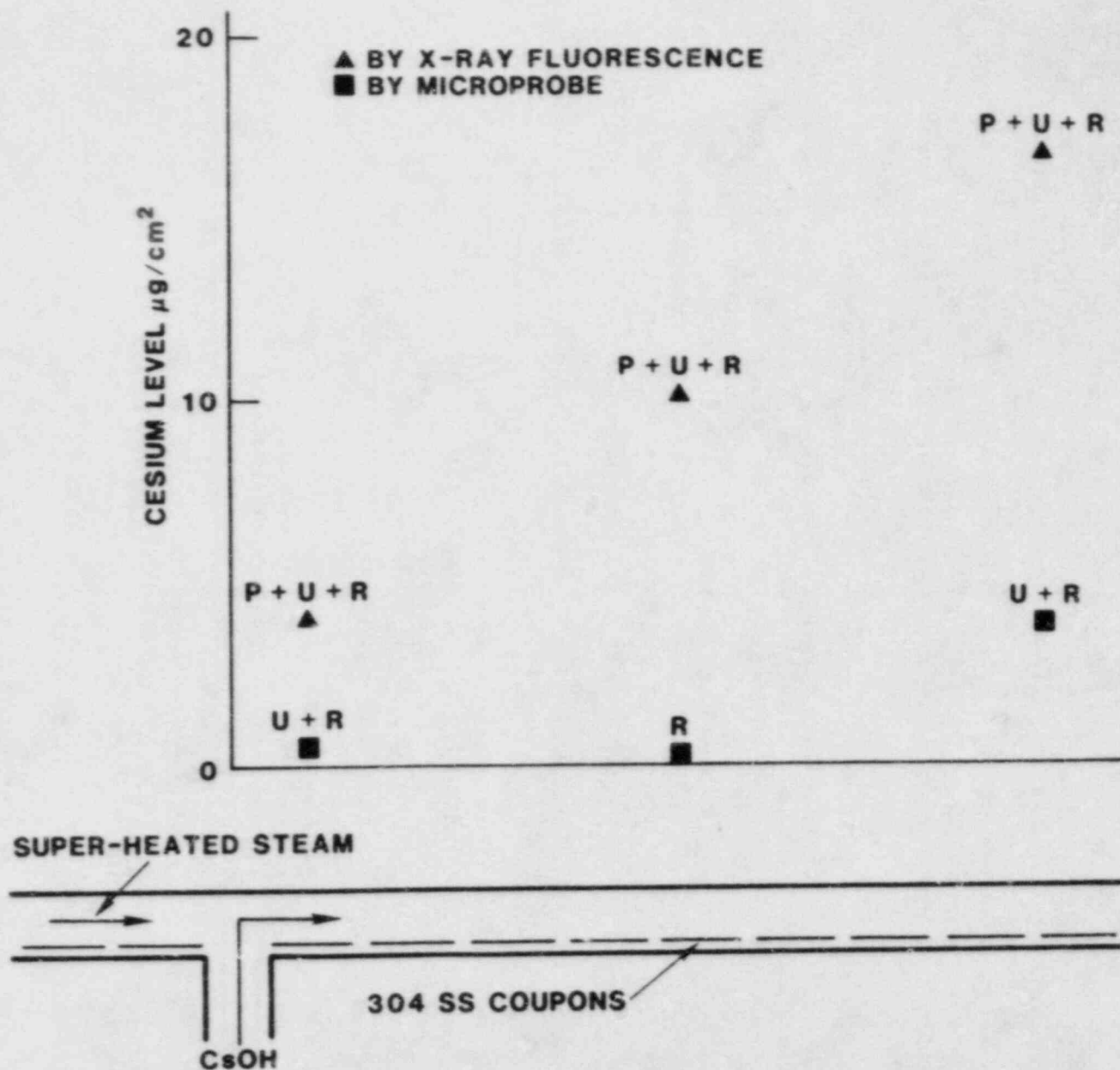
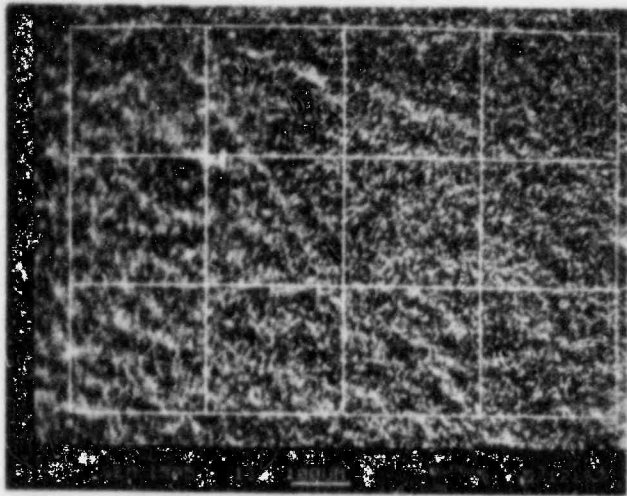
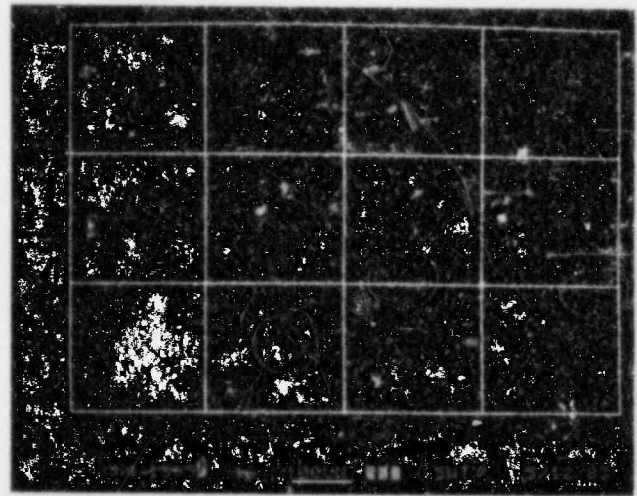


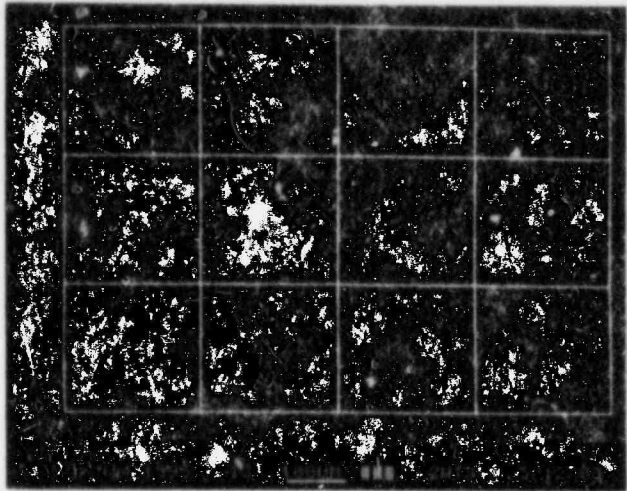
Figure 2.2-1. Cesium Levels Measured by Electron Microprobe and by X-Ray Fluorescence on 304 SS Surfaces: for Particles (P), as Reacted Species (R), and in a Form Removed by Water (U) (Test 15)



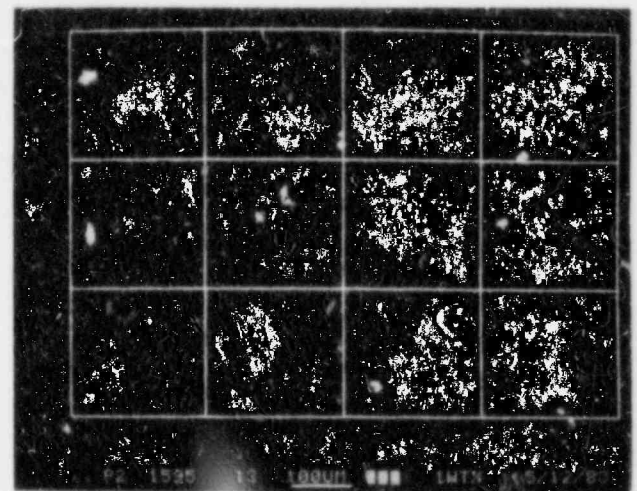
SEM



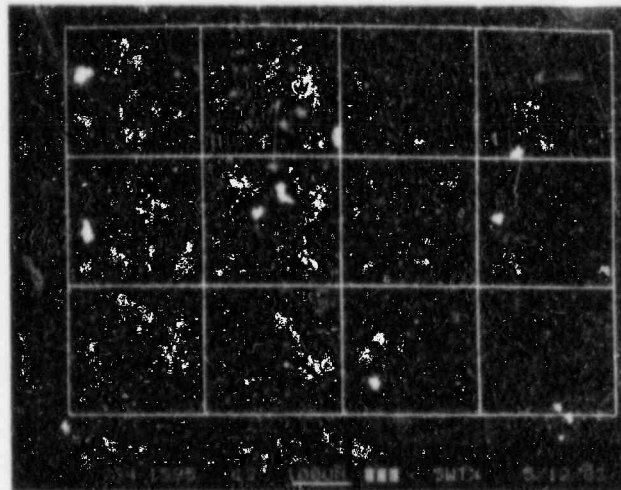
MANGANESE



NICKEL



PHOSPHORUS



CESIUM

200  $\mu$ m

Figure 2.2-2. Electron Microprobe Scans on Coupon 15.13 for Manganese, Nickel, Phosphorus, and Cesium

coupon, they were removed in the water wash. No particles with this composition were seen on the first coupon exposed to CsOH. If these particles exist, they must be less than  $\sim 3 \mu\text{m}$  in size. A possible explanation for the formation of the particles is that the cesium vapor reacted with vapor species of the other elements in the stream, condensed into particles, and collected on the tube surfaces.

A deposition velocity\* or surface reaction rate can be calculated for each of the three categories of cesium deposit. Since the mass of deposited particles does not show the characteristic decrease with time (with distance down the reaction tube), the usefulness of the calculation would be restricted to the specific experimental geometry. However, the observed particle formation demonstrates an important and apparently complex mechanism of vapor species reaction, condensation, and deposition for removal of fission products from the transport stream. Average values for U and R, as observed by the microprobe and shown in Figure 2.2-1, were used to calculate approximate surface reaction rate constants. Since microprobe analysis explores a layer about  $1 \mu\text{m}$  thick, it was assumed the cesium was uniformly distributed throughout the oxide. The oxide thickness was calculated from the coupon mass gain and density for  $\text{Fe}_3\text{O}_4$  to be about  $33 \mu\text{m}$ . The rate constants were  $2.6 \times 10^{-6} \text{ m/s}$  for the amount of cesium that was removed by a water wash and  $1.6 \times 10^{-4} \text{ m/s}$  for the amount of cesium that reacted with the steel.

Similar results were obtained at 970 K (697°C) (Test 10) where particles up to  $10 \mu\text{m}$  in size were collected on the first coupon downstream of the injection of CsOH. Further downstream (within several seconds), the particles increased in size to  $25 \mu\text{m}$ . This time, microprobe scans showed cesium and chlorine as the major elements in the particles. The origin of the chlorine is unknown but could have come from the organic binder in the asbestos seals. The distribution of cesium among the as-received coupons measured by microprobe and X-ray fluorescence is shown in Figure 2.2-3. Average values for U and R, as measured by microprobe, were used to calculate rate constants; the oxide thickness was calculated to be  $\sim 4 \mu\text{m}$ . For a uniform distribution of cesium in the oxide, the surface reaction rate constant for U is about  $7.3 \times 10^{-4} \text{ m/s}$  and for R is about  $4.4 \times 10^{-5} \text{ m/s}$ .

---

\*For slow reactions (when the reaction rate, and not mass transfer of species to the surface, controls the reaction), deposition velocity, as defined by Battelle [2-1] is approximately equal to the surface reaction rate. All reactions discussed here were "slow," so the Battelle method has been used.

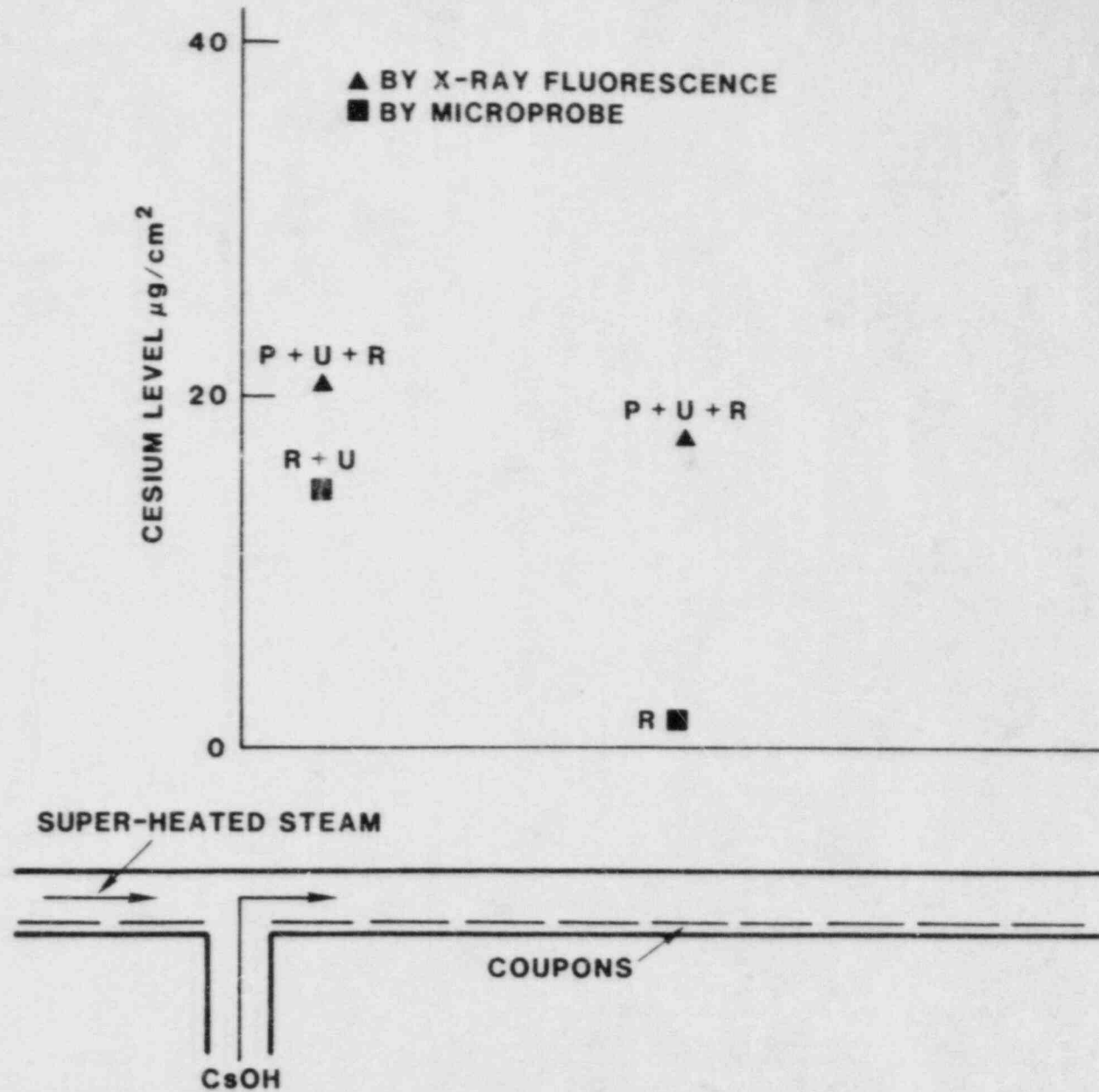


Figure 2.2-3. Cesium Levels Measured by Electron Microprobe and X-ray Fluorescence on 304 SS Surfaces: for Particles (P), as Reacted Species (R), and in a Form Removed by Water (U) (Test 10)

In the 1270 K (997°C) test (Test 19) with CsOH, particles up to 40  $\mu\text{m}$  in size were observed. Primary elements in the particles were cesium and aluminum. The source of the aluminum is unknown but is a minor constituent of Inconel, the superheater material. The distribution of cesium on the coupons is shown in Figure 2.2-4 as measured by microprobe and X-ray fluorescence. No rinsed samples were examined, but a small amount of cesium (<0.2 ppm) was in the water used to rinse the reaction tube liner; it was assumed essentially all the detected cesium reacted with the steel. The corresponding reaction rate constant is  $1.9 \times 10^{-5}$  m/s, based on a uniform distribution of cesium throughout the 65- $\mu\text{m}$ -thick oxide layer.

The primary oxide formed on the steel in the three tests was an  $\text{Fe}_3\text{O}_4$ -based spinel. Of the 13 elements detected by microprobe as being present near the sample surface ( $\sim 1 \mu\text{m}$  in depth), 9 are initially present in the steel (Cu, Cr, Mn, Fe, Ni, Si, S, Mo, and P). Two elements were detected in trace amounts. The others (Si, S, Cl, Cr, P, Mn, Ni, Mo, Al) were in concentrations of about 1% or less with the exception of Fe, which makes up 65 to 70 wt/% of the oxide layers, and Mn, present at about 4%. The addition of cesium to the steam stream has the general effect of decreasing the surface concentration of Cr and Mo and increasing the surface concentration of Si and Fe. Trends for the other elements follow no discernible pattern. There was no evidence that cesium combines to a significant extent with the major constituents of 304 SS.

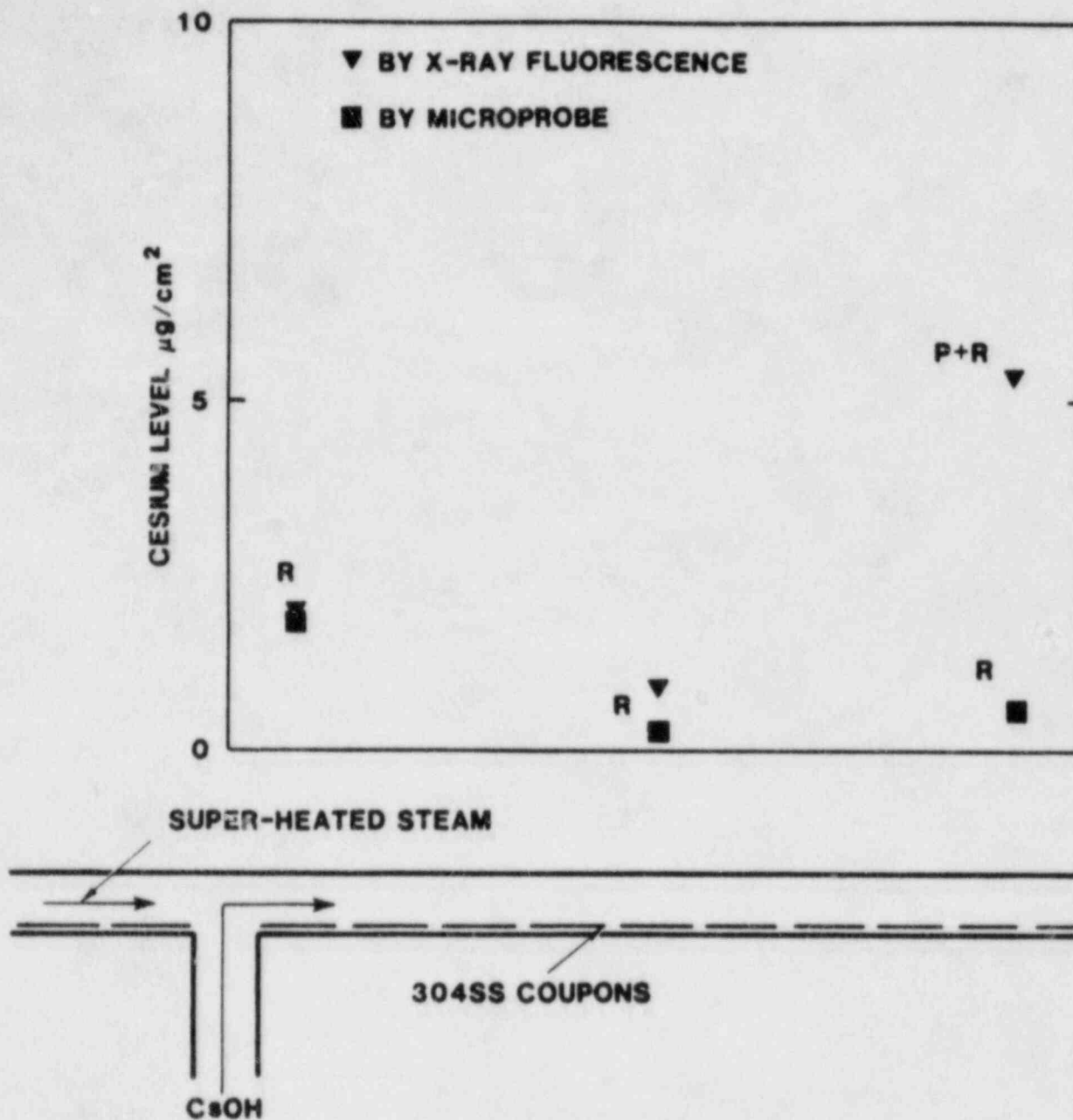


Figure 2.2-4. Cesium Levels Measured by Electron Microprobe and by X-ray Fluorescence on 304SS Surfaces: for Particles (P) and as Reacted Species (R) (Test 19)

### 2.3 REFERENCE

- 2-1. H. Jordan, J. Gieseke, and P. Baybutt, TRAP-MELT Users Manual, NUREG/CR-0632, BMI-2017 (Columbus, OH: Battelle Columbus Laboratories, February 1979).



### 3. CONTAINMENT ANALYSIS

(K. D. Bergeron, 6424; P. Rexroth, 6424; K. Murata, 6424; M. E. Senglaub, 6424; F. W. Sciacca, 6424; W. Trebilcock, 6424)

The Containment Analysis programs are centered on the development, testing, and application of the CONTAIN code. CONTAIN is NRC's general-purpose computer code for modeling containment response to a severe accident and provides detailed mechanistic models of phenomena that occur outside the reactor primary system and inside the reactor containment building. The phenomena include interactions between core debris and coolant or concrete, hydrogen combustion, thermal hydraulics of the gases in the various compartments of a containment building, aerosol behavior, and fission-product transport and decay. CONTAIN provides models for LMFBR and LWR containment systems. Major parts of CONTAIN are operational and are being extensively tested and applied to reactor accident analyses.

For core-disruptive accidents in an LMFBR, the code provides models for the thermal hydraulics of the cell atmospheres; heat transfer to and vapor condensation on structures in the cells; sodium-spray fires; chemical interactions of sodium vapor and aerosols; hydrogen combustion; aerosol transport, agglomeration, and deposition; and radioisotope transport and decay. The reactor-cavity debris-pool model is partially completed and can model sodium-pool fires and core-debris/concrete interactions. The sodium/concrete interactions model is complete but has not been fully tested.

For severe accidents in an LWR, the code provides models for core-debris/concrete interactions; cell-atmosphere thermal hydraulics; containment sprays; structure-heat transfer; steam condensation on structures and on aerosols; hydrogen combustion; aerosol transport, agglomeration, and deposition; and radioisotope transport and decay.

### 3.1 CONTAIN CODE DEVELOPMENT

#### 3.1.1. MEDICI, LWR Reactor Cavity Model

Pool boiling forms a critical coupling between the reactor-cavity pool and the atmosphere. The boiling of the pool and the attendant mass and heat transfer affect the pressure, and the boiling rate depends on the rate of change of the pressure. With such a strong feedback loop, it is desirable not to treat the interface explicitly, but rather to solve for the thermodynamic conditions and the mass and heat transfer self-consistently. The approach used in MEDICI is to identify all sources contributing heat and mass to the pool and atmosphere and to classify them as "explicit" or "implicit." Explicit sources will be calculated from the start-of-timestep values, and the rates are assumed constant throughout the timestep. Implicit sources are those having rates that must be determined self-consistently with the solutions of the mass, energy, and atmosphere thermodynamics equations. The categorizing process is guided by the trade-off between the complexity of the solution algorithm and its numerical stability. The treatment to be used for the first version of MEDICI is:

##### Implicit sources:

1. flow -- at least with respect to conditions in the cavity
2. boiling

##### Explicit sources:

1. condensation/evaporation on structures
2. oxidation
3. core/concrete interactions
4. quench of hot debris
5. decay heat from the rubble bed
6. volumetric decay heat from fission products in the pool
7. convection from pool or atmosphere to structures
8. liquid flow paths (pipes and drains)

A method for solving the mass- and energy-balance equations that treats gas flow, boiling, and air-steam thermodynamics self-consistently has been developed for MEDICI. Because of the tight coupling between the pool and the atmosphere during boiling, this routine solves for mass and heat

transfer between the pool and the atmosphere self-consistently with a two-phase thermodynamics calculation for the steam-air mixture in the atmosphere.

The M2 (debris bed) portion of MEDICI with the new quench model was integrated into the code and checked with previous stand-alone quench calculations. The integration of the new quench model into MEDICI involved some logic changes to the main program, input changes, and partial coding of an M2 (debris bed) subroutine to call the quench model. Several improvements were then added to the water-level calculation in M2. These improvements included allowing for level swell caused by the steam generated from decay heat and the addition of an iterative solution for the water level to improve accuracy.

A sample calculation for the debris bed quench model has been formulated and run for incorporation into a paper for the San Francisco ANS conference. Two cases were considered: one has constant pressure, while the other exhibits a rising pressure that might be associated with a debris bed quench process in a closed volume. The effect of pressurization on the quench-front velocity is to delay the front.

A generalized output structure for both plot and print output was planned and then coded. This output routine was checked for various cases.

Representatives of the University of Wisconsin (UW) and Sandia met in Madison, WI to discuss progress on the MEDICI code. Most of the features needed for the first version of MEDICI are either operational or are expected to be operational by August 1. Modules requiring additional work include the expulsion of debris following a steam explosion, pool-atmosphere coupling, hydrogen generation in the exposed debris zone, and entrainment and sweepout in a high-velocity gas stream.

The process of merging the parts of the code developed at UW and at Sandia will be initiated in July and should be completed during a week-long visit by UW personnel to Sandia in August. Project personnel expect that a version of the code will be available for review by other Sandia organizations around October 1.

### 3.1.2. Simple Sodium Concrete Interaction (SSCI) Code

The necessary input information was assembled for verifying the SSCI code with data from tests AA/AB. These data were obtained from a test report.[3-1]

The code has been revised to account directly for the observation that 37% of the reaction debris in test AB was combined sodium. This results in a sodium/concrete reaction

ratio of 0.832 by weight. The previous model used a ratio of 0.70 that was obtained from the results of earlier tests. However, this previous ratio has an uncertainty of 20% associated with it. Because the 37% figure was obtained by chemical analysis, there is more confidence in it.

Two CRBR accident cases have been completed for inclusion as a sample problem in the final report of the SSCI Code. One case incorporates decay heat from a full power core with a 1000-s melt-through delay, and one case does not have the decay heat. Use of these cases will illustrate the effect of reaction-produced heat in comparison to the magnitude of decay heat.

A wall condensation model and a pool heater model were also added to the SSCI code to perform the comparison study. These conditions were required because of the sensitivity of the test configuration to small perturbations in the heat balance. In this regard, the concrete temperature gradient was modified to agree with the test data. However, this adjustment reflects the added effects of lateral heat loss from concrete, an effect that could be neglected with the massive geometry typical of the CRBR cavity. The inclusion of the wall condensation model has, in effect, added a lateral dimension to the heat transfer model in the vapor space above the pool. Some preliminary runs with the SSCI code that simulated tests AA/AB are encouraging, but the results suggest that further tuning of the pool heater model may be required. Experimental temperature data from the pool and the vapor space are the principal measurements with which comparison is made to code results. The present SSCI model has one constant concrete sink temperature specified, so no comparison can be made for the concrete.

Additional information has been obtained on the release of sodium by hydrogen bubbles bursting at the pool surface. A search on this subject uncovered some interesting but not very quantitative papers published in the 1950s. Several investigators agree that there are two separate mechanisms for drop formation on bubble burst: (1) breakup of the bubble film into many droplets in the range of 50- $\mu$ m diameter and (2) a few drops in the range of 1-mm diameter from the breakup of the ensuing jet. Jet breakup could not occur for bubble diameters greater than 9 mm in a liquid similar to sodium at 800 K (527°C). In reactor-cavity pools, the hydrogen bubbles are mostly greater than 9 mm; therefore, any significant contribution by bubble burst will be attributable to film breakup.

A feature was added to the code to facilitate making plots on the Tektronics 4014 with a DISSPLA routine that was also developed this quarter. This routine produces four plots from a plot data file written by the SSCI code. The plots include (1) temperature, (2) inventory of major reactants and

products, (3) evaporation and boiling rates, and (4) inventory of gases and vapors.

As code improvements are completed and verified, the revisions will be included in the SSCI document. The final version of the document should be updated and available for review in the next reporting period.

### 3.1.3. Aerosol Model

The modifications and improvements to the aerosol module obtained over the past few months were adapted to the most recent version of CONTAIN for incorporation into a new (Mod415) base file. The new base file is currently being tested.

### 3.1.4. Radionuclide Model

Development of the radionuclide transport model continued with the identification and correction of coding errors discovered during the Surry AB-sequence calculations.

### 3.1.5. Aerosol Vent Plugging

Vaughan's paper describing development of his vent plugging model was reviewed.[3-2] By developing a differential form of Vaughan's plugging model, a numerical scheme and a small computer code (named AEROPLUG) have been formulated. This code has been used to run typical cases of vent plugging and predicted a plugging time of 47 min for a 0.1-cm-radius tube with a flow velocity of 1 m/s and an aerosol concentration of 10 g/m<sup>3</sup>. This simple model is based entirely on inertial deposition and assumes a constant flow velocity and neglects the effects of the plug profile, length of tube, wall roughness, and entrance and exit effects. Other assumptions address constant parameters relating to plug cross-section profile, plug density, and collection efficiency. With these assumptions, the model is nearly linear, so plugging times are proportional to concentration, flow velocity, and tube radius. The flow rate equation for flow past the plug deposit can be integrated analytically. This could be useful for studying the effect of the arbitrary geometric parameters (which define the plug profile), but the resulting log terms are cumbersome.

### 3.1.6. LMFBR Reactor-Cavity Model

The transport mechanisms in the new LMFBR reactor-cavity model have been expanded and tested. In tests with convecting material, which has a definite profile, some numerical problems have been observed. In most numerical schemes, the implicit assumption is that material convected into a node enters with a uniform distribution. This assumption is not valid or adequate when used in conjunction with a numerical scheme such as the Asymmetric Weighted Residual (ASWR) method.

To mitigate this problem, the conservation equations used in the REBEL model were reformulated in terms of average properties and surface properties. This improved the numerical solution of the system of equations. The heat transfer problems that were originally used in the development of the scheme were then retested.

A major difficulty now becoming apparent stems from the high level of detail that the ASWR model can provide. Treating the complete general problem, which attempts to anticipate all scenarios in a reactor cavity, requires an arbitrary number of interfaces. This problem could probably be handled if generic materials were considered for each layer in the problem. Concrete layers would then consist only of concrete in the solution algorithms, with simple side calculations defining the compositions. Likewise, the solution algorithms in the debris region treat a material "debris" whose composition is defined via explicit side calculations. Such an approach could make the general problem more tractable, but whether the remaining major effort is justified is still uncertain. Alternative options involving simpler and less general treatments of sodium pool phenomena are being considered.

#### 3.1.7. Engineered Safety Features

The details of the CONTAIN ice-condenser model have been outlined, and the coding has begun.

#### 3.1.8. MELCOR Phenomenological Assessment

Several sections in the MELCOR phenomenological assessment were critically reviewed, and comments were sent to the authors. In turn, reviews of the sections written by members of the Containment Analysis staff were received from reviewers, and these comments were incorporated into the second draft of that document. The completed draft was sent to MELCOR personnel for transmittal to reviewers outside Sandia.

#### 3.1.9. FORTTRAN 77 Conversion and Other Code Improvements

A new CONTAIN base file (Mod415) has been generated. As an intermediate step toward the conversion of CONTAIN into FORTRAN 77 language, this new base file was processed through the CDC F45 conversion program. This program identifies FORTRAN 66 statements that are not compatible with the new compiler and generates an update file of new FORTRAN 77 statements. Each of these generated corrections has been screened to insure that the machine-generated code does not introduce ambiguous or incorrect program flow.

A copy routine has been written and integrated into the CONTAIN program file and into the job control procedures for

running CONTAIN. This routine produces a copy of the input files from the job stream on the output file of the job during its execution. This provides an exact image of the input file for comparison and documentation purposes on the job output.

With the installation of a bigger computer as Sandia's unclassified, timesharing computer, CONTAIN can now be compiled and run on this computer. The necessary code modifications and procedures were developed for running CONTAIN on this system. This will allow more efficient interactive development and execution of CONTAIN.

A set of guidelines that establishes and explains coding conventions used in CONTAIN has been written. These conventions will be implemented during the FORTRAN 77 conversion and will guide future modifications to the code. Additionally, a set of guidelines has been set up for immediate documentation of code modifications, which will help speed up the process of code integration, checking, and debugging. This data management system was developed to provide a smoother integration of individually developed changes into the CONTAIN code. In previous code updates, certain changes introduced into the system by one code developer may have produced surprising impacts upon the results of other code developers. Under the new management system, the changes that each code developer has proposed as permanent changes to CONTAIN are collected periodically and maintained in a designated file. Other developers and users of the code can access this file and compare their results with and without these changes. This "curing period" is intended to allow all errors and conflicting coding to be identified and eliminated before the changes are placed in the permanent code.

## 3.2 CONTAIN TESTING AND VALIDATION

### 3.2.1 Testing

The performance of the current version of the CONTAIN code is currently being evaluated against the performance of previous versions. Of the numerous tests that have been used to test and validate the response of the code in the past, certain ones have been selected and designated as "standard tests." These standard tests are intended to be a routine quality control procedure to check new major revisions of the code.

Three new tests have been designated as standard tests, and one of the previous standard tests has been replaced by a new test that encompasses the objectives of the old test. The new test also evaluates the response of the new condensation coding within CONTAIN.

### 3.2.2 Test Documentation

Output for all 16 of the designated "standard tests" has now been reproduced on microfiche for easier retention. All tests were run on the current version (Mod415) of CONTAIN, and the output retained on microfiche includes an exact copy of the input deck, necessary temporary changes, the code-generated output, and appropriate plots of the output. Code developers intend that microfiche files of all standard tests be maintained for all future versions of CONTAIN.

Reports on tests AB-01 and AB-02 of the aerosol module were prepared for inclusion in the forthcoming report on the testing program. The AB-01 test is a qualitative test that compares CONTAIN results to the NSPP 207 dry aerosol experiment and to HAARM results for the experiment. The AB-02 test compares CONTAIN numerical methods and models in detail to ones from the QUICK code and constitutes the verification of the numerical methods used in the CONTAIN aerosol module. These tests are at the qualitative and verification levels only. Detailed experiment comparisons and predictions are beyond the scope of the forthcoming report on the testing program but will be addressed in other forthcoming reports and conference papers.

The report describing the results of the CONTAIN test efforts completed thus far has been completed in final form. All outstanding test reports were received and were incorporated into the overall report.

### 3.2.3 Tests Running on Interactive Operating System

All of the CDC Fortran compiler (FTN5) errors have been successfully removed from all of the proposed changes to CONTAIN, Mod415. One of the standard tests was executed on



the CDC Cyber 170/855 under NOS2 and represents a milestone toward developing a capability to execute CONTAIN interactively. The NOS2 execution was accomplished without the use of the CDC overlay structure. However, an attempt to execute the integrated standard test, ZT01, was unsuccessful, apparently because the amount of output from this test was in excess of the file limitation within NOS2. Apparently this interactive capability cannot be readily extended to handle all applications of CONTAIN, but it can be used in code development and the start-up and input debugging of applications.

#### 3.2.4 Validation

Aerosol calculations have been carried out in support of the upcoming ABCOVE AE-6 experiment. The AE-6 test will be a two-component sodium oxide-sodium iodide experiment designed to differentiate between multicomponent codes like MAEROS and MSPEC, and single-component, multimaterial codes like HAA-4 and NAUA. Scoping calculations were carried out using CONTAIN and comparisons made of the multicomponent treatment and the single-component treatment. Project personnel found that under the proposed experimental conditions, significant differences in code predictions should result just from the different treatment of components and that the experiment should satisfactorily demonstrate that the multicomponent treatment is needed.

The modeling of the NSPP aerosol experiments in steam environments is continuing. These calculations will be done using the new version of CONTAIN; however, a few modifications are still required before the calculations can proceed.

### 3.3 CLINCH RIVER CONTAINMENT ANALYSIS

CONTAIN input data decks were prepared which model the CRBRP melt-through scenario. The input has been modified to include simulation of the sodium/concrete interaction expected to occur in the reactor cavity. At present, this is being modeled as a chemical reaction occurring in the pool. Initial checks indicate that the appropriate amount of energy from this reaction is being added to the pool and that appropriate amounts of hydrogen gas are being released to the reactor cavity cell. For the output purposes, the investigators have run cases where the initial sodium pool temperature is specified to be near the boiling point. Boiling phenomena are initiated early in these problems, exercising more of the code subroutines. This was done to evaluate the code's handling of this complex accident scenario. These tests indicated that problems in calculations were occurring once boiling started. The presence of sodium vapor in the cell atmosphere resulted in unexpected chemical reactions. Investigations of this problem revealed that it was caused by improper storage locations within the code for certain materials that could react. This problem has been corrected with appropriate updates.

Checks of the pool-to-atmosphere heat transfer for a typical reactor-vessel melt-through scenario revealed that the amount of heat transferred was unrealistically high for the specified atmosphere and pool conditions. The high heat transfer was due to a hard-wired pool-to-atmosphere heat transfer coefficient. In order to improve this aspect of the code, the appropriate routines within CONTAIN were modified to calculate this coefficient based on the pool and atmosphere conditions. The revised coding assumes that the pool is a flat plate with appropriate Nusselt numbers being calculated for the atmosphere-pool system within each cell, based on the direction and magnitude of the temperature gradient. Heat transfer coefficients are then calculated. The CONTAIN results obtained with this revised coding are much more realistic than those obtained prior to the modifications.

Additional checks have been made of CONTAIN's treatment of fission-product heating and chemical heating of pools. For the CRBR problem, checks at specific time points showed that the rate of sodium boiloff from the pool in the reactor cavity was in good agreement with the amount expected from fission-product decay heating and sodium/concrete interaction heating effects. This investigation also checked the effect of condensation on the net loss of sodium from the pool. When the condensation option is employed for the reactor cavity, a large percentage of the sodium vapor leaving the pool condenses on the cavity walls and structures. The coding specifies that the bulk of this condensate will subsequently re-enter the pool. For early times in the melt-through problem, the walls are cool and the condensation is significant. The condensate entering the pool under these conditions is a large

fraction of the total amount of sodium vapor leaving the pool. This substantially reduces the net rate at which sodium is lost from the pool.

### 3.3.1 CRBR Radionuclide Inventory Evaluation

Quantitative information on the radioactive material inventories in the CRBR core (core and blankets) was recently received.[3-3] In addition, the project provided information on the actinide inventory present in the reactor. Following a review of the CRBR core fission-product and actinide inventories, which apply to an end-of-equilibrium-cycle core, all isotopes with significant activity and those with particularly significant health effects were noted for inclusion in the CONTAIN input data file for the CRBR analysis. Information was collected on the activity, half-life, decay modes, and decay energies of these isotopes. All significant decay chains were also identified and noted. Efforts were initiated to put this information in the format needed by CONTAIN. This will allow a more accurate and realistic assessment of the transport of radioactive materials following a melt-through event.

### 3.3.2 Additional Sodium Vapor Production from Bursting H<sub>2</sub> Bubbles

As mentioned earlier, any significant contribution by bubble-burst in the case of hydrogen bubbling through sodium will be due to film breakup. Experimental data from release of droplets by bubble film breakup have been reported.[3-4] If this can be used as a guide for the hydrogen-sodium system, 0.01 g/s can be expected in the case of the large spill into the CRBR cavity. This mass is 1% of the release of saturated vapor carried inside the bubbles and less than 0.04% of the surface evaporation. Thus, this source is not significant on a mass basis but may be so as an aerosol source, 500 particles/cm<sup>2</sup>-s.

### 3.3.3 Draft FY84 Research Plan

Programmatic guidance was received for the CONTAIN Code Applications program for FY84. The CRBR-specific analyses will be performed as part of this program. A draft has been prepared for this program.

The objective of this program is to adapt the CONTAIN code to accommodate specific advanced reactor containment systems and to conduct selected safety-related analyses of these containment systems. To accomplish this, a review and assessment will be made of pertinent phenomena expected to play a significant role in severe accidents in advanced reactors. CONTAIN's capabilities for modeling and treating these phenomena will be evaluated. Where the coding is found to be weak or deficient, improvements and adaptations will be made

to the code so that key phenomena can be suitably accounted for in the analyses. Design-specific accident analyses will then be conducted for selected accident scenarios. In particular, the way in which the CRBR containment system responds to severe accidents will be studied.

The overall emphasis of this program will be the analysis of severe accident challenges to the CRBR containment system. One objective is to test the adequacy of the CONTAIN code for applications such as this. A second objective is to provide valid and useful technical information to the NRC for use in evaluating the adequacy of the CRBR containment system.

Although the primary focus of the efforts will be the CRBR, other advanced reactor systems may also be studied. However, the results obtained using the CRBR as the model will likely be very useful in evaluating other systems. This will be the case unless the containment systems or accident scenarios envisioned for other advanced reactor systems differ considerably from those associated with the CRBR.

### 3.4 LWR CONTAINMENT ANALYSIS

#### 3.4.1 Coagulation in Containment-Blowdown Plumes

Previous work included analyses that showed that under some conditions, turbulence-induced coagulation in blowdown plumes may substantially increase the effective particle size for radionuclides released in certain LWR accident sequences involving containment failure caused by steam overpressurization. Two approaches were used. In the first, a simplified analytical treatment was employed in which the problem was treated as a single large particle of diameter  $D_1$  interacting with an aerosol composed of smaller particles of diameter  $D_2$ . In the second, sample MAEROS calculations for a more realistic lognormal particle-size distribution were performed. These two results were compared with good agreement.

Unfortunately, both the simplified analysis and the modeling in MAEROS involve physical approximations that can fail badly in the present problem. Essentially the same approximations are involved in other aerosol codes, and therefore these cannot be used to provide improved analyses. Hence, a series of scoping calculations were carried out using the two-particle-size model after incorporating certain refinements into the treatment. These refinements include the following:

1. Stokes' Law substantially overestimates the particle relaxation time,  $\tau$ , for larger values of  $D$  or the turbulent energy dissipation density,  $\epsilon$ , or both. More realistic values of  $\tau$  were obtained using procedures outlined by Reference 3-5.
2. When  $D_2/D_1$  is small, the collision efficiency is much less than unity. Unit collision efficiencies were assumed in the previous work. In the present treatment, collision efficiencies for interception and impaction were estimated using relations given by Reference 3-5. Relations given for viscous flow around the larger particle were used when the large-particle Reynolds number,  $Re_1$ , was less than or equal to 0.1, relations given for potential flow were used for  $Re_1$  greater than or equal to 50, and a (quite arbitrary) logarithmic interpolation procedure was employed for the immediate regime. Collision efficiencies were assumed to be unity when  $D_2/D_1$  is greater or equal to 2.
3. The basic formulation is valid only when  $t < \tau = (v/\epsilon)^{1/2}$ , where  $v$  is the kinematic viscosity. <sup>0</sup>For the very large values characteristic of the present problem, this assumption can fail for  $D$  greater than or equal to 1  $\mu\text{m}$ . A rough correction was applied based upon the assumption that a particle responds

only to accelerations corresponding to the portion of the turbulent eddy spectrum having characteristic time scales greater than  $\tau$ .

These treatments were incorporated into a numerical model for the rate of growth of the large particle that was then integrated numerically using the variable-order Adams integrator DEABM.

All three of the effects noted above proved very important. The results of the calculations show significant sensitivity to the remaining uncertainties in the second and third of these effects, and additional refinements in the treatment might be needed for reliable calculations. The current modeling of the first effect (particle  $\tau$  values) is believed to be adequate.

The results that have been obtained reveal that very substantial particle growth (to final sizes of the order of a few tens of micrometers) is to be expected for at least some realistic values of the relevant parameters. However, the final particle size that may be attained is quite sensitive to the values of these parameters. Some of these sensitivities are:

1. The degree of particle growth obtained depends quite strongly upon both the size of the largest particles initially present ( $D_1$ ) and the average size of the distribution ( $D_2$ ).
2. Agglomeration increases with increasing size of the blowdown jet; i.e., with increasing values of the containment-failure-rupture radius  $r_0$ . Decreasing  $r_0$  to 0.05 m decreased maximum particle sizes by factors of 2 to 5.
3. Decreasing the jet velocity from 400 to 200 m/s decreased maximum particle sizes by factors of 2 to 3.
4. Varying the aerosol density,  $f_p$ , a factor of 2 in either direction results in corresponding variation in maximum final particle size by factors of 2 to 5.
5. The above sensitivities are largest when the calculated growth in the particles is the largest.

The results also show that the processes considered here will not cause particles much smaller than 0.5  $\mu\text{m}$  to agglomerate effectively with larger particles because of the small values of the collision efficiencies.

The two-particle-size model used here does not give a very satisfactory description of the process; extending the treatment to include a more realistic size distribution would

be straightforward in principle, but it has not yet been done. However, the sensitivities noted above show that obtaining useful results for specific accident sequences will require detailed modeling of many phenomena in addition to the turbulent coagulation process. Some of the additional treatments required include description of conditions within containment prior to its failure, jet physics, and droplet size distribution resulting from heterogeneous and homogeneous condensation occurring during blowdown expansion and subsequent mixing with ambient air.

#### 3.4.2 Differences between MARCH/NAUA and CONTAIN Release Rates

Results for radionuclides released from the containment, as calculated by CONTAIN, are being compared with the MARCH/NAUA results in BMI-2104 using equivalent assumptions concerning containment leakage rates. For the AB- $\gamma$  sequence, CONTAIN calculates release fractions for Te, I, and Cs that are 2 to 2.8 times higher than the results given in the latest revision to BMI-2104. For AB- $\delta$ , the release fractions for these fission products range from 1.8 to 2.5 times higher. This difference occurs primarily because the MARCH/NAUA calculations predict that steam will condense on aerosols released from the primary reactor coolant system (RCS) prior to vessel failure, resulting in fairly rapid deposition of these aerosols. In the CONTAIN calculations, the atmosphere is not supersaturated during this period; hence, significant condensation does not occur, and little deposition of the primary RCS aerosols takes place until generation of the core-concrete aerosols begin.

Because the rate of condensation of aerosols is a strong function of the (usually small) difference between the actual water vapor pressure and the saturation vapor pressure, relatively small uncertainties in the thermal hydraulic effects can result in rather large uncertainties in the condensation on aerosols and the resulting suspended mass of aerosols. A calculation of thermal hydraulic behavior sufficient for assessing the temperature and pressure threat to containment may be insufficient for determining the aerosol behavior.

#### 3.4.3 Attempts To Reconcile the Differences between MARCH and CONTAIN Thermal Hydraulics

In an attempt to reconcile the differences in the condensation rate, the following were investigated:

1. The CONTAIN calculations did not originally include the effects from the evaporation of sump water. Incorporation of the MARCH sump vaporization source terms did not materially affect the condensation rate on aerosols.

2. The fission-product heating of the atmosphere in the MARCH code was compared to that used in the CONTAIN calculations and was not found to be significantly different prior to vessel failure. (This agreement is fortuitous because the fission-product-release fractions to containment upon melt in MARCH are fixed.)
3. Quantities affecting heat transfer to structures were adjusted over their uncertainty range.

Thus far, attempts to reconcile the MARCH and CONTAIN thermal hydraulic differences have been unsuccessful.

#### 3.4.3.1 Sensitivity of Release Fractions to Core-Concrete Aerosols

The decontamination of aerosols released from the RCS was found to depend significantly on the generation of aerosols from the core-concrete interaction in the CONTAIN AB- $\delta$  calculation. Without coagglomeration of the RCS and core-concrete aerosols and subsequent settling, the release fractions for the fission products carried with the RCS aerosols would have been a factor of 2.5 higher than observed.

#### 3.4.3.2 Effects Attributable to the Tracking of Fission Products

MARCH assumes that the fission products released from the reactor cooling system remain suspended indefinitely in the atmosphere of a PWR. The thermal hydraulic effects of fission-product deposition are being investigated using CONTAIN. The effects of fission-product deposition, for example, may significantly affect condensation on aerosols.

Note that the degree of agreement or disagreement between CONTAIN and MARCH/NAUA cited here refers only to the differences that are apparent when input assumptions are chosen to be as closely equivalent as possible. Total uncertainties in the analysis may be substantially larger. For example, aerosol generation rates using core/concrete interactions are quite uncertain, and the CONTAIN results suggest that considerable sensitivity to this parameter may also exist.

#### 3.4.3.3 Sensitivity of Fission-Product and Aerosol Behavior to Thermal Hydraulic Behavior

Through a series of CONTAIN calculations in which the criteria for hydrogen ignition were changed slightly and the fission-product decay-heating of the containment atmosphere was added, a period of steam condensation found upon the aerosols, which is present in earlier CONTAIN calculations shortly after vessel failure, is eliminated. This change resulted in somewhat slower deposition of the aerosols.



However, in the AB-8 sequence, large aerosol deposition, due to the abundant aerosols assumed to be generated by the core-concrete interaction, still occurs; and the net effect of eliminating the steam condensation after vessel failure during this particular sequence is not large. In contrast, the effect of steam condensation prior to vessel failure may be significant and is currently the major source of discrepancy between the NAUA and CONTAIN release rates for the AB sequence.

#### 3.4.4 MARCH 2.0 Review

A review of the new debris/water interaction models incorporated in MARCH 2.0 has been initiated in support of the SARRP program. These models are intended as replacements for HOTROP in MARCH 1.1. They consist of a variety of debris bed or single-particle models that can be selected or controlled by input. This increase in complexity and flexibility may, however, be illusory since the underlying physical model still appears to be for an isolated single particle with the different model choices resulting only in different heat transfer coefficients. More realistic steam rates may result, but the physical picture is incompatible with a debris bed model, and the hydrogen generation rate is expected to be unrealistic.

#### 3.4.5 Five-Cell Description of the Surry Containment

MARCH calculations and previous CONTAIN calculations have represented all of containment as a single, well-mixed compartment. A five-cell calculation of the Surry containment is currently being set up. A multicell description of the Surry containment is of interest because of the physical separation of the blowdown compartment, the reactor cavity, and the rest of containment. Because the flowpath connection is indirect, the flow of the aerosols through the intervening compartments may significantly reduce the aerosols before they reach the main part of containment (from which they may be released to the atmosphere), and the decontamination of primary aerosols from core-concrete aerosols may be less efficient than in the case of a single, well-mixed volume.

#### 3.4.6 ANS Source Term Committee Meeting in Detroit, June 14, 1983

The role that CONTAIN might play in the ANS study was discussed with members of the ANS Source Term Committee. The ANS Committee has selected a 15-cell representation of containment for modeling the thermal hydraulic behavior, using the THREED code. The aerosol behavior is to be modeled using the RETAIN, NAUA, and HAA-4 codes. Only RETAIN, an extension of TRAP-DELTA with HAARM aerosol modeling in this group of codes, is appropriate for general multicell modeling. However, RETAIN uses lognormal size distributions, does not model condensation on aerosols, and has no provision for

multiple aerosol components. CONTAIN does not have these limitations and has multicell capabilities. It would be highly suited for the ANS source term study if the thermal hydraulic conditions from the THREED code could be specified on input.

#### 3.4.7 Containment Loads Working Group

A panel of specialists from various laboratories around the country has been established by NRC's Containment Systems Research Branch to apply current phenomenological understanding to the problem of estimating the range of pressures that can occur in an LWR severe accident. The project is in support of the reassessment of source term estimates, and the goal is to provide useful input to the ASTPO by November 1983 by drawing on resources from a variety of NRC activities. The focus of the work is on the steam spike and the adequacy of models being used in the source term studies. The work will take place via two questionnaires and two Working Group meetings in the Washington area. The first questionnaire has been completed and responses returned to NRC. The first Working Group meeting is scheduled for the middle of July.

### 3.5 REFERENCES

- 3-1. R. Acton and E. Randich, Intermediate-Scale Tests of Sodium Interactions with Calcite and Dolomite Aggregate Concretes, SAND83-1064 (Albuquerque, NM: Sandia National Laboratories, 1983).
- 3-2. Vaughan, "Simple Model Plugging of Ducts by Aerosol Deposits," Transactions of the ANS, 28, p. 507 (1950).
- 3-3. Clinch River Breeder Reactor Plant Radioactive Source Terms, WARD-D-0193 (Madison, PA: Westinghouse Electric Corp., May 1982).
- 3-4. Knelman, "The Mechanism of Drop Formation from Gas or Vapor Bubbles," Transactions of AIChE, 32, p. 249 (1945).
- 3-5. N. A. Fuchs, The Mechanics of Aerosols (New York: Pergamon Press, 1964), pp. 32-34.

#### 4. ELEVATED TEMPERATURE MATERIALS ASSESSMENT

(C. H. Karnes, 1835; W. B. Jones, 1835)

The primary objectives of the Elevated Temperature Materials Assessment studies are to (1) determine how microstructures evolve due to thermomechanical history that results in mechanical property changes, (2) evaluate the validity of material damage rules used in design, and (3) develop and evaluate nondestructive evaluation techniques.

The computer control program developed for the cooperative study with ORNL on the behavior of stainless steels under nonproportional biaxial stress states was completed and verified for elastic deformation. The program controlled tests in which multiple linear paths in stress space were traced out by varying both axial load and internal pressure. Previous studies on this program have shown the relationships between crack growth rates under fully plastic cyclic conditions and strain range and temperature in "as-received" 316 SS. It is known that thermomechanical histories can result in significant microstructural changes such as precipitate formation either along the grain boundaries or uniformly distributed throughout the grains. A set of experiments was initiated to determine if these microstructural effects can result in changes in the crack growth characteristics. Crack growth specimens were placed in evacuated glass tubes to be aged at 922 K (649°C) for 2 mo. Others were deformed at a strain range of 0.5% for 300 cycles. These also will be thermally aged for 2 mo. Both sets of specimens will then be subjected to crack-growth-rate experiments under fully plastic loading.

A member of Sandia's staff visited six European research laboratories to exchange information on elevated temperature deformation behavior studies. These conversations revealed the following: Very-short-time creep behavior of 316 SS up to temperatures of 1473 K (1200°C) is being investigated for fast breeder reactor accident analysis. A heat-pipe furnace design is available that produces extremely accurate temperature uniformity and control. Shorter creep-rupture lifetimes are observed in tests on electronically controlled test machines compared to dead weight machines. Test frame vibrations are the suspected cause. Observations have been made of significant effects of low neutron fluences accompanied by creep and creep-fatigue deformation. Questions as to why the U.S. investigators have not been interested in radiation effects on out-of-core structural components were raised. The Europeans think the effects are important. A tremendous level of effort is underway on studies on deformation behavior, microstructural evolution, and fatigue with additional effort committed for future work on creep-fatigue, fracture mechanics at elevated temperatures, constitutive modeling, and damage accumulation. Strong emphasis has been placed on going to longer test times to confirm extrapolations to qualify nuclear materials under

multiaxial loading and creep-fatigue conditions. The feeling is that current damage accumulation models for elevated temperature design are not adequate and may not even be conservative. Results indicate that long hold times in sodium may be worse than in air for some alloys, but the cause is unknown. The investigators at the Joint Research Center--Petten would like to collaborate on the crack growth studies under fully plastic cyclic loading. They have observed anomalies at short crack lengths similar to Sandia's. The British have seen a significant change in failure mechanisms for cycling over slow strain rates ( $10^{-10}$ /s to  $10^{-5}$ /s) compared to strain rates greater than  $10^{-5}$ /s. The slow strain rates are more representative of operating conditions.

## 5. ADVANCED REACTOR ACCIDENT ENERGETICS

The Advanced Reactor Accident Energetics program addresses the key issues in a core-disruptive accident that determine the progression and severity of the accident for current LMFBR designs. This program involves a series of in-pile experiments and analyses that focus on key phenomena in two general areas:

- a. Initiation Phase - Fuel/Clad Dispersal Experiments
- b. Transition Phase - Fuel Freezing and Streaming Experiments

### 5.1 INITIATION PHASE

(S. A. Wright, 6423)

The motion of clad and fuel in the initiation phase of an LOF accident are important considerations in the subsequent progression of the accident. Early fuel dispersal can lead to neutronic termination while limited dispersal and blockage formation continues the accident into the transition phase and the possibility of further neutronic activity. To obtain data on the important phenomena involved in this phase of an LMFBR accident, the USNRC is sponsoring the Sandia Transient Axial Relocation (STAR) experiments in the ACRR test facility.

The STAR experiment program is the follow-on series to the Fuel Disruption (FD) experiments. This in-pile program is intended to extend the technology gained in the FD series to the fundamental issues of the axial relocation of fuel and cladding.[5-1],[5-2] The STAR tests will subject single and multipin bundles of irradiated mixed oxide fuel to reactor power transients. These transients will reproduce the heating conditions of LOF accidents in LMFBR. A high-speed camera system will be used to observe the fuel and clad relocation. In addition to this experimental work, a major portion of this program will develop or modify existing phenomenological models for fuel and clad relocation as well as verify similar models used in accident analysis codes, such as SAS.

The funding for this program will be cosponsored by the USNRC and by the German Nuclear Research Center, KfK. Currently, negotiations are underway to define the extent of the exchange program and to determine specific areas in which each research center can contribute to the program.

#### 5.1.1 Test Plans

Six experiments are tentatively planned for the first phase of this program. The details of the fuel heating conditions have not been specified, but a variety of heating conditions to cover the range of uncertainties for LOF accidents in LMFBRs will be investigated. The first two experiments are

scoping experiments that will use fresh  $UO_2$  fuel, and one of these first experiments will use a multipin bundle. The following four experiments will probably be performed with irradiated mixed oxide (MOX) fuel. These experiments will probably use heating conditions similar to the CRBR and SNR-300 LOF accident scenarios.

During this report period, the experimental design for the program was completed and most of the hardware was ordered. This report describes the design of the STAR capsule and the scoping calculations used to estimate the necessary thermodynamic and neutronic data required to perform such an experiment.

### 5.1.2 Experiment Design and Description

The goal of the STAR program is to investigate the axial relocation of fuel and cladding during LMFBR LOF accidents. To accomplish this task, the experiment hardware was designed to reproduce accurately the relocation processes but allow for direct viewing and filming of these processes. A schematic drawing of the STAR capsule and hardware is shown in Figure 5.1-1.

The experiment hardware forces an inert gas (Ar) past a multipin bundle that has been electrically preheated to 1200 to 1300 K (927° to 1027°C). The density (pressure) of the fill gas will be adjusted to the density of saturated sodium vapor and will be forced through the pin bundle at velocities up to 100 m/s. The flowing gas will cause the molten clad and fuel to move upward (or downward) as though driven by the competing forces of streaming sodium vapor, drag, and gravity. Since the drag on the particles of fuel and cladding is accurately reproduced, the flow characteristics of the molten fuel and clad particles will be typical of those in LOF accidents.

Prior to the reactor power transient, the pin bundle will be electrically preheated to the sodium boiling temperature. This will insure that the freezing and plugging processes of molten fuel and cladding over the nonneutronically heated sections are accurately reproduced.

Experience from the FD experiments showed that disrupting irradiated fuel moves primarily in the radial direction. This is an anomaly of the FD experiments because the disrupting fuel is not surrounded by neighboring pins. To overcome this radial motion, many of the STAR experiments will use multipin bundles.

In most cases, several fresh fuel pins will surround one or more irradiated pins to limit the radial motion. Multipin bundles of up to eight pins will be used. A maximum of four

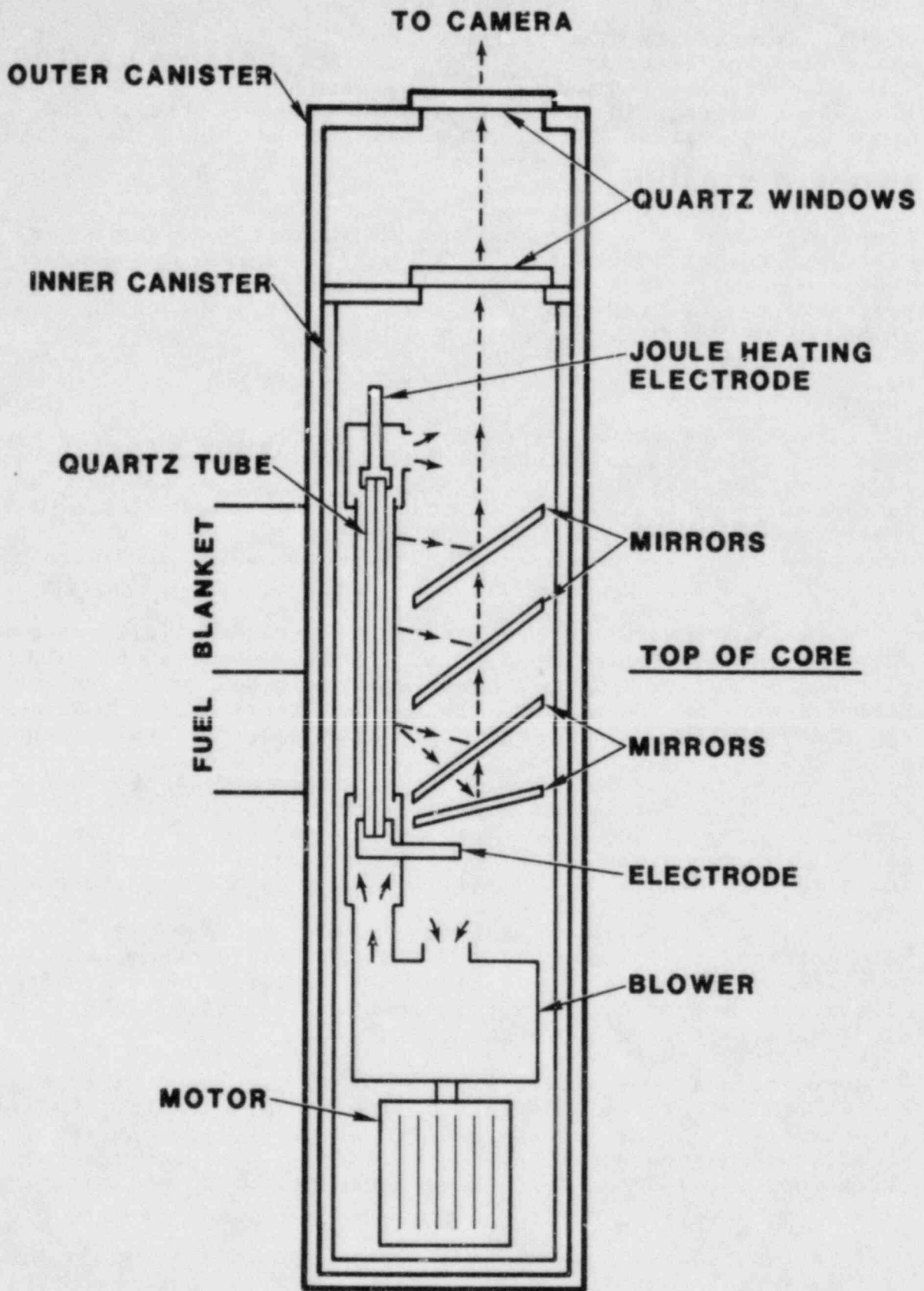


Figure 5.1-1. Schematic of STAR Capsule and Hardware



irradiated pins will be used in any one experiment. In addition, the fuel bundle will be surrounded by a quartz tube to help contain the radial motion as well as direct the gas coolant flow.

The fuel pins have a total length of 0.66 m. The center 0.42 m of the fuel pins simulates the upper structure of an LMFBR fuel pin. It therefore has an enriched fuel zone 0.16 m long and an upper blanket zone 0.26 m long. The enriched fuel zone consists of 40% to 67% enriched  $UO_2$  or MOX fuel. The blanket zone will use fully depleted  $UC_2$  instead of natural uranium as in an LMFBR. The very bottom of the enriched fuel zone will be placed at the axial centerline of the ACRR. Thus a strong axial thermal gradient will exist on the fuel pin (up to 400 K (127°C) over the length of the enriched  $UO_2$ ). Each fuel pin will contain approximately 34.1 g of enriched fuel. For an eight-pin bundle (the largest that will be used in any experiment), the total enriched fuel mass will be 242 g.

The STAR capsule and hardware uses the same concept of double containment with quartz windows and mirrors that was used in the FD experiments. However, the entire capsule has been redesigned and is now approximately 2.44 m tall and 0.2286 m in diameter. The canisters are made of 304 SS steel and are 2.286 mm thick. The inner container houses a motor and blower, the fuel pin, and associated instrumentation, including TCs, flow meters, and pressure transducers. Since the optic system must view a 0.42-m-long section of the fuel pin, a 35-mm high-speed camera system will be used to record the the axial fuel and clad relocation.

The inner capsule also houses a series of mirrors that comprise part of the optic system. The mirrors are mounted on an optical slide that reflects a "multiplexed" image of the fuel pin through a quartz window located in the upper lid. Figure 5.1-2 shows the fuel pin image as seen by the cameras. Two types of mirrors are used to produce this image of the fuel pin. The first type looks directly at a 10-cm section of the fuel pin (or possibly at a slight angle, to view about 12.7 cm of the pin). Three mirrors of this type are used to view from 31 to 41 cm of the fuel pin. The other type mirror is located below the fuel pin and views its entire length at a severe angle (approximately 15°). Because an individual mirror as viewed from the quartz window is 10 cm long and the quartz window is only 8.25 cm in diameter, a relay lens is used to fully view the fuel pin as reflected by the mirrors. This lens is mounted on the upper structure assembly, 1 m above the capsule.

### 5.1.3 Instrumentation

The high-speed camera and the reactor power monitors are the major diagnostic tools for the STAR experiments. Other types of instrumentation are also provided, including fuel and

**QUARTZ TUBE &  
PIN BUNDLE**

**MIRRORS**

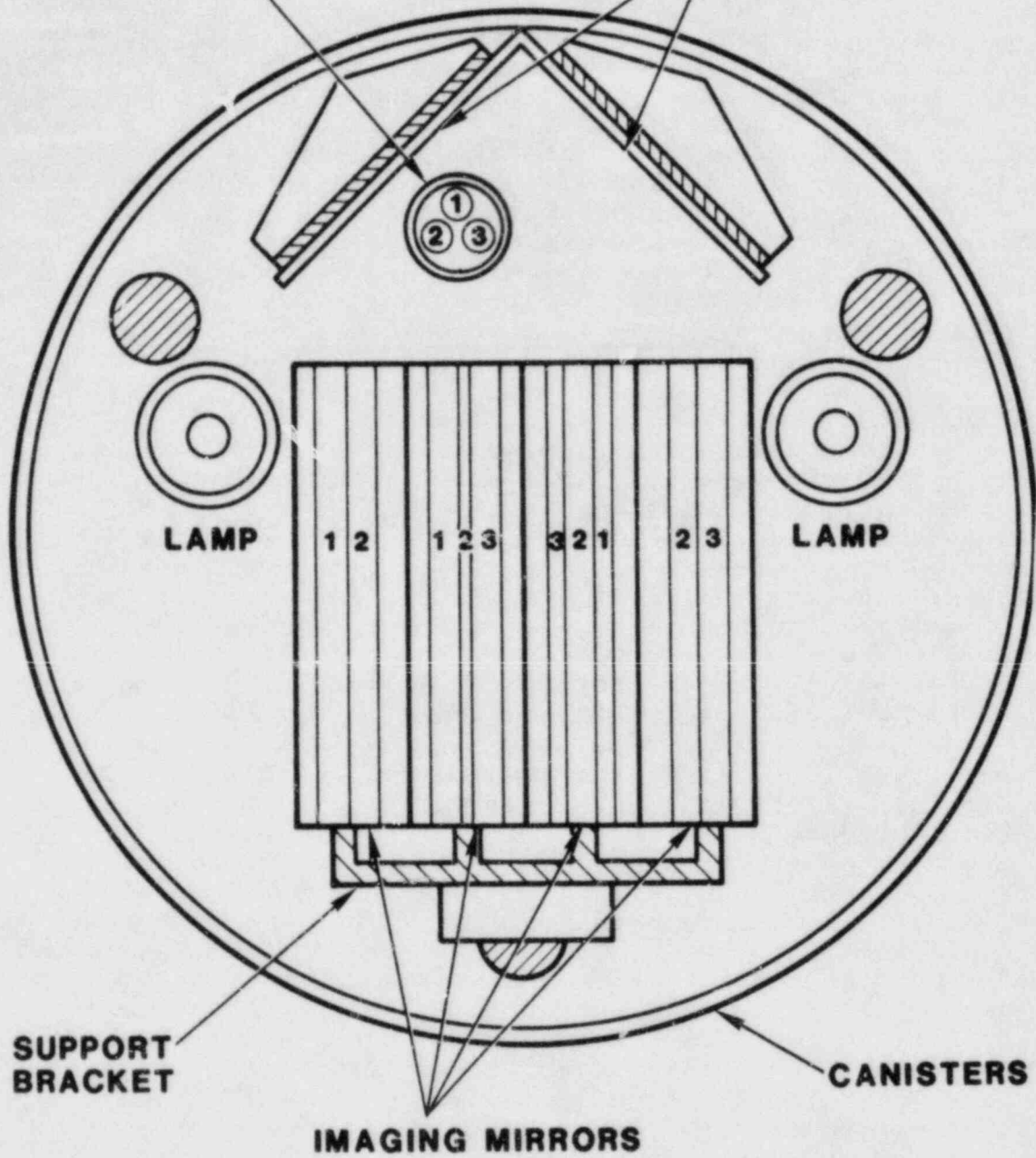


Figure 5.1-2. Image of Fuel Pin as Seen from Camera

clad surface temperature measurements; gas temperature, pressure, and flow rate measurements; and some structural temperature measurements. Table 5-1 lists the various diagnostic devices and gives some important characteristics of each device.

#### 5.1.4 Reactor Power Transients and Coupling Factors

To simulate the LOF heating conditions in the STAR experiments, both the programmed rod withdrawal mode and the multiple-pulse mode of the ACRR will be used. The multiple pulse mode will be used mainly with the first fresh  $UO_2$  experiments. The HRR experiments used reactor power pulses of this type.[5-3] The programmed rod withdrawal mode will be used for the irradiated fuel experiments. This type power transient was used in the FD2/4 series of experiments.[5-4],[5-5]

These types of power transients were chosen for several reasons. Both modes of reactivity insertion (TRW and pulse) provide a preheat section that lasts from 2 to 9 s. During this neutronic preheat, the fuel is raised to near-steady-state operating temperatures. The preheat allows enough time for the radial temperature profiles to relax and thus establish near-prototypic profiles. In addition, the time of the second pulse can be selected to disrupt the fuel either before, during, or after clad melting. The magnitude of the pulse can also be varied to select the heating rate at the time of disruption. In the TRW mode, the heating rates will be on the order of 1000 to 4000 K/s, while in the multipulse mode the heating rates will be on the order 50,000 to 100,000 K/s. The slower heating rates represent the heating conditions for LMFBR LOF accidents while the higher rates are more representative of LOF-driven transient-overpower (TOP) accidents.

Depending on the goals of the individual experiment, the STAR power transients will clearly vary from these proposed transients. As a consequence, several test transients will be requested prior to the experiment to determine the actual rod insertion times and rates.

#### 5.1.5 Reactor Coupling Factor and Shape Functions

The reactor coupling factor is defined as the ratio of the average energy (per unit mass of fuel) in the test pin to the total energy in the reactor core. Its units are J/g (in the test pin) per MJ in the reactor. An accurate knowledge of this ratio is needed to determine the desired reactor pulse and to perform posttest analysis. In addition, the axial and radial shapes of the energy deposition are needed.

Estimates of the coupling factors were determined from the FD calorimeter experiments and from TWOTRAN neutron transport calculations. The coupling factors measured for the FD

Table 5-I

## Instrumentation for the STAR Experiments

<u>Detector</u>	<u>Location</u>	<u>Measurement Range</u>	<u>Time Response</u>
High-speed 35-mm camera "Photosonics"	Reactor room	500 to 2000 frames/s	---
Cadmium self-powered neutron detector	Reactor core	0 to 40,000 MW (reactor power)	1 $\mu$ s
Fission chamber (XC-FC-19)	NW of core	0 to 40,000 MW (reactor power)	1 $\mu$ s
Optical pyrometer "Pritchard"	Reactor floor	2000 to 3500 K (1727° to 3227°C) fuel surface temperature	1 ms
Pressure transducers "Statham-Gould" PL131TC-5	Inner canister		1 ms
PA208TC-50	Through quartz tube Inlet to flow channel	0 to 5 psia 0 to 50 psia	
Gas TCs (3) K-type exposed wire "Medtherm"	Inner canister Inlet flow Exit flow Canister gas	300 to 1700 K (27° to 1427°C)	20 ms
Clad TCs (2-3) K-type thin film "Medtherm"	Inner canister Bottom of pin Middle of pin Top of pin	300 to 1700 K (27° to 1427°C)	20 ms
TC K-type (1)	Inner bulkhead	300 to 1700 K (270 to 1427°C)	200 ms
Flow meter FT-24 "Flowtechnology"	Exit of flow channel	8 to 150 ACFM	10 ms

are assumed to be identical to the STAR single-pin coupling factors at the axial center line of the ACRR. Thus, the FD results were used to normalize the TWOTRAN calculations and were then used to estimate coupling factors for other enrichments and for multipin bundles.

Table 5-II lists the coupling factors at the core axial centerline for one-, three-, four-, six-, seven-, and eight-pin experiments. For the four-, six-, seven-, and eight-pin experiments, more than one coupling factor is given because the energy deposition in the pins depends on the degree of self-shielding by neighboring pins. These coupling factors are grouped according to geometric similarities. Figure 5.1-3 shows a cross section of the multipin bundle configurations that are under consideration. The numbered pins represent pins for which coupling factors are given. The coupling factors are given in sequential order, beginning with pin 1 at the top of the list.

Table 5-II gives the coupling factors for 40% and 67% enriched fuel. As the size of the bundle increases, the coupling factor decreases. The eight-pin bundle has an average coupling factor (10.27), which is 30% less than the single pin coupling factor (14.63), while the four-pin bundle has a coupling factor (12.32) that is only 16% less. In some experiments, the 40% enriched fuel pins may be placed around 67% enriched fuel to insure that all fuel pins fail simultaneously or that the inner pins fail first.

The single-pin axial energy deposition profiles for 40% and 67% enriched fuel are given in Figure 5.1-4. The TWOTRAN calculations indicate that the shape of this profile is independent of the pin bundle size and enrichment. Thus, only one profile is needed to describe the axial shape of the energy deposition. Because of the cosine-shaped neutron flux, the energy deposition at the top of the pin is about 26% less than at the bottom (core centerline).

The single-pin radial energy deposition profiles for 40% and 67% enriched  $UO_2$  are given in Figure 5.1-5. These radial shapes are nearly identical to the FD radial energy deposition profiles (note that they are dependent on the enrichment). Because of the large variety of bundle geometries and their complexity, the coupling factor calculations described above will have uncertainties on the order of 25%.

Table 5-II

Coupling Factors for 40% and 67% Enriched UO<sub>2</sub>

Enrichment (%)	Number of Pins					
	<u>1</u>	<u>3</u>	<u>4</u>	<u>6</u>	<u>7</u>	<u>8</u>
	Coupling Factor (J/g)/MJ					
40	10.85	9.34	8.54	8.75	6.21	6.64
			9.50	7.39	7.80	8.38
				7.51		7.25
				8.77		
		<u>14.63</u>	<u>12.53</u>	11.27	11.83	8.06
67			<u>12.67</u>	9.82	<u>10.34</u>	<u>11.32</u>
				10.03		9.63
				<u>11.88</u>		

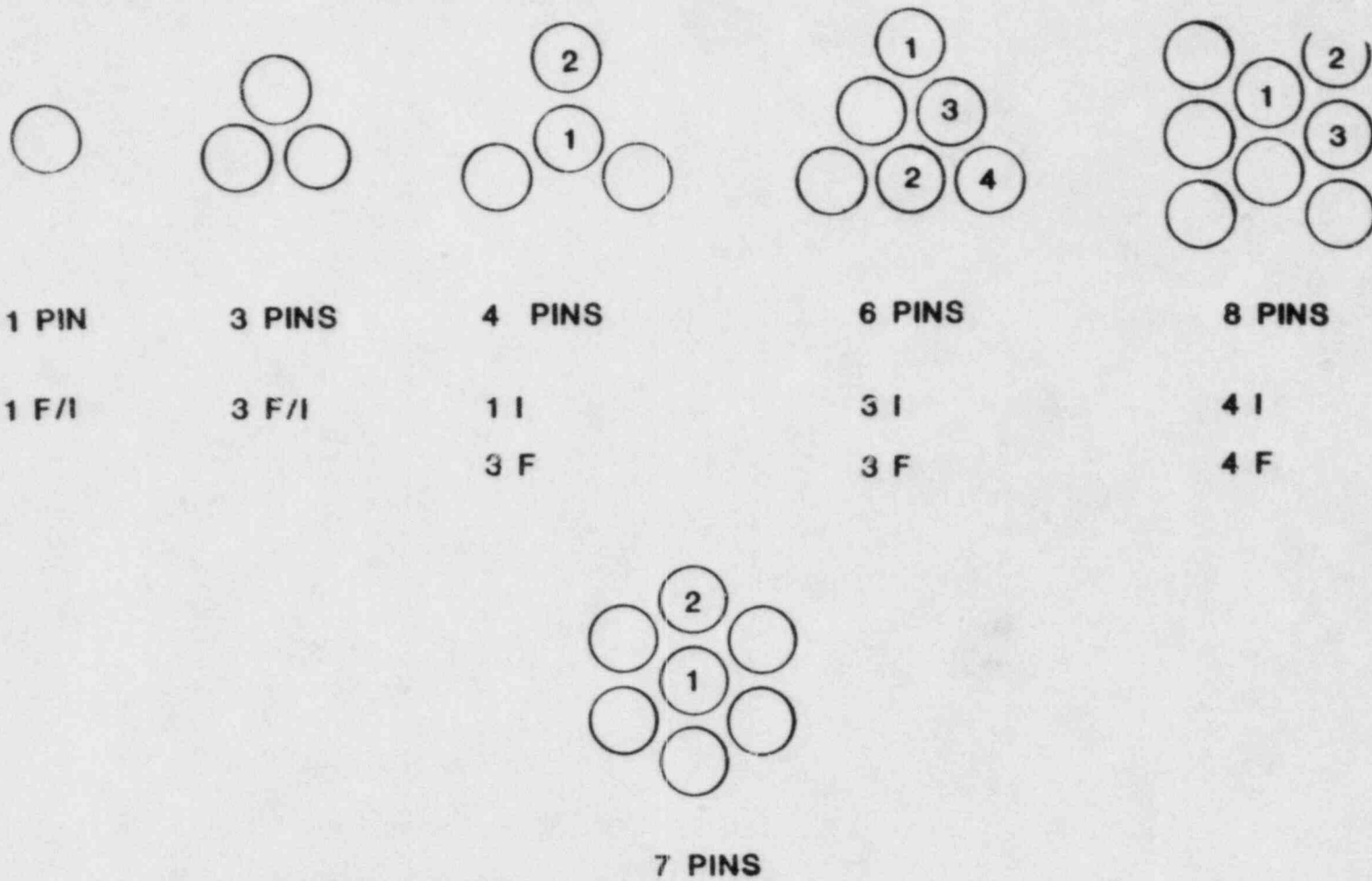


Figure 5.1-3. Multipin Geometries

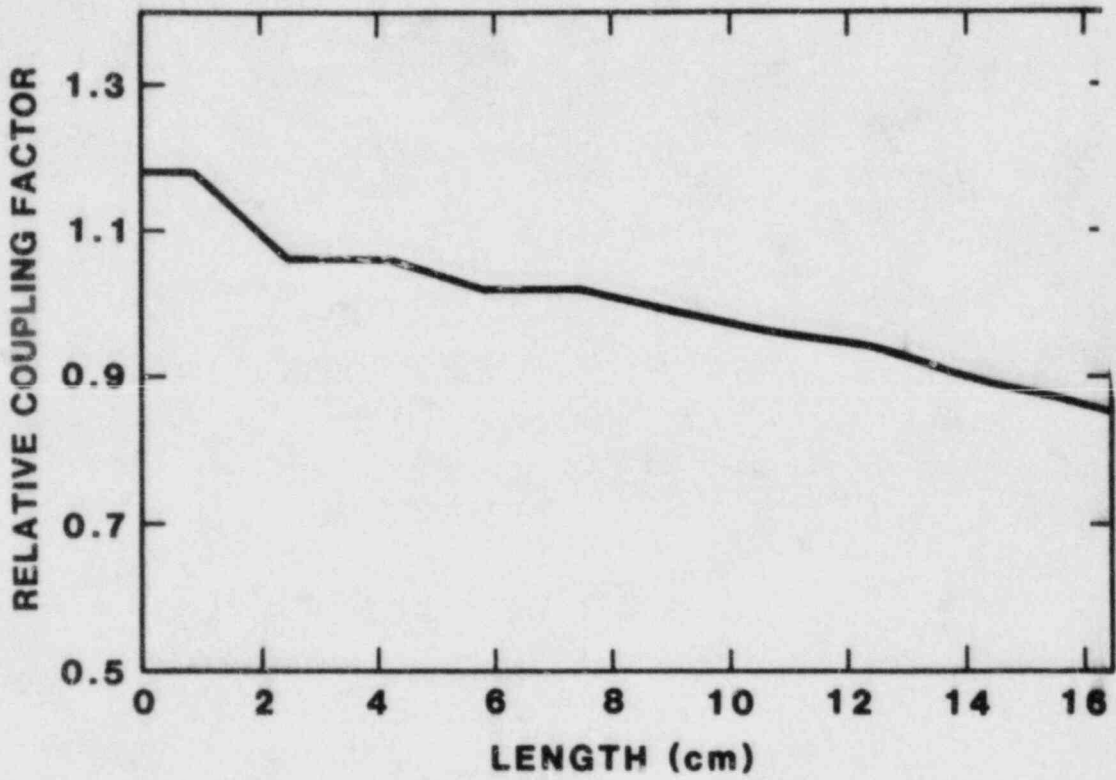


Figure 5.1-4. Axial Energy Deposition Profile



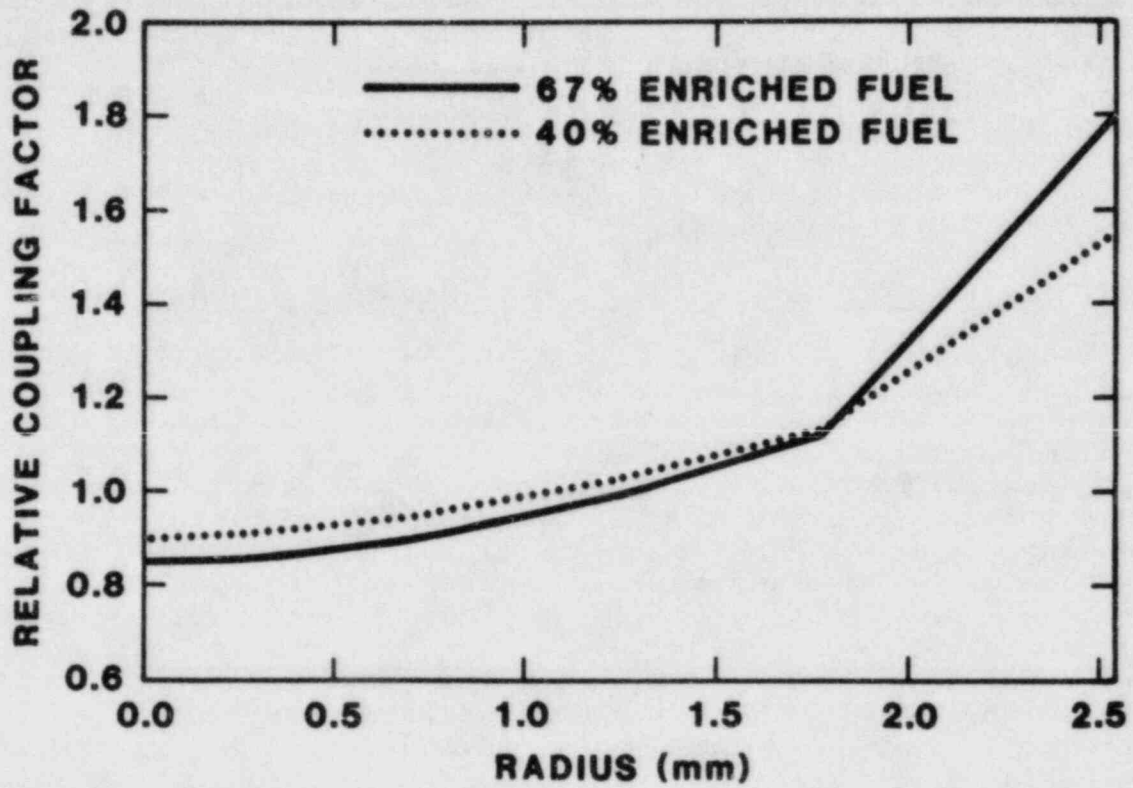


Figure 5.1-5. Radial Energy Deposition Profiles

## 5.2 TRANSITION PHASE

(D. A. McArthur, 6423, R. O. Gauntt, 6423; P. K. Mast, 6425)

Many current LMFBR core designs are characterized by a relatively low-Na void coefficient and incoherent behavior in the initiation phase. These features generally increase the likelihood of a "transition" or "meltout" phase during a core-disruptive accident. The key questions in the transition phase are whether fuel or clad blockages form, leading to a confined or "bottled" core configuration, and the behavior and reactivity implications of this pool of fuel-steel in the core region if the fuel blockages do lead to this state. The TRAN program addresses the question of fuel-inventory reduction by penetration into upper core structure or through subassembly (S/A) gaps to the lower core structure. If deep penetrations occur, nonenergetic shutdown is probable, while shallow penetration will lead to a transition phase and the possibility of further energetics. First-of-a-kind in-pile experiments are being conducted to provide data to evaluate the various models describing fuel penetration.

### 5.2.1 Posttest Examination of TRAN Series I (TRAN-2 Test)

Analysis of TRAN-2 continues to be of special interest because it exemplifies the onset of steel melting yet does not exhibit the extremely complex behavior seen in TRAN-4. Longitudinal sections were previously made through the two blockages observed in experiment TRAN-2. Detailed examination of these blockages revealed a lower average density for the leading blockage. Each blockage contained globules of steel surrounded by  $UO_2$ , and some of these steel globules contained spherical void regions (Figure 5.2-1). Globules of steel were also observed in the upper end of the crust layer (although the crust layer ends about 8 cm below the final position of the two blockages, the two blockages were presumed to be originally formed at the end of the crust layer). The outer surfaces of the leading blockage were more rounded than the surfaces of the trailing blockage, perhaps implying that the trailing blockage had been constrained during freezing by the leading blockage and by contact with the channel wall.

The more porous and rounded structure of the leading blockage suggests the possibility that steel boiling could have occurred into the low-pressure region of the leading edge of the advancing fuel slug. Because of the large heat of vaporization of steel, such boiling could represent a large heat loss mechanism for the fuel at the leading edge of the flow and could be a very important mechanism for blockage formation.

Since steel boiling may have played an important role in the blockage formation, the source of the molten steel found in the fuel crust becomes of interest. The steel may have

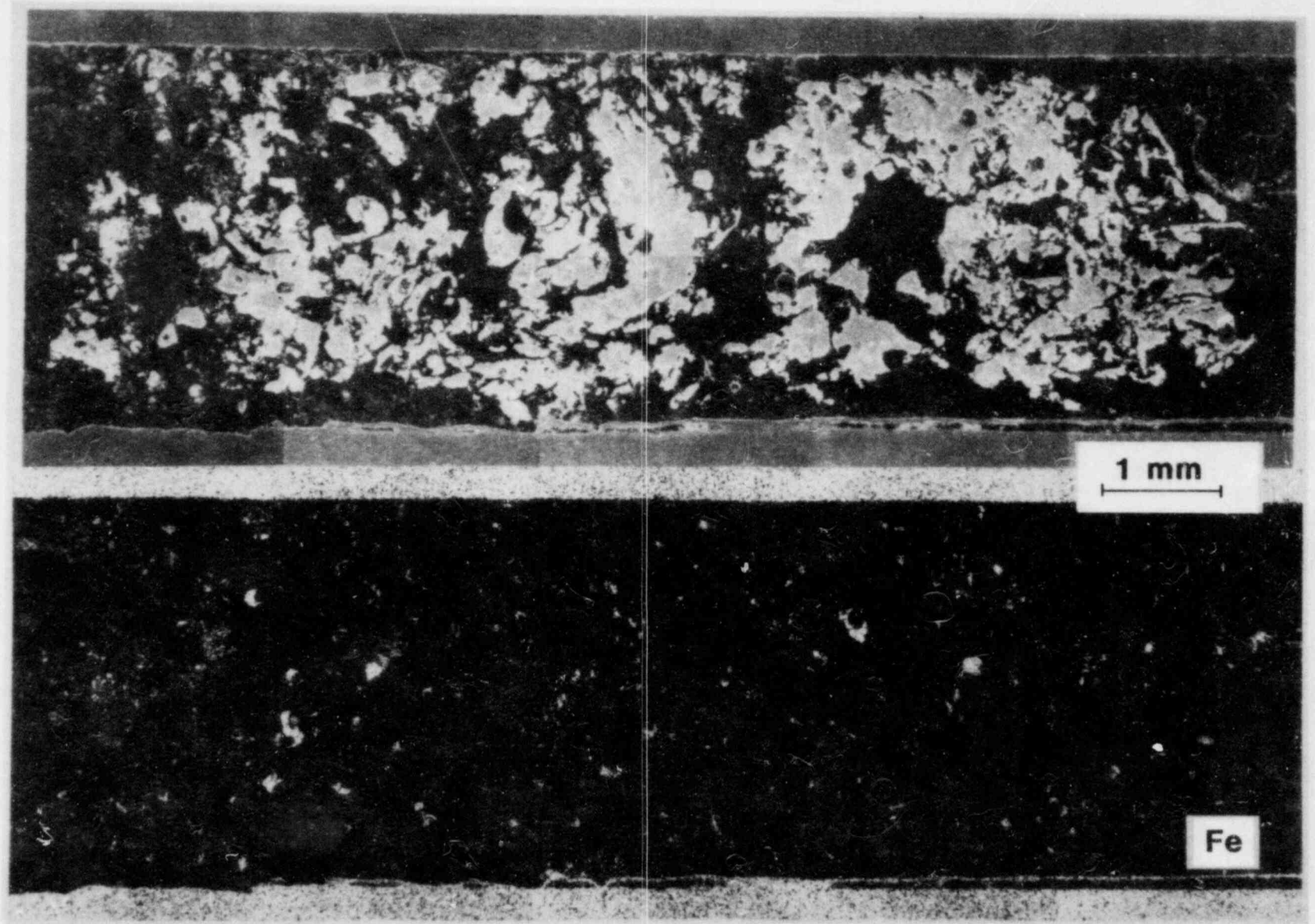


Figure 5.2-1. Blockages Observed in TRAN-2

been ablated from the fuel melting chamber wall or from the freezing channel wall near the channel entrance where the melt flow is changing direction. Therefore, additional transverse and longitudinal sections were made near the channel entrance to determine the axial extent of steel ablation from the channel wall. Areas of refrozen steel were indeed found under the fuel crust near the channel entrance (Figure 5.2-2). However, without an accurate distance scale on the photos, it is difficult to say conclusively whether these areas represent steel in the process of being ablated, or molten steel being deposited over an as-machined steel surface.

The transverse sections near the channel entrance show a very smooth line of demarcation between the melted steel and the as-fabricated steel. However, the boundary between the fuel crust and the melted steel is irregular on a small spatial scale.

Substantial erosion of the molten steel layer is not evident except over the 0.3 cm near the channel entrance. Hydrodynamic effects associated with the transition from melting chamber to freezing channel may have been responsible for the steel entrainment.

Field distortions are present in scanning-electron micrographs, and instrument limitations also prevent the making of a single electron micrograph of the entire channel. Therefore, the best method for obtaining an accurate absolute distance scale appears to be placing an accurate optical graticule in contact with the polished sample and making an optical micrograph. The results of this procedure should be available during the next quarter.

## 5.2.2 Results of TRAN B-Series (B-1 Test)

### 5.2.2.1 Final Fuel Distribution

Detailed scans of the  $^{103}\text{Ru}$  gamma-ray line were completed for both the zero and 90-degree orientations of the B-1 apparatus. Data for the zero-degree orientation are shown in Figure 5.2-3. The correction for absorption in the steel of the fuel housing is somewhat simpler for this orientation. The agreement between the gamma scans and the initial radiographs is excellent. The relative fuel distribution shown in Figure 5.2-3 indicates that compared to TRAN Series I experiments, an unusually large fraction of the fuel froze above the entrance to the freezing channel (about 60% of the initial fuel load, or about 60 g). This tendency toward greater upward fuel movement may be the result of the larger flow area of the annular channel compared to the 3.2-mm-diameter cylindrical channel used in TRAN Series I. Based on the fuel mass distribution implied by Figure 5.2-3, a total crust thickness of about 0.5 mm should be observed in transverse cuts made through the lower 40 cm of freezing channel. A very large

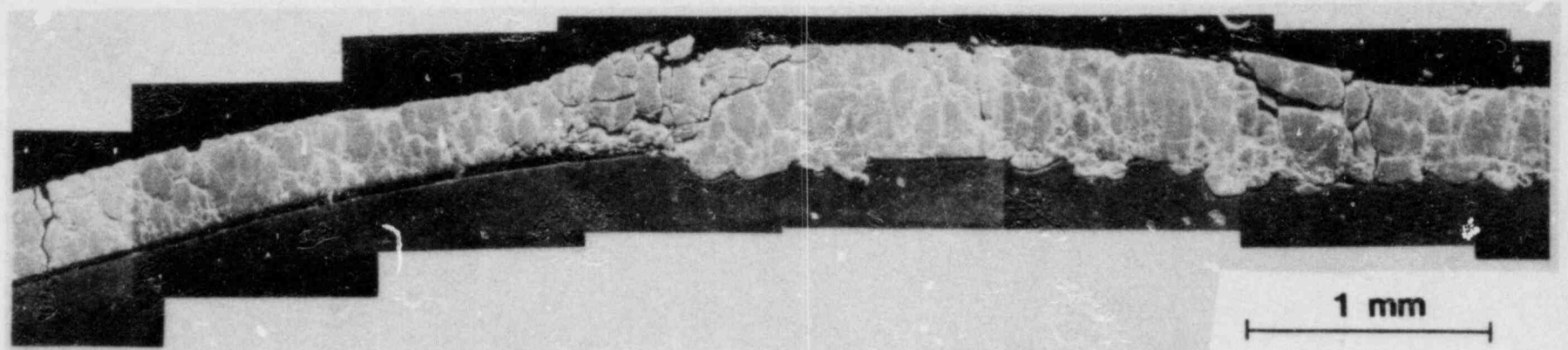


Figure 5.2-2. Fuel Crust near the Channel Entrance  
of TRAN-2

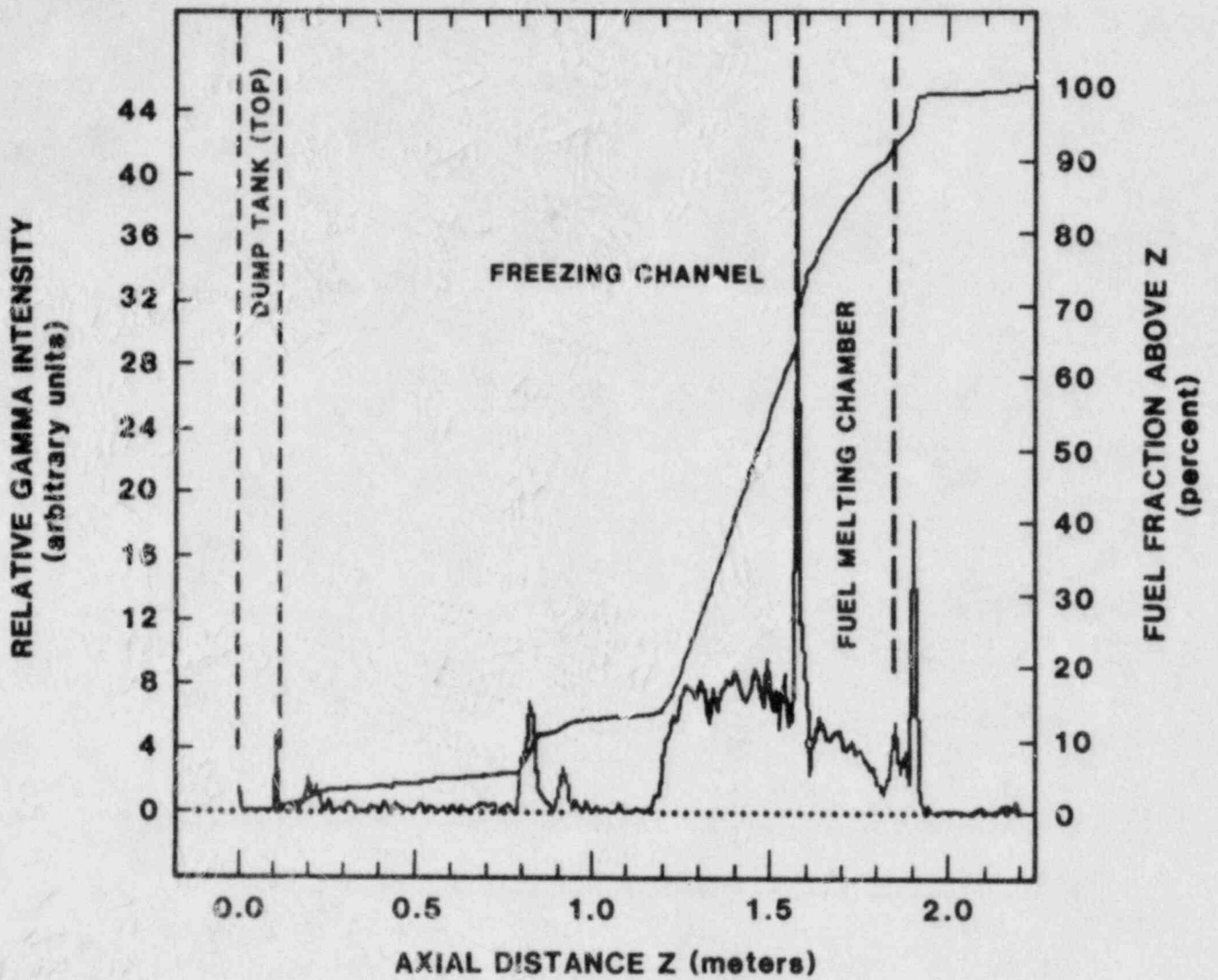


Figure 5.2-3. Relative Fuel Distribution Data for 0° for TRAN B-1

peak of emission was seen at the entrance to the freezing channel, where an axial gap apparently developed between the freezing channel insert and the inner face of the fuel housing. Isolated peaks of gamma emission correlate very well with accumulations of loose debris seen above the main fuel crust.

#### 5.2.2.2 Posttest Examination of B-1 in Hot Cell Facility

When the annular channel insert was removed from B-1, a fine, dust-like powder of fuel was seen inside the dump tank at the exit of the freezing channel and over the outside of the upper end of the channel insert. This suggests either deposition of fuel from the vapor state, or generation and deposition of fine solid fuel powder by the He gas flow.

Following removal of the channel insert, the channel entrance was attached to a vacuum line, and epoxy was drawn from the channel exit toward the entrance to immobilize the debris for transverse sectioning. Following this process, another radiograph of the channel was made (Figure 5.2-4). Comparison with the radiograph of B-1 made just after the experiment was performed showed that much of the finer debris had been swept back toward the channel entrance by the epoxy flow. The fuel distribution in the lower part of the channel did not seem to be affected by the epoxy, however.

Because much less steel surrounded the channel in this second radiograph, the contrast and resolution were much better. In the new radiograph, a thin continuous crust was observed only over the first 20 cm of the outside wall of the channel. The crust on the remainder of the outer wall (next 20 cm) appeared to be nonuniform and even discontinuous. A well-defined crust was not apparent anywhere on the inner rod. In several locations, two thin overlying layers of crust were observed, and transverse sections were made at these locations to see whether the two crust layers might originate from different walls. The crust appears to be azimuthally and axially less uniform about 10 cm into the channel, and these regions were also studied for comparison with the lower, more uniform crust.

Transverse cross sections were made through the B-1 freezing channel at several axial locations. Consistent with the earlier radiographs, these sections show an azimuthally uniform, partially disrupted crust very near the outer channel wall. Unlike the crusts seen in the earlier TRAN Series I experiments, however, this crust does not adhere to the steel wall and is in fact partially disrupted (sections missing). Also consistent with the radiographs, in no case was there found a fuel crust still present on the inner rod. However, the channel did contain several azimuthally extensive (up to 40% of channel circumference) sections of crust that appear to have originally frozen on the inner rod and were subsequently displaced (by rod bowing, perhaps) into the channel.

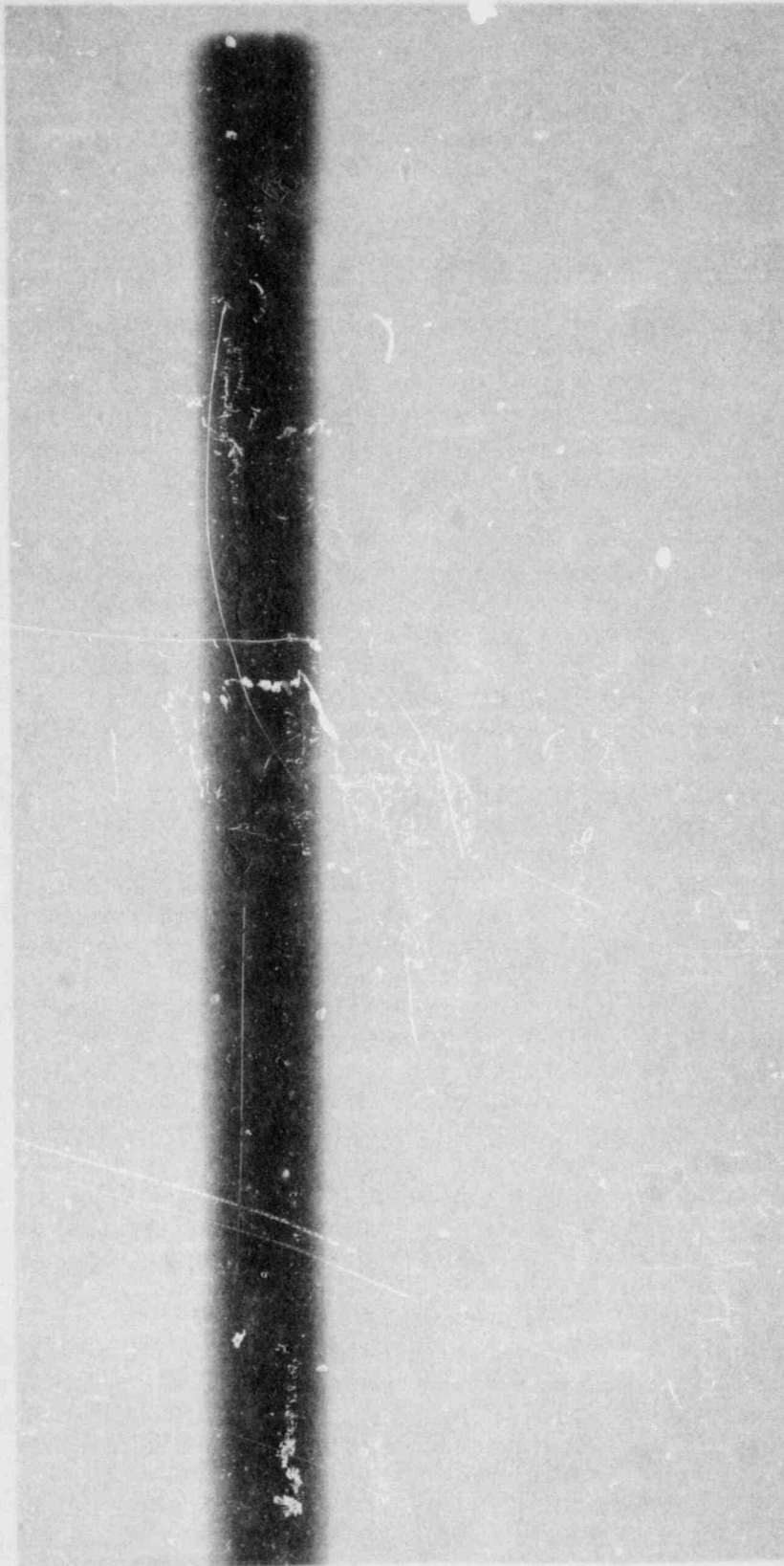


Figure 5.2-4. Radiograph of the Channel for TRAN B-1



The generally uniform thickness of all the crusts suggests that during the entire fuel flow process the crust was in contact with the inner rod and in fact froze there. The subsequent disruption of the crusts, resulting in the final fuel configuration seen, appears to have occurred late in time when even most of the residual liquid film (deposited at the trailing edge of the liquid fuel slug) was solidified. In general, the crusts on the outer channel wall appear to be somewhat (up to 20%) thicker than the crust that is hypothesized to have originally come from the inner rod surface. On the average, the measured crust thickness exceeds that predicted by PLUGM by about 15%. This discrepancy is largely due to uncertainties in liquid film deposition.

### 5.2.3 Experiment Preparation of TRAN B-Series (B-2 Test)

#### 5.2.3.1 Preparation for TRAN B-2 (First Fuel/Steel Experiment)

Los Alamos National Laboratory has found that it is very difficult to sinter mixtures of  $UO_2$  and steel and, in fact, has been able to make only pellets that are either very fuel-rich or steel-rich. This has meant that the preferred composition of about 25 vol% steel/75 vol% fuel cannot be made by the usual extrusion method. Early in June, Sandia personnel decided that large hot-pressed slabs must be made and the two-enrichment-zone pellets machined from these slabs. Preliminary pressings were made in June. This method should produce 25% steel/75% fuel pellets of the desired average density and strength, but more material will be required, since more is wasted during fabrication.

Pellets of 5% steel/95% fuel were produced by Los Alamos National Laboratory, but they differ significantly from the requirements originally specified. An average density of only 63% of theoretical density was achieved, in comparison to the desired 80% of theoretical density. As a result, the total melt mass will be significantly lower than in other B-Series experiments; also, the pellets are quite weak, so it was not possible to drill a TC hole through the center to facilitate measurement of the energy deposition coupling factor. Finally, much less fuel was fabricated than had originally been ordered, and this will limit the number of experiments that can be performed with this fuel/steel composition.

The 5% steel/95% fuel pellets were assayed for enrichment, and the fuel housing for B-2 was assembled, incorporating the new Loctite-sealed TCs in the freezing channel. About 5 atm of He backpressure will be used in B-2 to suppress boiling of the steel at those locations in the fuel/steel pellets where the energy deposition peaks. Eliminating any transient rise in the backfill gas pressure, such as was observed in the Series I experiment TRAN-5, will be necessary.

A stainless-steel-wool debris catcher was placed at the entrance to the dump tank to prevent fine fuel debris from spraying throughout the dump tank and producing a pressure pulse by heating the backfill gas. The effect of the debris catcher on the He gas flow was measured to be negligible compared to the flow resistance of the 3.2-mm-diameter freezing channel.

#### 5.2.3.2 "Tagging" of Initial Melt Load

In modeling of the fuel flow and freezing process, necessary information includes whether the plugs observed in TRAN-2 were composed of fuel from the leading or trailing end of the liquid fuel slug. If a gamma-emitting "tag" nucleus could be incorporated into one or more of the initial fuel pellets, the axial distribution of the "tagging" nucleus after the experiment should reveal any strong tendency for fuel from different axial portions of the fuel load to freeze at different axial locations in the freezing channel. Based on their neutron absorption cross sections, gamma spectra, and relative abundances, suitable tag elements include Ir, Sc, Hf, and Tb. Table 5-III shows the energy of the most intense gamma-ray for each element, along with a "quality factor" (QF) for each element that combines the gamma-ray energy, the natural abundance, and the neutron activation cross section.

Table 5-III

#### Properties of Suitable Tagging Elements

<u>Element</u>	<u>E<sub>g</sub> (MeV)</u>	<u>Quality Factor (QF)</u>
<sup>192</sup> Ir	0.32	230
<sup>46</sup> Sc	0.889	18
<sup>181</sup> Hf	0.482	5.6
<sup>160</sup> Tb	0.879	30

The chemical compatibility with UO<sub>2</sub> of several possible tagging elements (Hf, Tb, Sc, Ta) was investigated, and foils of several of these materials were ordered. When the foils are received, some of them will be irradiated in the ACRR with a neutron spectrum characteristic of TRAN experiments, to measure typical signal levels relative to fission-product lines now used to map the final fuel distribution.

As an initial test of the tagging concept, it would be possible to insert some of these foils between individual test fuel pellets. After considering the probable signal levels

and boiling temperatures of Hf and Sc, it seems best to place Hf discs near the leading end of the fuel load, where total pressures are lower, and Sc near the trailing end.

#### 5.2.4 PLUGM Code Development and Experiment Analysis

##### 5.2.4.1 Completion and Documentation of PLUGM-I Code

The PLUGM topical report/code user's manual was completed. A version of the code consistent with that report has been archived as PLUGM-I and is available for distribution. This version of the code uses an integral energy balance method (polynomial temperature profiles in crust and wall with time-dependent coefficients) to determine crust growth and wall heatup. Both finite and infinitely--thick walls are considered for the thermal solutions, but wall melting is not treated. The film deposition calculation in the code (due to finite-mass effects) accounts for both steady-state film deposition as well as enhanced film thickness caused by Taylor instabilities. These modeling features allow for an accurate analysis of a low wall temperature experiment such as TRAN-1.

##### 5.2.4.2 Development of PLUGM-II Code

The released version of the PLUGM code, PLUGM-I, corresponding to the topical report, uses an integral energy balance method to determine crust growth and wall heatup. Although in principle it is possible to extend this methodology to treat the case of wall melting, this approach does not appear to offer significant benefits (simplicity, code running time, etc.) over more conventional solution techniques such as finite differencing. Further, the desirable feature of being able to treat temperature-dependent properties is more readily implemented in a finite-difference solution scheme. For these reasons, it was decided to implement a new version of the PLUGM code, PLUGM-II, based on a finite-difference solution scheme for the crust growth and wall heatup.

In the context of a plugging and freezing code such as PLUGM, there are two phase transition problems that must be addressed, crust growth and wall melting. In the PLUGM-II heat transfer formalism, these two melting and freezing problems are treated differently. A general finite-difference heat transfer mesh is shown in Figure 5.2-5. The surface of the crust is located at radial position  $r$ , and the material beyond  $r$  is the bulk fluid at temperature  $T_b$ . For a typical node,  $i$ , in the interior of the crust or wall, the radial conduction equation takes the form:

$$\rho c_p V_i \frac{\partial T_i}{\partial t} = \left( \frac{KA}{\Delta r} \right)_{r_i, r_{i+1}} (T_{i+1} - T_i) + \left( \frac{KA}{\Delta r} \right)_{r_i, r_{i-1}} (T_{i-1} - T_i) \quad (5.1)$$

where

$\rho$  = material density

$c_p$  = material specific heat

$V_i$  = volume of node  $i$

$\left(\frac{KA}{\Delta r}\right)_{r_i, r_{i+1}}$  = conductance between radii  $r_i$  and  $r_{i+1}$

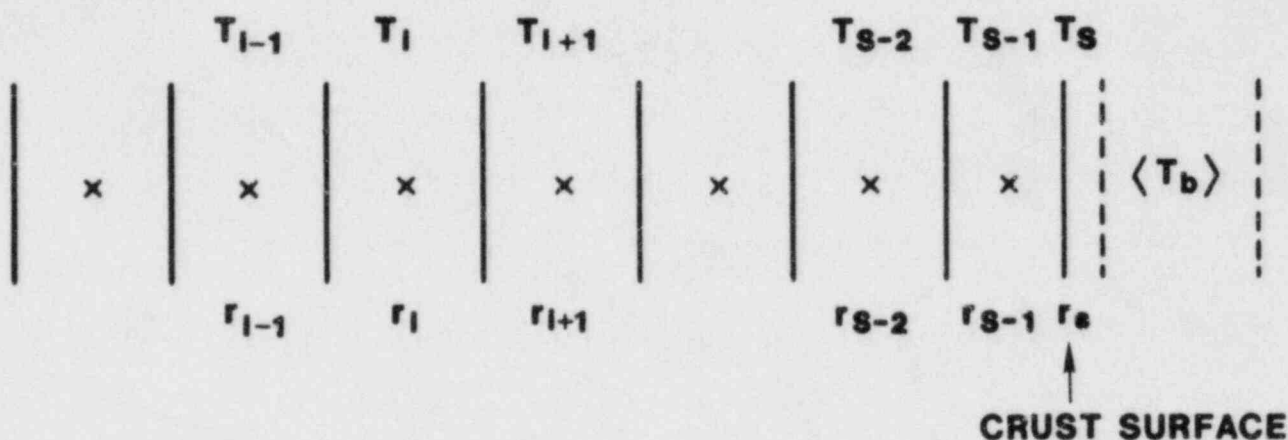


Figure 5.2-5. Finite-Difference Mesh Used in PLUGM-II Calculation

For melting or solidification in one of these nodes (wall melting or refreezing), the standard practice is to perform an enthalpy correction to the temperature  $T_i$  to account for the heat of fusion. An iterative procedure is then used to determine a new value for  $T_i$  that is consistent with both the conduction equation as well as the local melting or solidification. This procedure determines an average temperature for the partially molten node  $i$ . An estimate of the melt fraction for the node (or melt radius) can be obtained by assuming that the solid portion of the node exists at the solidus enthalpy and that the liquid portion of the node exists at the liquidus

enthalpy. This is the procedure used in PLUGM-II to determine the extent of wall melting.

The above procedure does not lend itself very well to the analysis of crust melting or solidification, because the outer crust node dimension actually changes in time ( $r_s$  varies with time). The equation that defines the temperature of the last crust node is written as:

$$\begin{aligned} \rho c_p V_{s-1} \frac{\partial T_{s-1}}{\partial t} &= \left( \frac{KA}{\Delta r} \right)_{r_s, r_{s-1}} (T_s - T_{s-1}) \\ &+ \left( \frac{KA}{\Delta r} \right)_{r_{s-1}, r_{s-2}} (T_{s-2} - T_{s-1}) \\ &+ \rho c_p (T_s - T_{s-1}) \frac{\partial V_{s-1}}{\partial t} \end{aligned} \quad (5.2)$$

This equation is similar to the equation for a general interior node  $i$ , with the addition of the term involving the time derivative of the node volume  $V_{s-1}$ . This time derivative can be determined directly by considering the boundary conditions at the crust surface. These are:

$$T_s = T_{\text{solidus}}$$

$$\begin{aligned} [\rho L + \rho c_p (T_b - T_s)] \frac{\partial V_{s-1}}{\partial t} &= \left( \frac{KA}{\Delta r} \right)_{r_s, r_{s-1}} (T_s - T_{s-1}) \\ &- hA_s (T_b - T_s) \end{aligned} \quad (5.3)$$

These equations simply state that the crust surface temperature is the solidus temperature of the crust material and that the rate of crust formation (or remelt) is determined by the difference between heat flow into the crust from the bulk fluid and the heat flow away from the crust surface via conduction. Thus, the modified matrix equation is used for the last crust node and the crust surface boundary conditions are used to iteratively determine the new temperature array and the new crust dimensions (from the time derivative of volume  $V_{s-1}$ ).

The above procedure was implemented into the code for both slab and cylindrical geometry. This new version of the code was then used to recalculate the TRAN-1 experiment for comparison with the PLUGM-I results. That particular case did not involve wall melting, and the agreement between the two versions of the code was excellent.

In addition to the new heat transfer algorithm, the use of temperature-dependent properties was also implemented.

#### 5.2.4.3 Analysis of the TRAN B-1 Experiment

A detailed analysis of the TRAN B-1 experiment has been performed using the PLUGM code. Previous PLUGM analyses of TRAN Series I experiments had required that substantially less than 100% of the initial fuel mass be used in the calculation. Series I has a substantial amount of fuel drained (or dispersed) below the melt chamber rather than being injected into the flow channel. Since the PLUGM model cannot account for this draining process, it was necessary to simply remove that fuel from the calculation. In TRAN B-1, only a small amount of fuel (~15%) was found to be below the fuel melt chamber at the end of the experiment. In addition, about 7 g of fuel accumulated in a slot in the outer channel wall at the exit of the fuel melt chamber. This slot could not be modeled in the PLUGM code. Thus, for these TRAN B-1 analyses, the calculations were performed for a 75-g initial fuel mass. Other parameters (geometry, initial conditions, etc.) used in the analyses include:

- Initial Fuel Temperature = 3600 K (3327°C)
- Initial Wall Temperature = 875 K (602°C)
- Driving Pressure = 1.0 MPa

The PLUGM code calculates liquid-film deposition on the channel surface at the trailing edge of a moving liquid slug based on steady-state film deposition enhanced by Taylor instabilities. Earlier PLUGM analyses of TRAN Series I experiments had used an early version of the code in which the calculation of steady-state liquid-film deposition was based on a film thickness that was characterized by a cross-sectional area of 15% of the available channel area. This approximation had substantial experimental basis from results in tube geometry, and this model had given excellent agreement with the crust/film measurements for Series I experiment TRAN-1.[5-7], [5-8] However, for an annular channel, such as the one used in TRAN B-1, there is a large uncertainty in the amount of liquid-film deposition. Liquid-film deposition experiments performed in annular geometry have shown a large variation in deposited film thickness, with areal coverage fractions varying from ~13% to as high as ~25%, depending on the details of the velocity and materials used. Thus, a simple areal coverage fraction criterion, used for the tube geometry, is not possible. However, a mechanistic film deposition calculation that accounts for material properties is beyond the scope of the PLUGM code. Rather than trying to provide such a mechanistic calculation, two parametric PLUGM calculations were performed, using 15% and 25% film deposition criteria, respectively. These two calculations should bound the actual film deposition in the annular channel.

The results of the two calculations are qualitatively very similar. The principal difference is that the calculated penetration distance is somewhat shorter for the 25% film deposition case. The position of the molten fuel slug as a function of time and the velocity at the leading edge of the fuel slug as a function of time are shown in Figures 5.2-6 and 5.2-7, respectively, for the 15% film-deposition case. These same results are shown in Figures 5.2-8 and 5.2-9 for the 25% film-deposition case. Both cases show the same general behavior: the molten fuel slug moves up the channel, shrinking by mass depletion at the trailing edge of the flow and consequently accelerating as it moves up the channel. The early-time discontinuity in velocity seen in Figures 5.2-7 and 5.2-9 results from the flow area change (discrete in PLUGM model) at the entrance to the annular channel. The 15% film-deposition case has a total penetration distance of 58 cm with a flow time of 49.5 ms. The penetration distance and flow time for the 25% film-deposition case are 45 cm and 42 ms, respectively. Thus, the penetration distance is in somewhat better agreement with the experimental value (40.5 cm) for the 25% film-deposition case. However, even for the 25% deposition case, the calculated flow time of 42 ms is substantially longer than that inferred from the pressure transducer history (22.5 ms). In both cases, the average velocity between 5 cm into the channel and 25 cm into the channel (the TC locations) is 12 m/s, as compared to the experimentally determined value of 15.7 m/s.

The effect of the different film-deposition criteria can also be seen in the final axial crust (plus liquid film) distributions. These final crust distributions are given in Figures 5.2-10 and 5.2-11 for the 15% and 25% film-deposition cases, respectively. As can be seen from these figures, the liquid-film thickness is substantially larger in the 25% film-deposition case. Thus, the total crust (crust plus liquid film) thickness is about 25% larger than for the lower film-deposition case.

It should be noted that the PLUGM-calculated values shown in Figures 5.2-10 and 5.2-11 represent average values for the inner (rod) and outer (tube) surfaces of the annular channel. In reality, the photomicrographs show that the crust on the outer surface is somewhat larger than the crust on the inner rod. These measured crust thickness values are also shown in Figures 5.2-10 and 5.2-11 for comparison with the calculated values. Whereas PLUGM does predict slightly different crust thicknesses on inner rod and outer surface due to heat transfer effects, this effect is much smaller than the observed differences. The larger observed differences are thought to be caused by differences in film deposition on the two surfaces. Such details of the film deposition process are, however, beyond the scope of the PLUGM code; the assumption is simply made that the film thicknesses are the same on inner and outer channel surfaces.

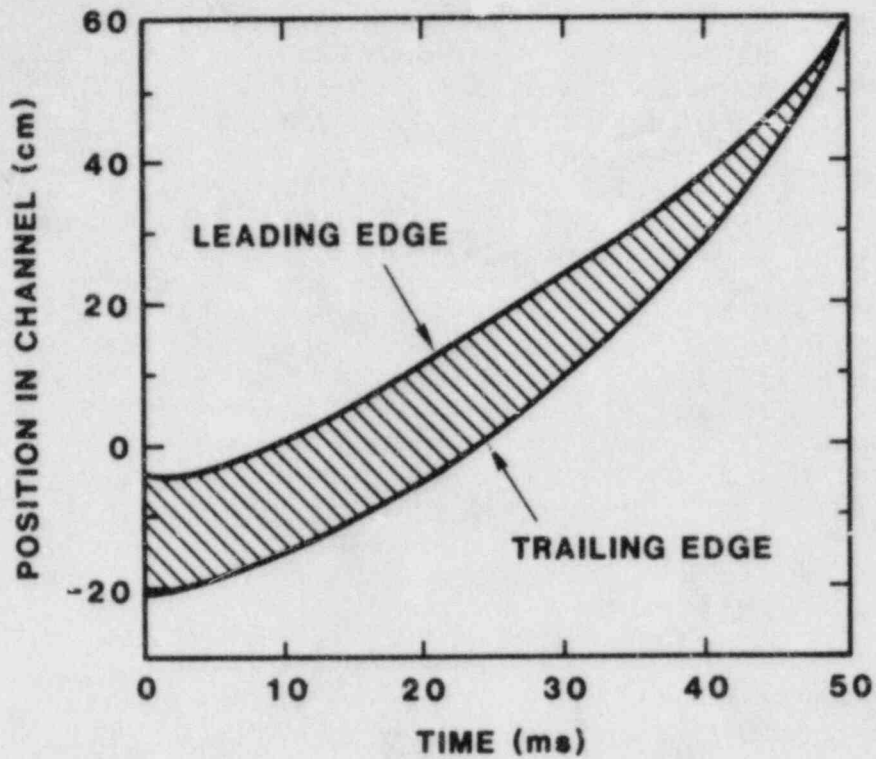


Figure 5.2-6. Molten Fuel Slug Position as a Function of Time (15% Film-Deposition Case)

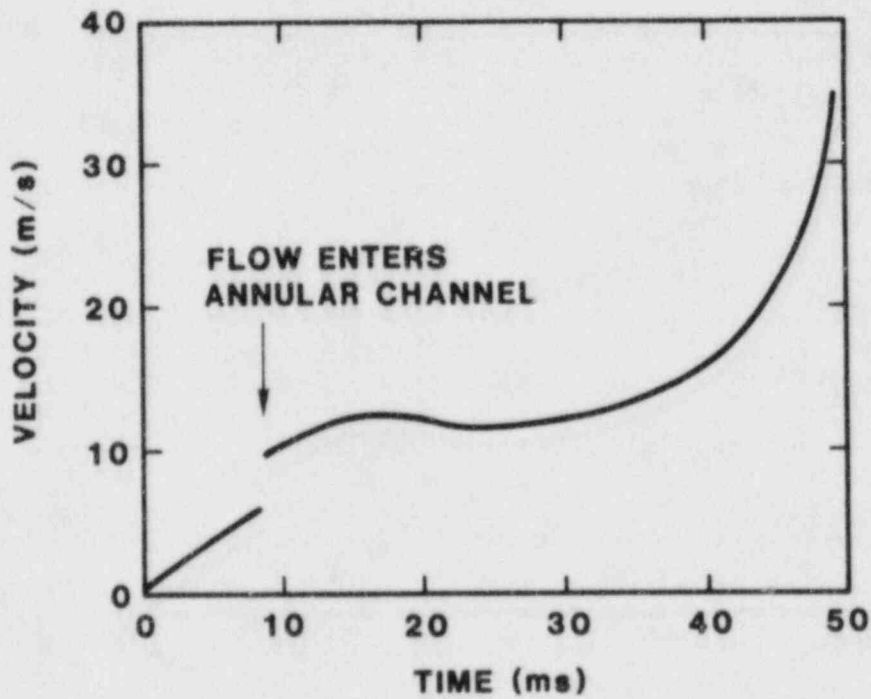


Figure 5.2-7. Leading-Edge Velocity as a Function of Time (15% Film-Deposition Case)



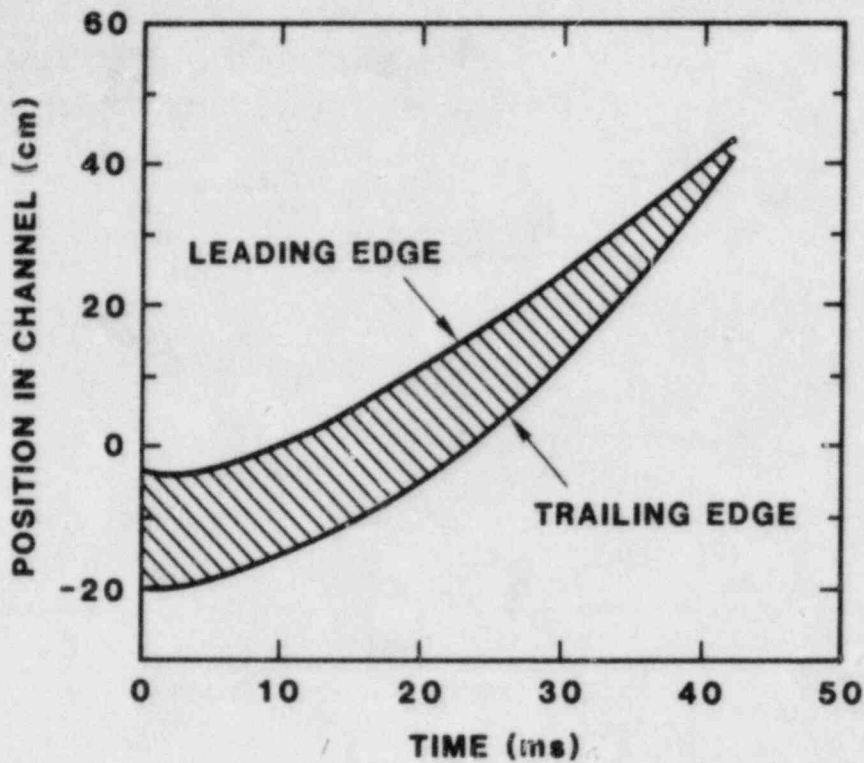


Figure 5.2-8. Molten Fuel Slug Position as a Function of Time (25% Film-Deposition Case)

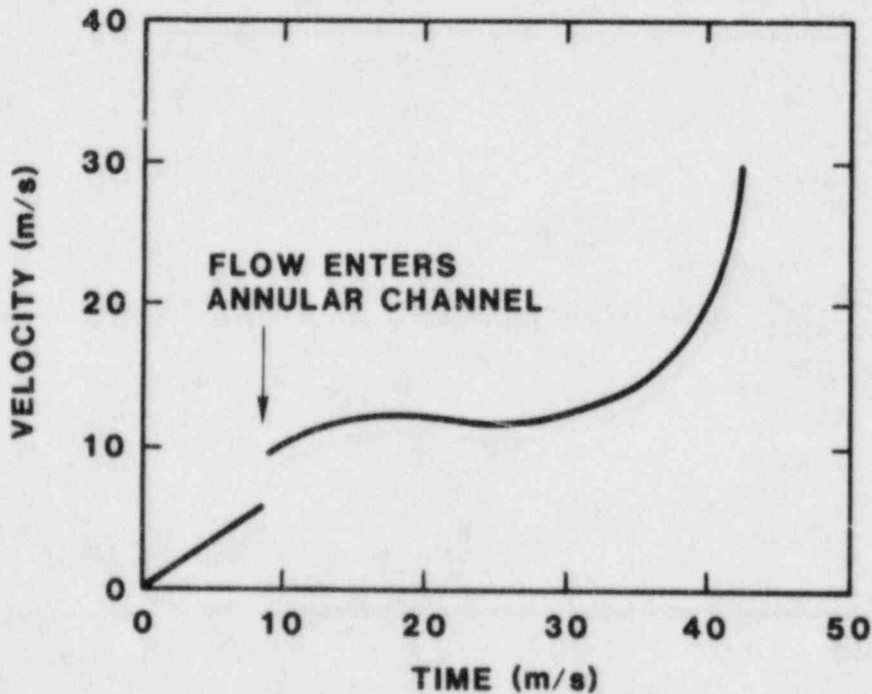


Figure 5.2-9. Leading-Edge Velocity as a Function of Time (25% Film-Deposition Case)

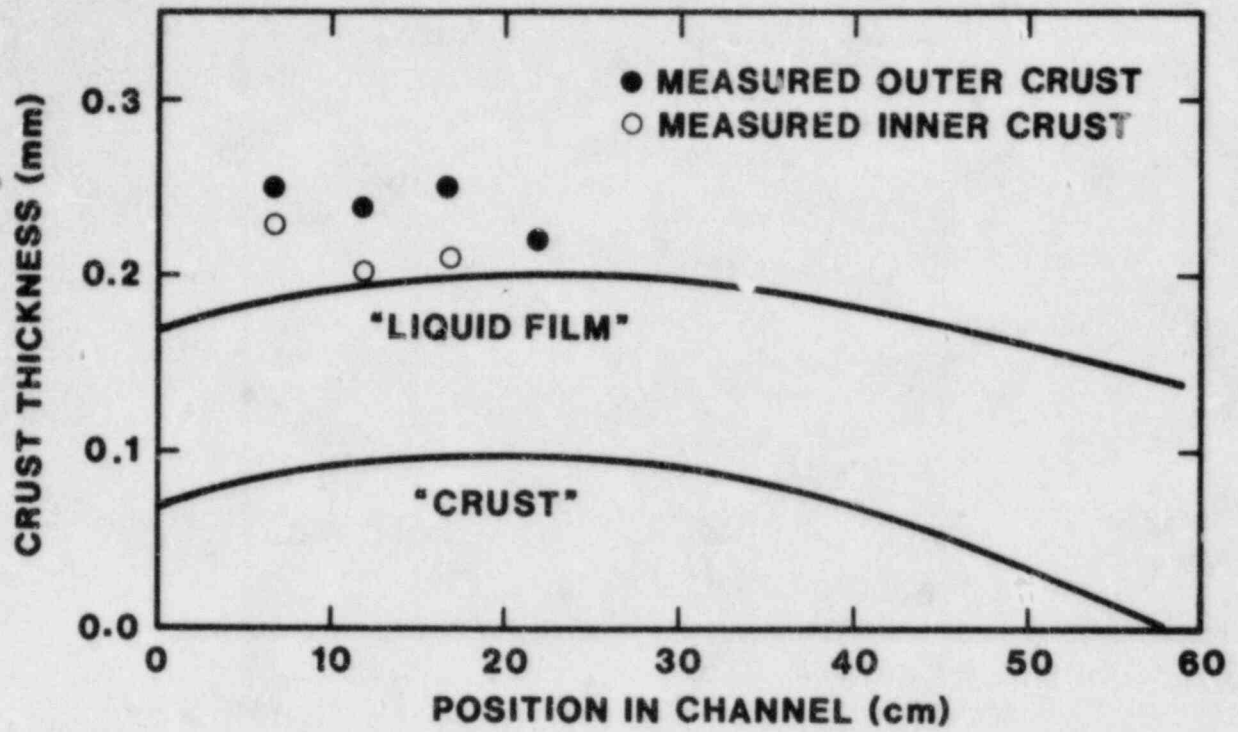


Figure 5.2-10. Final Axial Crust Distribution (15% Film-Deposition Case)

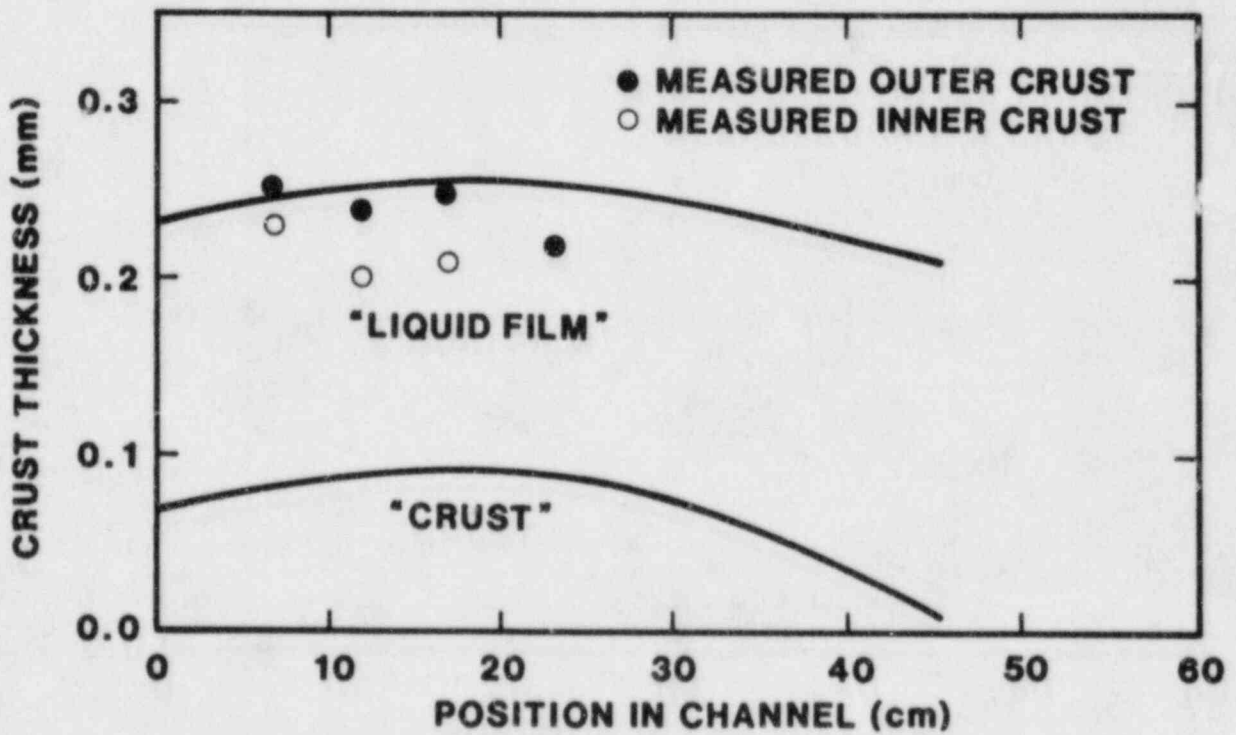


Figure 5.2-11. Final Axial Crust Distribution (25% Film-Deposition Case)

Qualitatively, the PLUGM analyses are in good agreement with the experimentally observed results in TRAN B-1. The predicted penetration distance for the 25% film-deposition case is only slightly longer than that observed in the experiment. The predicted (average) crust thickness is also within ~10% of the measured values. The largest discrepancy between calculation and experiment is in the predicted vs. measured (inferred from pressure transducer data) duration of the fuel flow. A significant discrepancy also exists in the predicted and measured average fuel velocity between TC locations. Separate-effects calculations performed at Sandia suggest that the higher velocities observed in the experiment may be caused by small amounts of trapped gas in the fuel sample. This trapped gas would provide an internal pressure source in the fuel and result in higher leading-edge velocities. Future analyses are planned to investigate this effect further.

#### 5.2.5 TRAN Series III "GAP" Design

The TRAN-GAP experiments differ from those performed previously in that a significantly larger mass of fuel (2 kg of fresh  $UO_2$ ) is to be driven downward into a rectangular freezing channel (nominally 0.4 by 7 cm) under driving pressures ranging from zero (gravity flow) to 10 bars. This geometry represents the intrachannel subassembly gaps that exist in the lower axial blanket regions of LMFBR designs, such as CRBR. Shown in Figure 5.2-12 is a schematic of the experiment package illustrating the key components and concepts. The entire experiment package is encased in a large stainless tube (7.5 in. in diameter by 12 ft in length), which constitutes the principal containment boundary. The fuel load is housed in a stainless steel annulus, surrounded by insulators and steel shields within the containment canister. Using the ACRR multiple-pulse mode, approximately 2 kg of fresh  $UO_2$  is to be neutronically heated to a molten state (nominally  $1 \times 10^{17}$  total fissions) and ejected downward from an initial annular geometry in the midcore section, through a funnel-shaped flow transition region and into the rectangular flow channel. Initial fuel motion is achieved by applying a gas (helium) pressure to the upper section of the annular fuel melting channel (Figure 5.2-12) as the fuel becomes molten. A remotely actuated solenoid valving system, similar to that used in TRAN Series I and II, will be used in the GAP experiments to apply a gas pressure to the melt. As the liquified fuel enters the rectangular freezing channel, flow may proceed either by the force of gravity or by continued application of a driving pressure.

Fuel motion down the freezing channel will be monitored by an array of TCs that penetrate the channel wall at various axial locations. Each TC will successively come into contact with the melt front as the molten fuel proceeds downward, providing data on melt front velocity and penetration. Heat will be transferred to the steel boundaries as the fuel proceeds

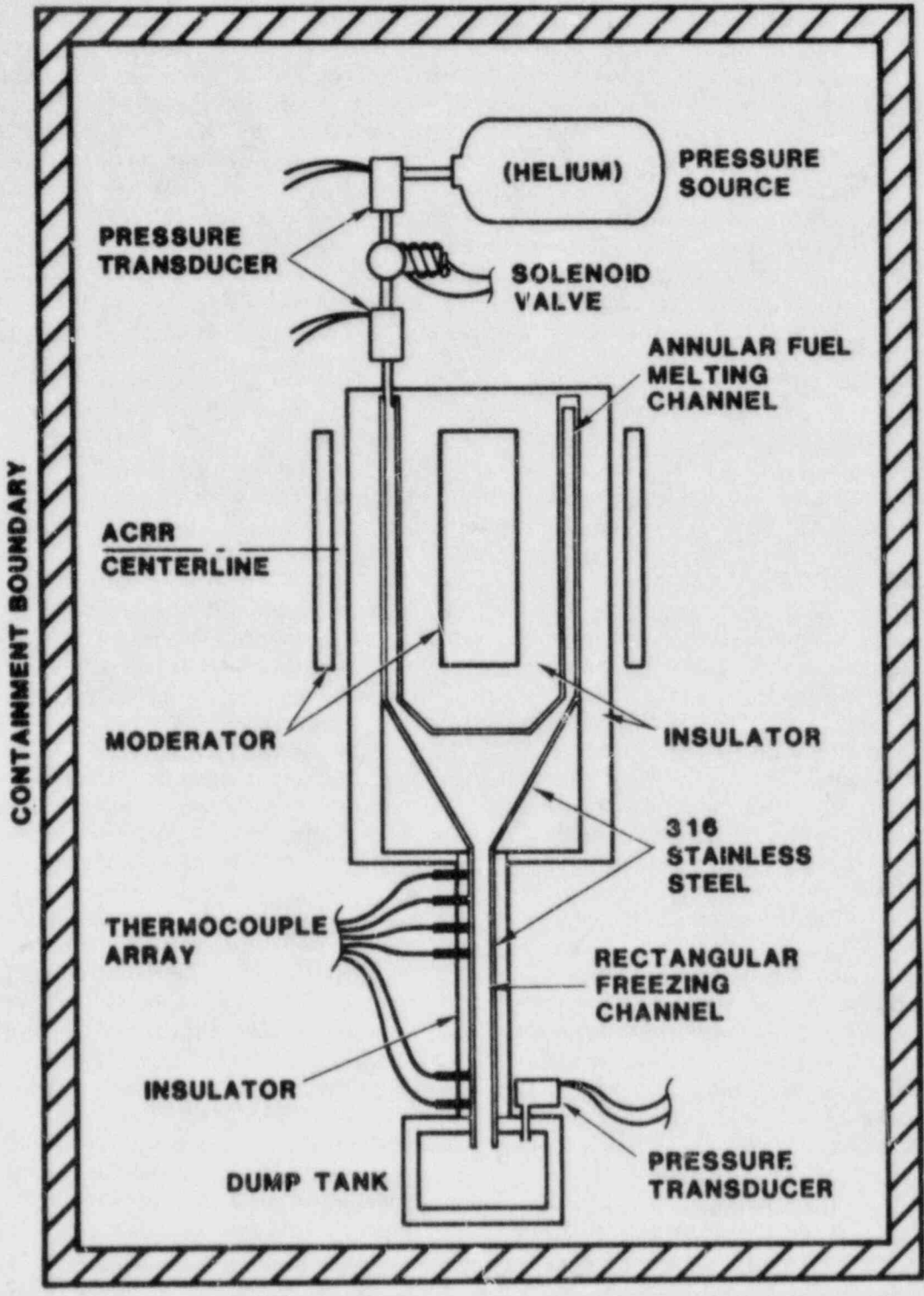


Figure 5.2-12. Schematic of the GAP Experiment Package

downward, leaving a thin crust of frozen fuel behind the flowing fuel mass. Eventually when enough heat has been transferred to the bounding steel walls, the fuel will refreeze, in either the melt funnel, the freezing channel, or the massive steel dump tank at the bottom of the freezing channel. Pressure transducers shown on either side of the solenoid valve and on the dump tank will record the pressure history associated with the fuel motion to facilitate posttest analysis.

#### 5.2.5.1 Safety Issues

The principal safety issues associated with this design arise due to the high fuel temperatures that threaten containment integrity and potential pressurization sources associated with fill gas heatup or vapor generation. The most severe conditions would arise if the fuel were underheated and failed to leave the annular melting section, where the adjacent steel walls would subsequently melt. The combination of large heat capacities in package construction, secondary steel heat shields and high-temperature zirconia insulators prevent fuel from relocating and from coming into contact with the containment. No significant heat loads to the containment occur under these conditions. An in-containment auxiliary heat sinking system is available for use after the reactor transient in case cooling of the internal moderator is required. This system is intended primarily to prevent damage to the internal moderator in the event an experiment malfunction subjects the moderator to overheating and subsequent hydrogen evolution. Thermal calculations indicate that if  $ZrH_{1.8}$  is used as the inner moderator, no active internal heat removal is required. In some instances, however, using polyethylene for the inner moderator may be desirable; and the active internal cooling is necessary for heat removal should a significant percentage of the fuel fail to leave the melting channel. This heat removal prevents decomposition of the polyethylene and avoids any pressurization of containment. A large internally contained heat sink is available for any transient high-level heat fluxes to the moderator cooling jacket, while long-term heat removal is effectively accomplished by transfer through the containment wall. External package cooling is attained via cavity purge, with air ( $60 \text{ ft}^3/\text{min}$ ). This external cooling system removes heat passing through the containment wall during the slow cooldown period following completion of the experiment.

#### 5.2.5.2 Experiment Design Basis

The design basis of this experiment package will allow investigation of fuel melt temperatures up to 3000 K ( $3527^\circ\text{C}$ ) where freezing channel preheat temperatures range up to 1000 K ( $727^\circ\text{C}$ ), and driving pressures are as high as 10 bars (about 150 psi). Fuel composition for the first four experiments will be either fresh  $UO_2$  or mixtures of up to 25 vol%

stainless steel with fresh  $\text{UO}_2$ . The presence of steel particles in the test fuel presents an additional safety issue associated with steel vapor generation. This is principally a pressurization problem. The current design presented in this plan is for pure fuel melts and will be modified somewhat for use with fuel/steel mixtures as required, given the magnitude of the pressurization potential. The channel wall thickness may be a secondary parameter in later experiments. Thick walls (with large wall heat capacity) would simulate the presence of liquid sodium at channel wall boundaries (this design), and thin walls would be more prototypic of sodium-voided channel regions (future design modification). The range of experimental parameters is summarized in Table 5-IV.

Table 5-IV

Range of Experimental Parameters

Fuel temperature	Up to 3800 K (3527°C) (3700 K (3427°C) for fuel/steel)
Freezing channel	Up to 1000 K (727°C)
Driving Pressure (differential)	Up to 10 bars
Fuel composition	Up to 25 average vol% 316 SS with fresh $\text{UO}_2$ (20% enriched)
Fuel mass	2 kg
Neutron moderation:	
Ex-containment	Up to 1/2-in. annular thickness of polyethylene
In-containment	Either $\text{ZrH}_{1.8}$ or up to 1/2-in. annular thickness of polyethylene

### 5.2.5.3 Description of the Apparatus

#### a. Fuel Melting Section

The fuel melting section of the experiment package is shown in Figure 5.2-13. The fuel annulus is assembled from about 80 stick-shaped extruded elements, nominally 5 mm square on end by 12 cm in length. The elements rest upon a ledge machined into the steel wall that encases the fuel on both

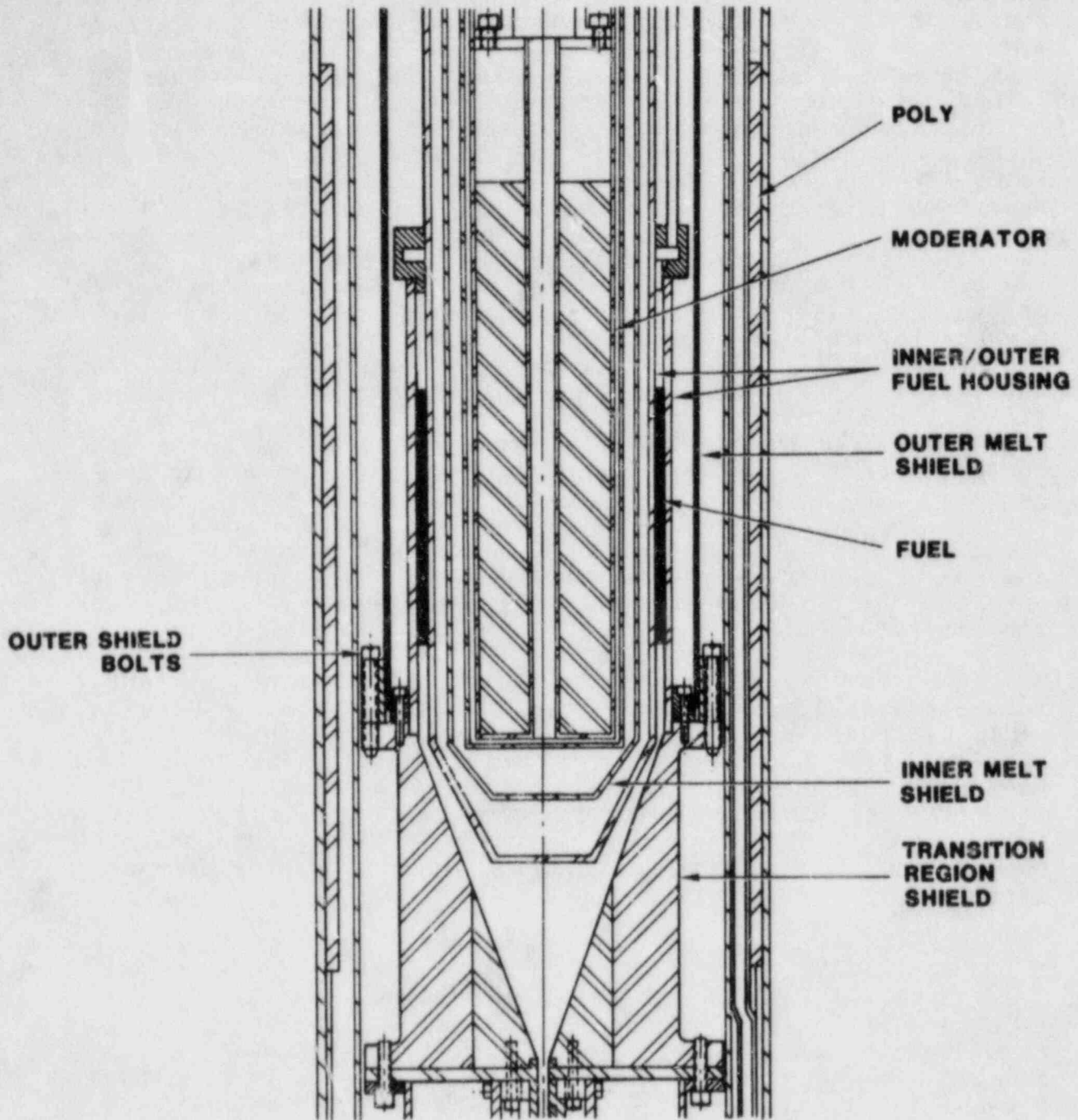


Figure 5.2-13. Fuel Melting Section of the GAP Experiment

sides. Adjacent to the steel casing on either side is a layer of zirconia felt insulator, a secondary steel liner, and another layer of zirconia felt insulator. The secondary steel liners serve to add structural integrity to the fuel melting section in the event the primary fuel casings should be threatened by excessive temperatures and are mounted to accommodate the axial thermal expansion associated with the rapid heating of the inner steel casings enclosing the fuel load. Internal to the innermost zirconia layer is a series of thin-walled steel cans encasing an annulus of zirconium hydride, which serves as a moderator to the inner surface of the fuel load. The zirconium hydride is sealed in the inner can. Provision is made for the flowing of a coolant through the 2-mm gap between the inner and outer moderator cans should excessive temperatures be detected at this location. This feature was included in the design to preclude any possibility of hydrogen degassing of the internal moderator in the event an unexpectedly large heat load threatens this section. The containment wall (304 SS) lies just beyond the outermost layer of zirconia insulator. An outer steel shell houses the containment canister and serves as a guide tube, centering the experiment in the ACRR lower hex cavity. To remove any heat conducted to the containment boundary from the inside of the package, cooling air is released at the bottom of the package between the containment canister and the exterior shell. An additional degree of external moderation is provided by an annulus of high-density polyethylene, which rests against the exterior shell in the gap between the containment canister and the exterior shell.

Upon melting, the fuel flows downward, leaving the annular melting section and entering a heavy wall flow transition region (Figure 5.2-13). Also constructed of stainless steel, this section funnels the molten fuel into the rectangular flow area formed by the freezing channel. The heavy steel construction of this section insures ample heat capacity to safely contain the full 2-kg fuel melt should freezing occur in this area. Adiabatic equilibration temperatures are approximately 700 K (427°C).

#### b. Freezing Channel

It is anticipated, however, that the molten fuel will flow into the freezing channel gap (Figure 5.2-14) leaving a thin crust of frozen fuel on the walls of the channel, and finally, if enough heat is transferred to the walls from the flowing fuel, the liquid may freeze into a plug somewhere along the channel length. The velocity and time-dependent axial position of the flowing molten fuel will be recorded through the rapid rise in local temperature sensed by an axial array of TCs penetrating the freezing channel wall. Nineteen chromel-alumel TCs (40-mm O.D. stainless steel sheath) are mounted in the freezing channel wall, spaced nominally 10 cm



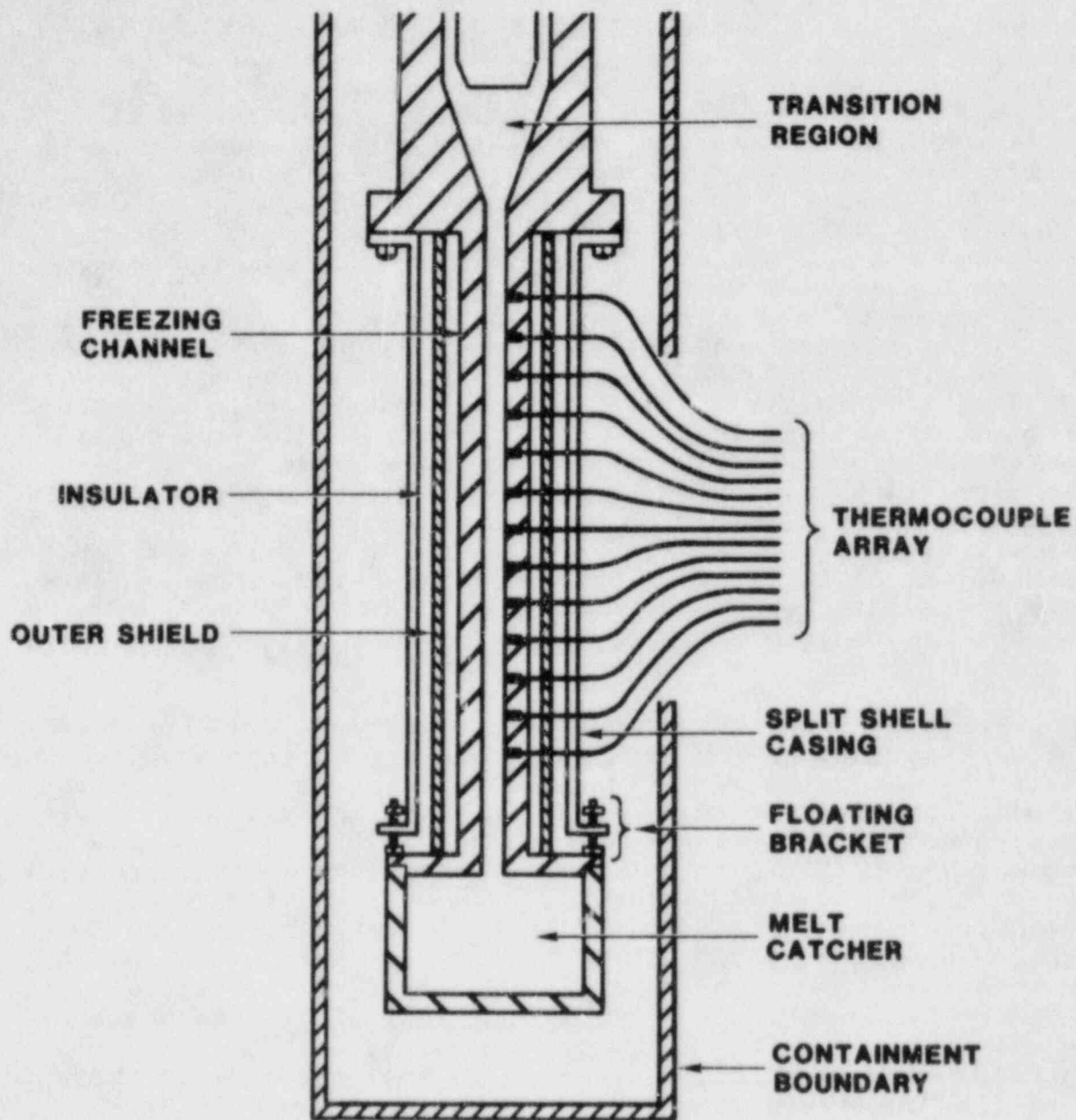


Figure 5.2-14. The Fuel Freezing Channel (Schematic)

apart over the 74-cm length of channel wall with a 5-cm spacing used over the first 15 cm of channel length. With two TCs at each axial station, time positioning and flow profile information may be determined.

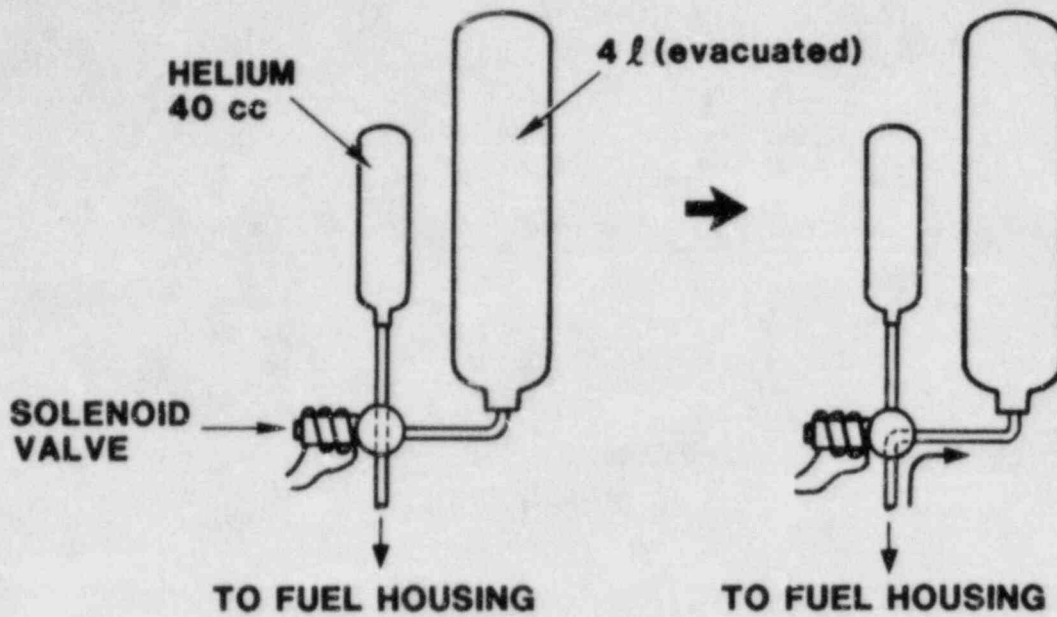
The freezing channel will be preheated to somewhere between 775 and 1175 K (502° and 902°C) (the saturation temperature of sodium) by axial heaters, which are situated against the channel exterior wall. An axial thermal gradient may be required in some experiments. A layer of dense zirconia insulator surrounding the heater-channel assembly restricts heat loss to the exterior channel structures. A second steel wall encases the zirconia-freezing channel assembly and provides massive heat sink and structural integrity to the inner channel structures should the inner channel materials reach excessive temperatures.

Any fuel that penetrates the full length of the freezing channel will come to rest in a melt catcher. The catcher has enough heat capacity to safely contain the entire fuel melt with all the initially added enthalpy. The adiabatic equilibrated temperature of the melt catcher, with full initial fuel enthalpy, is 620 K (347°C). A Kaman Sciences pressure transducer is mounted at the end of a short tube that penetrates the lid of the melt catcher. This transducer will measure the pressure ahead of the flowing fuel so that the actual differential driving pressure may be determined.

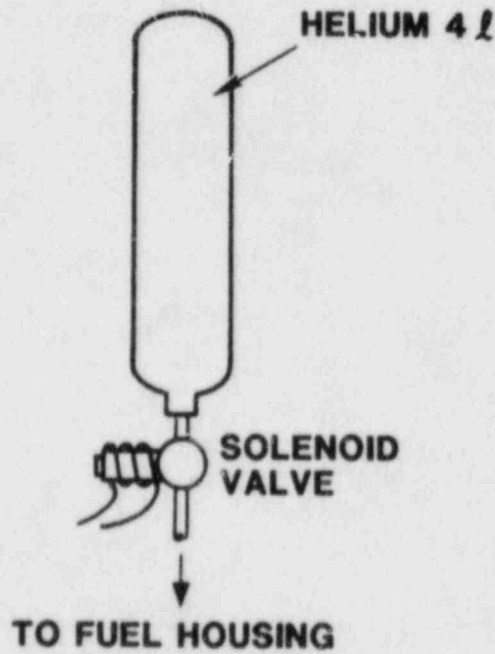
### c. Pressure System

A standard Department of Transportation (DOT) pressure cylinder is used to contain the helium gas, which, when released by actuation of the solenoid valve (Circle Seal Series SV30) will drive the molten fuel into the freezing channel. The technology of this pressure system is the same as used in the earlier TRAN experiments. Two variations of this pressure system are to be used, depending upon whether gravity flow or pressure-driven conditions are to be implemented. These options are illustrated in Figure 5.2-15. In the case of gravity flow conditions, a relatively small (40-cm<sup>3</sup>) pressure cylinder will be used as a source of initial driving pressure to move the molten fuel out of the melting section and into the flow transition funnel. At that time, the applied pressure will be vented to a large evacuated bottle so that the remainder of the fuel motion may proceed under gravity flow conditions with only a small differential driving pressure. Alternatively, for the pressure driven cases, a large (4-l) pressure bottle contains the driving gas that when released to the fuel melting section, remains applied for the duration of the experiment.

Kaman Sciences-type pressure transducers are used to measure the bottle pressure, solenoid valve pressure drop, and fuel load differential driving pressure. Additionally, a



A) Initial impulse to fuel, later relieved to evacuate bottle for gravity flow case



B) Constant applied pressure throughout experiment

Figure 5.2-15 Pressure Systems To Be Used in TRAN GAP Experiment Package

transducer is also located outside of the pressure system that monitors the containment canister pressure throughout the experiment. The containment canister will be purged and filled with helium to approximately 1 bar ambient pressure.

#### 5.2.5.4 Thermal and Neutronic Analyses

Described in this section are results of analyses that have addressed the neutronic and thermal performance of the fuel within the melting section of the experiment package. The fuel melting section shown in Figure 5.2-13 has been analyzed using the TWOTRAN neutron transport code. Results from this analysis indicate a substantial flux depression exists within the center of the fuel element with a peak-to-average energy deposition ratio of 1.1 on the inner fuel surface, while the outer surface peaking factor is 1.32 (Figure 5.2-16). For the nominal case, the average ACRR-experiment coupling factor was calculated to be 7.2 J/g deposited in the test fuel per MJ of ACRR yield. If the fuel was heated adiabatically with a single ACRR pulse, this energy distribution profile would give rise to outer surface temperatures of 4200 K (3927°C) where the mean fuel temperature was only 3400 K (3127°C). To alleviate this disproportionate heating of the inner and outer surfaces, a double ACRR pulse, which allows a short thermal relaxation interval between pulses, is being used. A reasonable relaxation time between pulses was found to be on the order of 0.5 s. Shown in Figure 5.2-17, a, b, and c are the radial thermal profiles that result following the first pulse, just prior to the second pulse, and just after the second pulse. The most favorable results have been obtained with roughly one-third of the total energy deposited in the first pulse, following with the remaining two-thirds deposited in the second pulse. Using the ACRR-experiment coupling factor of 7.2 J/g/MJ, approximately 210 MJ total ACRR yield is required to bring the mean fuel temperature to 3400 K (3127°C) (1540 J/g). From Figure 5.2-17c, the calculated fuel temperature varies by  $\pm 200$  K (200°C) about the average temperature.

This design is currently being fabricated, and assembly is expected to be completed during the last quarter of calendar 1983.

#### 5.2.5 Participation in Review of ANL Thermite Experiments

Project personnel attended a meeting at Argonne National Laboratory (ANL) with staff from GE, FAI, and ANL to discuss the transition phase experiments being conducted at SNL and at ANL. A summary of both programs was presented followed by a discussion of differences in results between the two programs and hope of better future cooperation.

The most recent experiments involving thermite injection into room-temperature, thick-walled, steel tubes show very

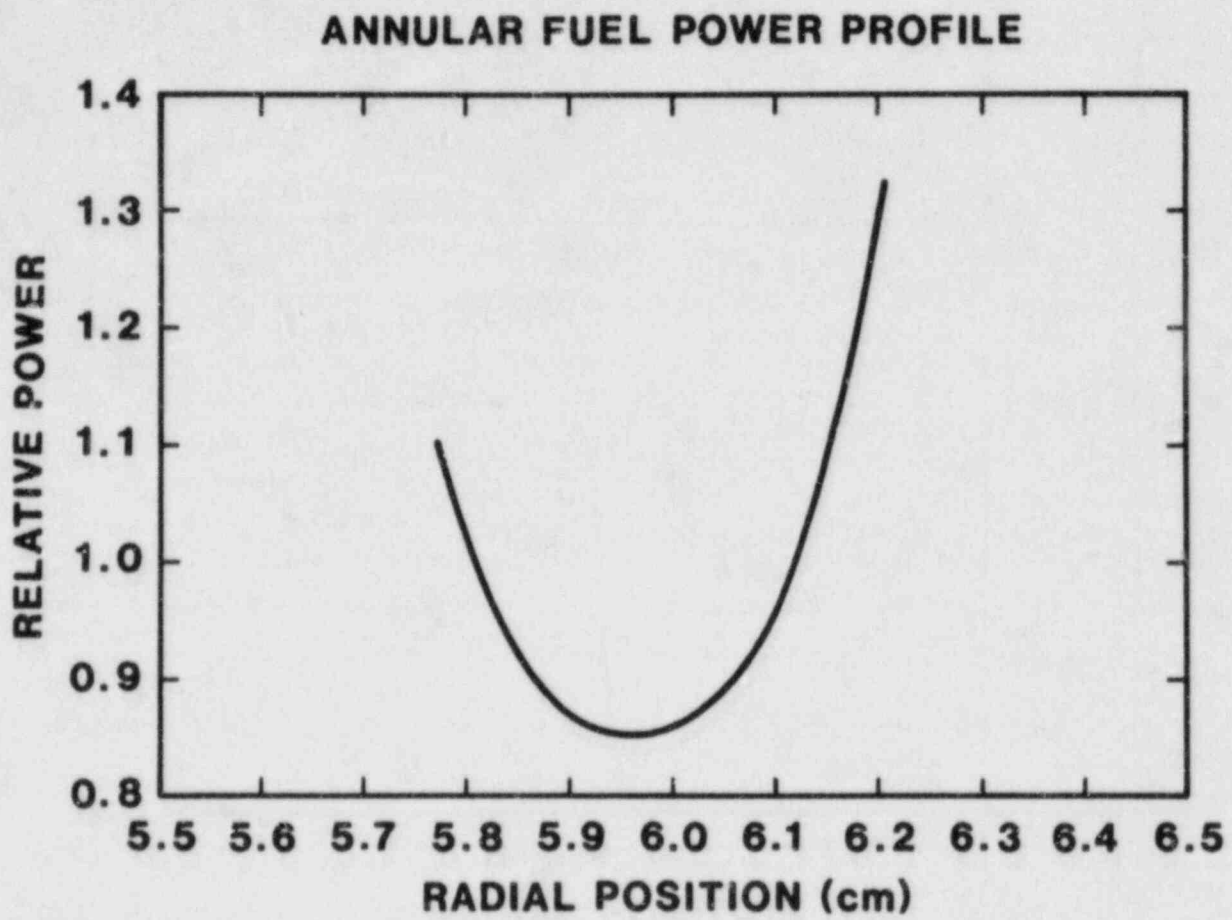
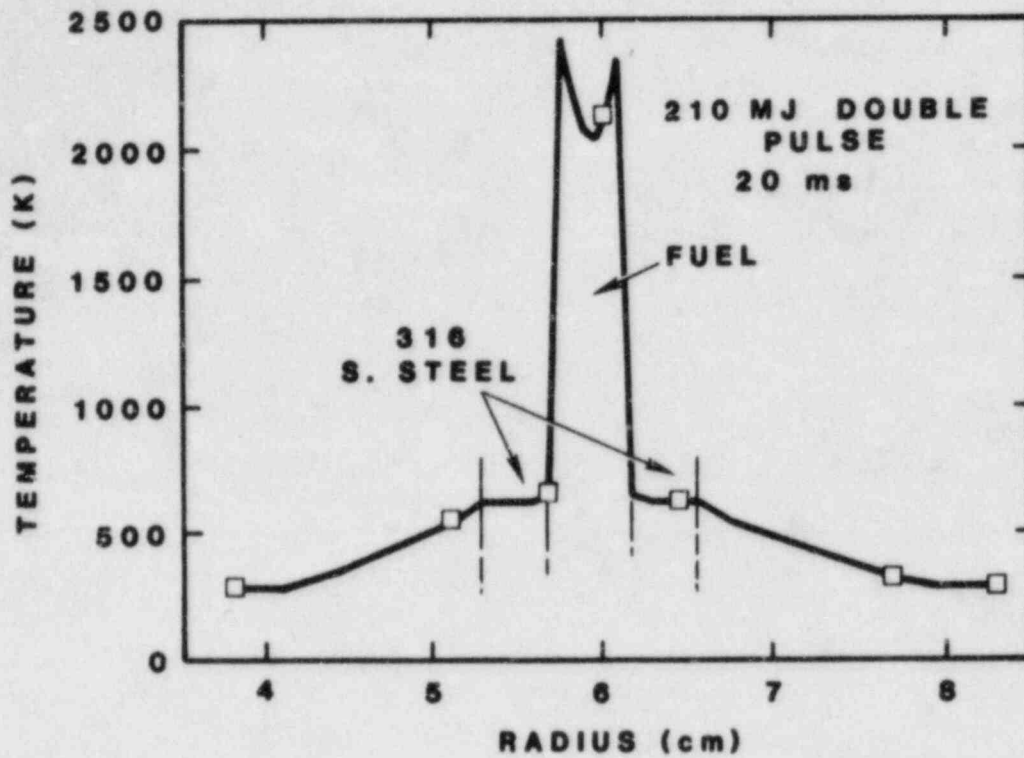
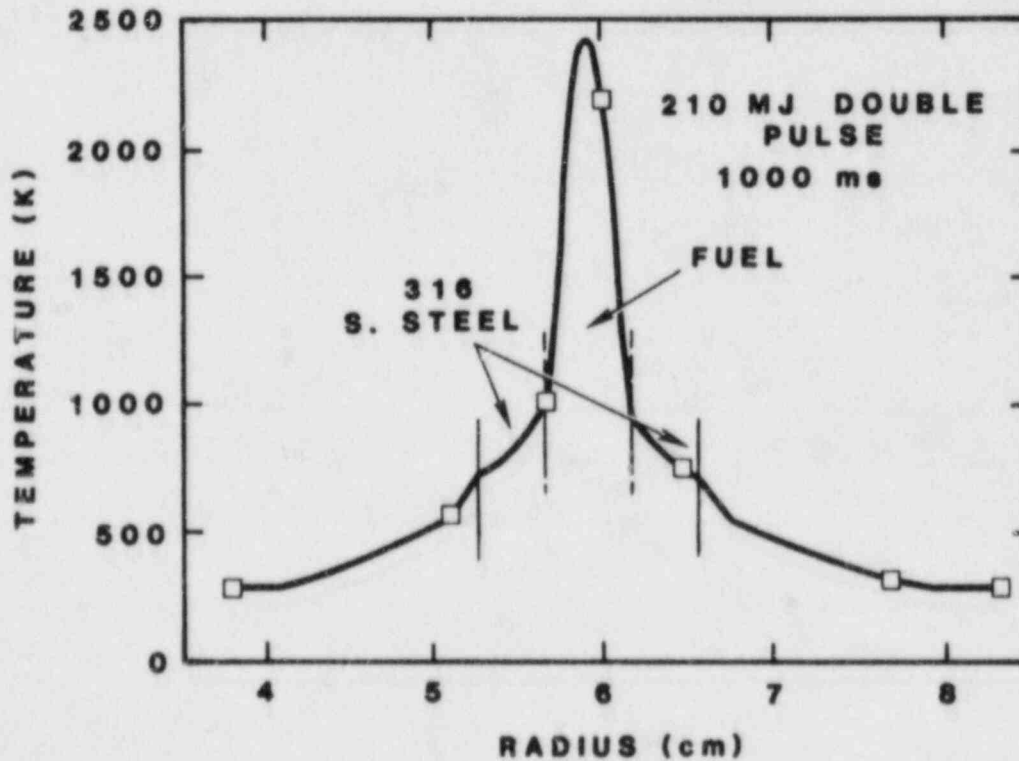


Figure 5.2-16. Radial Fission Energy Deposition Profile (Normalized) through the Annular Fuel Element



(a)



(b)

Figure 5.2-17. Radial Thermal Profiles Characterizing the Two-Pulse Strategy

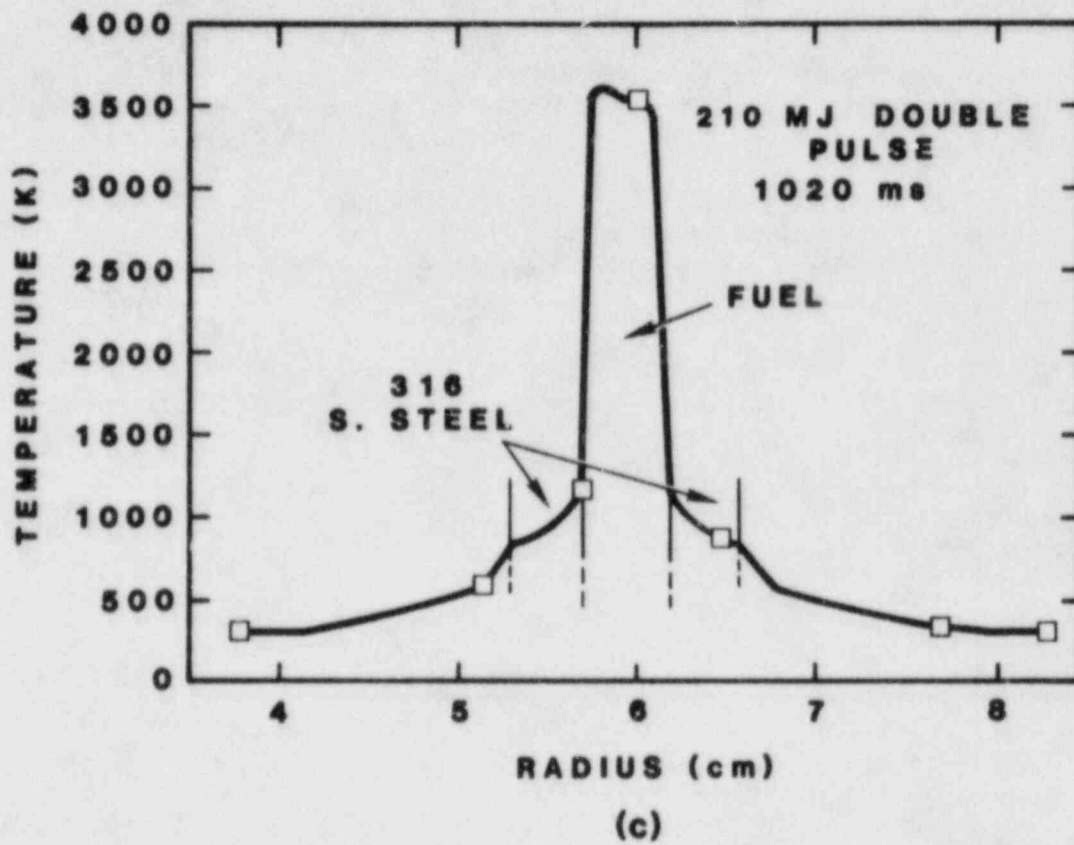


Figure 5.2-17. Radial Thermal Profiles Characterizing the Two-Pulse Strategy

limited penetration (2 to 5 cm) for small-diameter (4-mm) tubes but substantially longer penetrations for tubes greater than 6.35 mm. The very short penetration (which is inconsistent with TRAN Series I results) is probably caused by artifacts associated with the thermite injection process.

One suggestion at the meeting was that Sandia might do a very simple TRAN Series I-type experiment with a larger initial fuel mass and/or a lower driving pressure such that a conduction-type fuel blockage would be expected to occur. This would be useful for verifying existing conduction-freezing models (such as PLUGM). To investigate the requirements for such a test, a series of PLUGM calculations was performed to determine the initial fuel load required as a function of driving pressure so that plugging would occur prior to mass depletion. These calculations indicated that a 180-g fuel load would be required for a driving pressure of 2 bars. Higher driving pressures would require a larger initial fuel load than is possible with current fuel/melt chamber designs.

A firm decision on performing an experiment of this nature has not been made. However, to try such a high-fuel-inventory experiment in the pin channel geometry planned for upcoming B-series experiments would be more feasible. The channel geometry and wall melting behavior would be reasonably prototypic such that any results obtained would be more directly applicable to actual reactor safety analysis.



### 5.3 REFERENCES

- 5-1. Advanced Reactor Safety Research Quarterly Report January-March 1982, NUREG/CR-2679(1 of 4), SAND82-0904(1 of 4) (Albuquerque, NM: Sandia National Laboratories, 1983) p. 5.1-5.33.
- 5-2. S. A. Wright, P. K. Mast, G. Schumacher, "LOF Accident Simulations for Homogeneous and Heterogeneous Core LMFBRs: FD2/4 Series," Transactions of the ANS, Washington, D. C., November 14-19, 1982.
- 5-3. S. A. Wright, P. K. Mast, et al, Fuel Disruption Experiments Under High Ramp Rate Heating Conditions, SAND81-0413, (Albuquerque, NM: Sandia National Laboratories, 1982).
- 5-4. S. A. Wright and P. K. Mast, "Visual Observations of Fuel Disruption in In-Pile LMFBR Accident Experiments," Proceedings of the Conference on Fast, Thermal, and Fusion Reactor Experiments, Salt Lake City, UT, April 12-15, 1982.
- 5-5. S. A. Wright, P. K. Mast, et al, "In-Core Fuel Disruption Experiments Simulating LOF Accidents for Homogeneous and Heterogeneous Core LMFBRs: FD2/4 Series," Proceedings of the International Topical Meeting on Liquid Metal Fast Breeder Reactor Safety and Related Design and Operational Aspects, Lyon, France, July 19-23, 1982.
- 5-6. Advanced Reactor Safety Research Quarterly Report July-September 1981, NUREG/CR-2238(3 of 4), SAND81-1529(3 of 4) (Albuquerque, NM: Sandia National Laboratories, 1981).
- 5-7. D. A. McArthur, N. K. Hayden, and P. K. Mast, In-Core Fuel Freezing and Plugging Experiments: Preliminary Results of the Sandia TRAN Series I Experiments, SAND81-1726 (Albuquerque, NM: Sandia National Laboratories, to be published).
- 5-8. H. K. Fauske, W. D. Ford, and M. A. Grolmes, "Liquid Film Thickness for Slug Ejection," Transactions of the ANS, 13, p. 646 (1970).

## 6. LIGHT WATER REACTOR (LWR) DAMAGED FUEL PHENOMENOLOGY

Sandia's LWR Damaged Fuel Phenomenology Program includes analyses and experiments that are part of the integrated NRC Severe Fuel Damage (SFD) Research Program. Sandia will investigate, both analytically and in separate-effects experiments, the important "in-vessel" phenomenology associated with severe LWR accidents. This investigative effort will provide for three related research programs, the Melt-Progression Phenomenology (MPP) Program, the Damaged Fuel Relocation (DFR) Program, and the Damaged-Core Coolability (DCC) Program. These programs are key elements in the NRC research effort to provide a data base to assess the progression and consequences of severe core-damaging accidents.

## 6.1 MELT PROGRESSION PHENOMENOLOGY

(J. B. Rivard, 6420A; M. F. Young, 6425)

The objective of this program is to provide balanced perspectives and capabilities applicable to that phase of severe LWR accidents starting with initial core damage and progressing through to breach of the reactor vessel and discharge of core materials into the containment environment.

The formal elements comprising this program are:

- a. Core Damage Sensitivity Studies.
- b. Severe Accident Uncertainty Analysis (SAUNA).
- c. Melt Progression Model (MELPROG) Development.

### 6.1.1 Core Damage Sensitivity Studies

Tasking for these studies is being reorganized to provide a more centrally focused report. This report tentatively titled "Considerations in the Behavior of LWR Fuel and Coolant Systems During Severe Accidents" will contain material on accident sequence progression, fuel and core damage, RCS flow and heat transfer, fission product considerations, and the development of test matrices for the DFR fuel damage experiments. This report will incorporate previous studies in these areas.

A six-section format for the report includes:

1. Introduction
2. Accident Progression, Processes, and Consequences
3. Influence of System Processes on Risk
4. Development of Test Matrices for Fuel Damage Experiments
5. Remaining Uncertainties
6. Summary and Conclusions

The first two sections are complete, and initial drafting of Section 3 has begun.

### 6.1.2 Severe Accident Uncertainty Analysis (SAUNA)

For the draft SAUNA report, Identification of Severe Accident Uncertainties, the working group discussed the following items at its meeting.

1. State of completeness
2. Schedules for completion for internal review
3. Sandia reviewers and review approach
4. Working Group comments on contents
5. Definitions

Nine candidate specialists at Sandia have been nominated to perform the peer review. Each will be requested to review as much of the report as he can but to concentrate on the two or three sections that feature areas of his expertise. U.K. specialists will be asked to perform a parallel review on behalf of the U.K. members of the working group.

A final draft was reviewed. A draft cover letter to the Sandia reviewers will be prepared.

### 6.1.3 Melt Progression (MELPROG) Code Development

The Melt Progression Model (MELPROG) calculates the in-vessel part of LWR accident sequences from rubble/debris formation through vessel failure. MELPROG includes models to calculate rubble melting by decay heat and oxidation, structural failure including vessel failure, melt/water interactions, and fission-product transport, plateout, and chemistry.

MIMAS/MELPROG was installed on the Sandia timesharing system. No differences in answers occurred between the computer systems, indicating that MELPROG is running correctly. Calculation of a standard reference case was initiated for the DFR experiment. This involved calculating new view factors for the experiment package and hardwiring of the view factors into MIMAS. This calculation pointed to the need for a more automatic method of view factor calculation for use in MIMAS/MELPROG. Running of the reference case also indicated some problems in the time-step control of MIMAS; these had to be solved.

Coding of the basic structures module for MELPROG was completed on schedule. This package consists of one-dimensional heat transfer routines and creep rupture/melting structural failure models for cylindrical walls, perforated plates supported by columns, and perforated plates supported at the edges. Associated driver, input, and data management routines were also coded.

Debugging of the structures module began. Compilation errors were removed first, and the module was then interfaced to the rest of MELPROG. An input test deck was set up to facilitate run-time debugging.

6.2 LIGHT WATER REACTOR (LWR) FUEL DAMAGE EXPERIMENT  
(A. C. Marshall, 6423; K. O. Reil, 6423; K. T. Stalker,  
6426; F. Horine, 6426; J. Andazola, 6451; J. Garcia,  
6423; P. S. Pickard, 6423)

This program is directed toward examining the key phenomena that determine the core-damage configuration during the progression of a core melt sequence in an LWR core-uncovering accident. This program uses the information and perspectives gained in current LWR safety programs and focuses on the design of experiments that can contribute to the resolution of important severe-damage issues.

The two major areas of interest regarding in-vessel phenomena are:

1. The behavior of fuel and cladding during the stages of major core deformation from rod-bundle geometry to a severely degraded geometry and
2. The response of the severely damaged fuel to reintroduction of coolant from the emergency core cooling system (ECCS), especially the questions of redistribution of quenched material, short-term cooldown, increased steam generation, and oxidation reaction kinetics.

6.2.1 Test Planning, Review, and Analysis

The safety analysis for the DF experiment plan has been completed. Calculations include several two-dimensional heat transfer calculations to determine the maximum posttest heat load on the test section jacket and the containment tube. Very conservative assumptions were made regarding fuel and component temperatures, fuel relocation, and shroud penetration. These conservation calculations provide bounding values for the posttest temperatures of the jacket and the containment tube. Detailed stress calculations for the capsule were also completed and were included in the experiment plan. Project personnel have begun reviewing the experiment plan with the ACRR safety committee. Although the DFR experiments involve a relatively low number of fissions ( $\sim 10^{17}$ ), the containment and control features required in these experiments present some additional considerations. To allow steam inlet to the rod bundle, a series of check and solenoid valves has been used in the inlet to the experiment package. These valves are closed in the event of reverse flow to provide an "active" containment boundary. The safety committee expressed concern over the use of an active containment boundary because it is a modified approach to experiment containment. Experimenters and safety committee members have begun discussions to arrive at a mutually acceptable containment philosophy. The safety committee is also reviewing proposed test plans for checking reliability and leak rates for the isolation valve

trains under experiment condition. The DFR experiments will also rely on microprocessor control and data retrieval and display. The safety committee has requested unprocessed safety data for ACRR operations. The project group has agreed to provide this data.

The DFR·MOD5 code is used to predict the thermal/hydraulic behavior of the test section for the DF experiments. The original version of this code did not account for radiant heat losses out the top and bottom of the test section. The most recent version of the code allows for these radiant heat losses. The new version of the code was used to perform calculations for experiment DF-1. Improved view factors were also incorporated in these calculations. The improved calculation predicts a slower heatup (1 min slower) and cooler temperatures at the exit of the test section.

Project personnel have written another version of the DFR·MOD code that will calculate the thermal/hydraulic behavior of the entire steam system (boiler, superheaters, CuO tubes, condenser, etc., as well as the test section). The code will also account for heating of the CuO bed from the exothermic reaction of  $H_2$  and CuO.

#### 6.2.2 In-Pile Experiment Apparatus

The DF experiment capsule will be purged of noncondensables (air) just before initiation of the experiment. Heating will be required to drive off adsorbed noncondensables from the CuO bed and  $ZrO_2$  fiber. This approach also requires that the capsule be vented during the preliminary heating stage, then sealed just before or during experiment operation. At present, only the CuO bed can be electrically heated. With the present design, low-power nuclear heating will be required to heat the  $ZrO_2$  fiber. Venting during low-power nuclear operation, up to 773 K (500°C), has been planned. At 773 K (500°C), the purge line will be sealed. A conservative calculation has shown that the maximum activity that could be released (assuming clad failure at this point is <10 millicuries). An analysis has also shown that the pressure required to cause fuel rod failure at 773 K (500°C) is greater than three times the maximum possible rod pressure at 773 K (500°C).

Project personnel have proposed electric heaters as an alternative to nuclear heating. Two-dimensional heat transfer calculations were performed to determine the feasibility of electrically heating the  $ZrO_2$  shroud. The analysis suggests that electrically heating the shroud could reduce or eliminate the need for nuclear heating during the early (purging) phase of the test.

Fabrication of many of the in-pile components has been completed and proof testing of these components has begun. The

design of a noncondensable dome for the in-pile capsule is underway. Several sources for small pumps capable of pumping noncondensables from the condensate tank to the dome under worst conditions have been identified and pumps ordered.

Plumbing of the in-pile skid is near completion. Almost all of the in-pile miscellaneous hardware (pumps, heaters, valves, etc.) has arrived and inventory of all DF-1 hardware has begun.

### 6.2.3 Out-of-Pile Systems Tests (OPST)

#### a. Simplified Tests

The first full-scale out-of-pile steam system test has been successfully completed. The system included a simplified test section, CuO getter tube, condenser, condensate tank, and Raman diagnostic system. No fuel rod simulators were included for this test. Steam conditions typical of in-pile test requirements were attained with flow rates of approximately 1 g/s.

At intervals, during the test, H<sub>2</sub> was mixed with the steam to test the Raman diagnostic system and the CuO getter. All systems performed as expected and confirmed the basic system approach. The CuO and condenser components appear to be very efficient. Preliminary system testing indicates that operational procedures will be required to eliminate potential noncondensables from the steam system during system startup. These potential noncondensables include air entrained in the boiler water, the CuO, and ZrO<sub>2</sub> insulation.

#### b. Electrically Heated Tests

Fabrication and proof testing of all components for the electrically-heated rod simulator tests has been completed. Assembly of the major components is near completion. Tests with this system will be almost identical to those used in the in-pile system. The shrouds, TCs, thermal-limit monitors, CuO bed configuration, condenser, steam injection, and mixing tube are in the same configuration as in the in-pile system. Fuel rods for this first test (OPST-1) will be simulated by four 3/4-inch-I.D. zircaloy-4 tubes with internal tungsten heaters.

Several small modifications to the hardware and assembly procedures were made for the OPST. These changes will also be incorporated in the in-pile capsule design. If OPST-1 suggests significant changes, a second OPST will be performed before the in-pile experiment DF-1.

The self-adjusting pressure regulators for the hot steam lines entering the condenser were tested. Although the regulators do maintain a constant pressure drop as the flow rate is varied (as designed), the regulators are very sensitive to

perturbations; transients can induce flow oscillations. Electrically adjusted valves have been proposed as an alternative to the self-adjusting regulators. The design and fabrication of the electrically adjusted orifices (valves) is straightforward and should have only minor effects on the present schedule. The design of the electrically controlled orifices is underway.

#### 6.2.4 Instrumentation

The out-of-pile tests, described above, were also used to determine the sensitivity limits of Raman spectroscopy for the measurement of hydrogen in steam. The geometry for these tests is similar to the in-pile experiments. Raman measurements were made at a distance of 12 m using the same components that will be used for the in-pile experiments. These first test results showed that a 5% mixture of hydrogen in steam could be measured at a system pressure of 500 torr. Simple system improvements should result in a measurement capability of 1%, or less, for H<sub>2</sub> in steam.

Essentially all of the DF-1 instrumentation has arrived. All of the hardware for the ZrO<sub>2</sub>-sheathed wire TCs has arrived. The SS430 TC body will be brazed to the ZrO<sub>2</sub> sheath by Sandia.

Most of the optical design has been completed. All major components needed for the visual diagnostics for the first in-pile experiment are either on order or have arrived. Some subsystem-level testing of the film camera systems has begun. The remainder of the optical components should be received by the next quarter, and a total system test will be performed at that time. A series of measurements over the temperature range of 1273 K to 2673 K (1000° to 2400°C) has been made using a calibrated blackbody source to determine the accuracy of multiband film radiometry over this temperature range. Several films have been used and results are being evaluated to choose a film for the first in-pile experiment.

In order to insure safety margins on pressure and containment structures, fuel temperatures during the DF experiments must be limited to some maximum allowed value. TCs may be unreliable safety monitors since they will be located in the very high temperature, corrosive environment of the flow volume, and may not survive. Optical pyrometry could be used to obtain high-temperature data in this environment; however, considerable time is required to unfold the temperature data accurately. Because of these limitations, a simple thermal-limit monitor has been designed for these experiments. The safety monitor consists of platinum wires strung axially within the ZrO<sub>2</sub> fiber insulation. The radial location within the insulation will be selected (based on calibration tests that determine the temperature gradient through the insulation) such that the wires will melt when the fuel temperature



limit has been reached. Electrical continuity in the platinum wires will be monitored. A loss of electrical continuity will indicate that the thermal limits have been reached, and the experiment will be terminated. These thermal monitors will also provide an indication of significant shroud penetration.

### 6.3 LIGHT WATER REACTOR (LWR) DEGRADED-CORE COOLABILITY PROGRAM

(K. R. Boldt, 6421; E. G. Bergeron, 6425)

The LWR Degraded-Core Coolability (DCC) program investigates the coolability of uranium debris in water. The uranium is fission-heated in the ACRR to simulate the decay heat expected in an LWR severe core-damage accident. The governing phenomenological uncertainties to be investigated are pressure effects, deep bed behavior, particle size distributions, stratified beds, bottom coolant feed, and material effects. Each DCC experiment will determine coolability in three thermal regimes: (1) convection boiling, (2) dryout, and (3) extended dryout. The staff will use experimental results to confirm and/or modify the present analytical models used to predict degraded-core coolability. Work is proceeding on two in-pile experiments, DCC-1 and DCC-2.

#### 6.3.1 DCC Experimental Activity

During the reporting period, the DCC program effort focused on the following activities:

- a. Preliminary assembly of some DCC-1 hardware was performed, including the crucible, electric heater, primary passthroughs, and TCs. The final experiment assembly was not started because of the delay in receiving the uranium fuel.
- b. The DCC-1 experiment plan was completed and reviewed by the Sandia Reactor Safety Committee. Because DCC-1 contains the most thermal energy and mechanical potential of any experiment performed in the ACRR, the safety analysis in the plan is based on adiabatic energy balances during all credible accident scenarios. The review process concentrated on showing that the assumptions used in this analysis were conservative.
- c. A destructive test of an identical (stress equivalent) vessel to the DCC primary containment was performed. The D-test vessel ruptured at 17,700 psi in a hydrostatic test. The test demonstrated that the 3000-psi pressure rating of the primary containment has a safety factor of at least 4 to rupture.

Each of these activities is detailed in the following discussion.

##### 6.3.1.1 Preliminary Assembly of DCC-1 Hardware

The DCC-1 crucible is a double-walled insulated, cylindrical vessel that supports the debris bed and provides a near-adiabatic condition at the walls and bottom. The crucible was assembled by placing preformed Min-K insulation around

the inner wall and sliding the outer wall over the insulation. The crucible was then closed with a class-I weld of the two Inconel-625 cylinders. The assembled unit was proof-tested to 4400 psi and leak-tested at 1000 psi. The electric heater for DCC-1 was also assembled and proof-tested. The 4-kW (240-V, 17-A) cartridge heater was assembled into an Inconel-625 tube and welded closed. In addition to a proof and leak test, the heater underwent performance testing to insure maximum power capability.

The primary TC assemblies (seven units with eight TCs per unit) were received. The leads from each TC were extended using stainless-steel crimps to attach the new leads. Some problems were encountered because of resistance variations at the point of the crimp. These were resolved by recrimping and stabilizing the connection in a tie-down shell. Following successful performance testing at temperature, the TC assemblies were placed into the primary containment bulkhead and the TCs were bent into position. Figure 6.3-1 shows the TC locations in and around the debris bed. The 39 TCs in the bed were positioned both axially and radially. As specified by the location identifiers in Figure 6.3-1, the bed TCs are designated by levels 00 through 20 (corresponding approximately to inches) and by radial positions as follows:

Table 6-I

Bed Thermocouple Locations for DCC-1

<u>Designator</u>	<u>Distance from Bed Centerline</u>
C (center)	0.0 cm
M (middle)	2.0 cm
S (side)	4.0 cm
X	4.0 cm
Y	4.0 cm
Z	4.0 cm

Ten TCs around the crucible will be used to monitor crucible heat losses, water pool temperature and primary vessel temperatures. Five additional TCs not shown in the figure will monitor the water bath temperatures, heater temperature, and steam temperatures.

#### 6.3.1.2 DCC-1 Experiment Plan

The DCC-1 experiment plan was completed and the review by the ACRR safety committee was started. Because of its size (a 30-kg urania bed contained in 500-kg pressure vessels), the DCC-1 package will have the most thermal energy (~90 MJ) of any experiment performed in the ACRR.

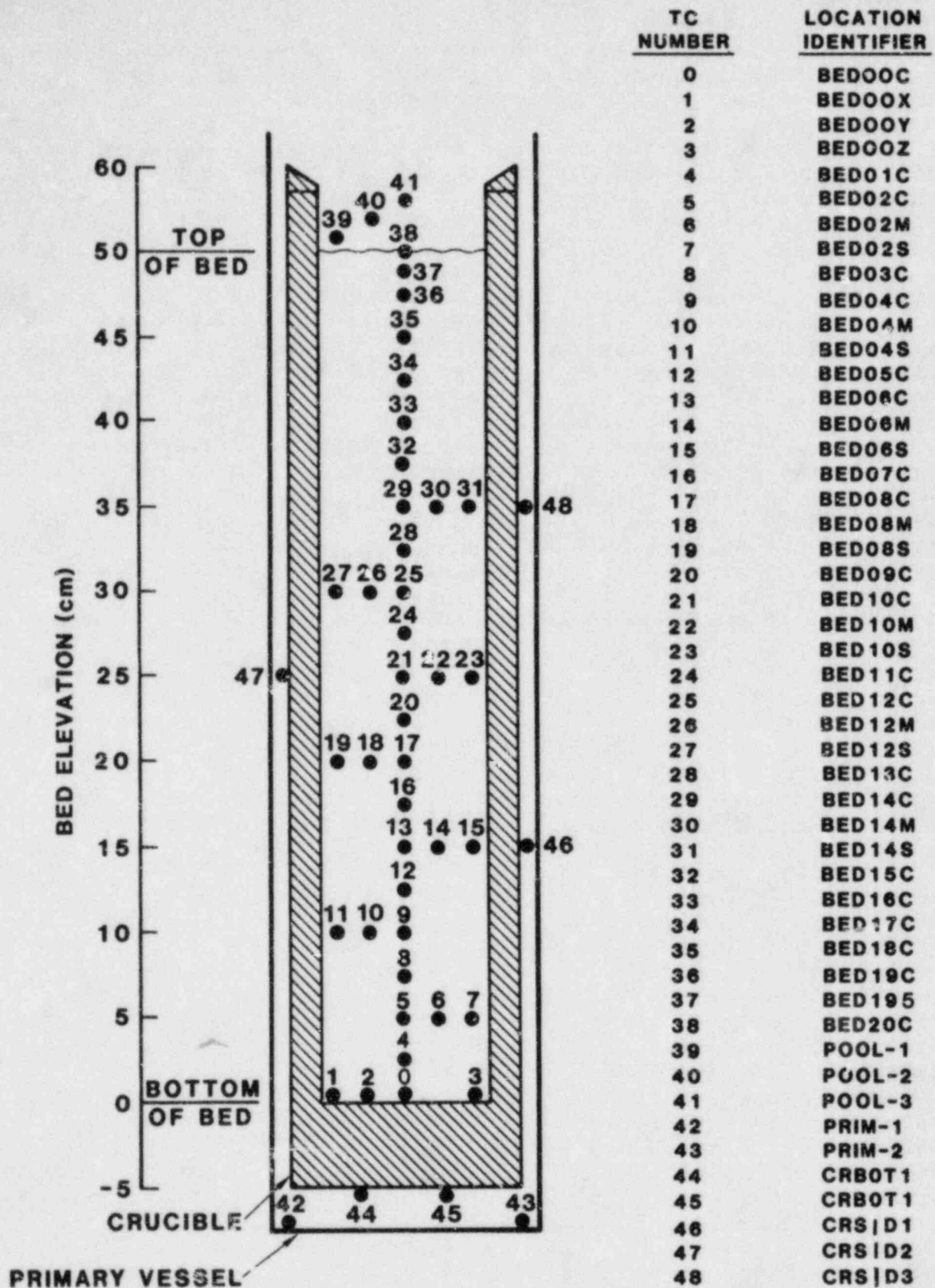


Figure 6.3-1. DCC-1 Thermocouple Locations

About 15 MJ of this total is internal energy in the pressurized water bath and therefore can be converted into mechanical work. For these reasons, the accident analysis in the DCC-1 experiment plan presents a thorough evaluation of the containment integrity for all credible (single-failure) accidents with conservative assumptions. The credible occurrences analyzed are:

1. Excessively high bed temperatures
2. Bed disturbances
3. Crucible failure
4. Loss of cooling capability
5. Primary containment failure
6. Secondary containment failure
7. Hydrogen generation

All of these occurrences have been analyzed and used to determine design parameters, operating limits, and/or instrumentation specifications. The failure used as the design basis for the primary containment is the loss of cooling capability. For the secondary containment, the design basis is the failure of the primary containment. Since these two occurrences represent the most significant hazards for the DCC-1 experiment, they are summarized here.

The loss of cooling accident for the DCC-1 experiment assumes the following conditions exist at the time of occurrence:

1. The water/steam bath, primary containment, and secondary containment are all at saturation temperature and pressure up to the shutdown value of 2700 psi.
2. Half of the debris bed is dried out and at 1073 K (800°C).
3. A loss of cooling occurs and the package is allowed to adiabatically attain an equilibrium temperature and pressure.

Figure 6.3-2 shows the internal energy of the primary system as a function of pressure. With half of the bed dried at 1073 K (800°C), the energy available above 643 K (370°C) is 1.7 MJ. In case of loss of coolant capability, the reactor would be shut down and the energy assumed to adiabatically heat up the package. The rate at which this energy becomes available to pressurize the system is determined by the quench rate. The rate of quench is one of the parameters to be investigated in the experiment. Current models predict the rate of quench to be on the order of the dryout power. Therefore, the quench is predicted to take at least 700 s. With this much time, it can be assumed that the heat not only increases the bath temperature, but also heats up the entire primary system (vessel, bulkhead, crucible). As shown in Figure 6.3-2, the resultant

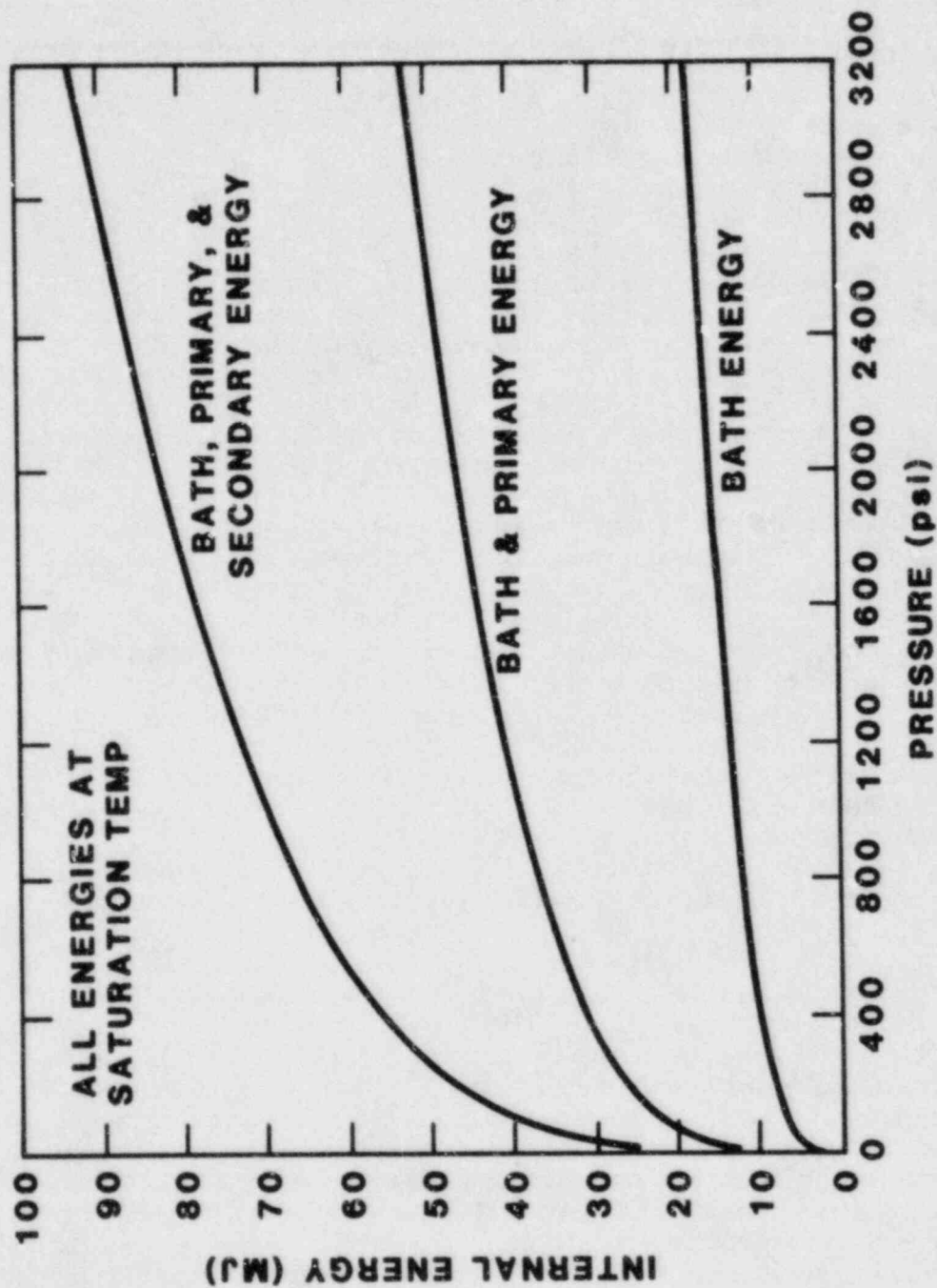


Figure 6.3-2. Internal Energy of the DCC-1 Primary System

pressure rise starting from the shutdown pressure of 2700 psi would be ~300 psi. If assumed that the heat is also conducted to the secondary, the pressure rise would be much less. Based on this conservative analysis, a maximum allowable working pressure (MAWP) of 3000 psi at 643 K (370°C) is established for the primary containment.

The primary containment failure serves as the design basis for establishing the MAWP for the secondary containment system. Adopting the approach that all single failures are credible, the following failures are considered as failures of the primary containment integrity:

1. Failure of the upper bulkhead weld
2. Failure of the vessel wall
3. Failure of the lower closure weld
4. Ejection of the passthrough or pressure transducer
5. Slow leakage

None of the credible single failures has been identified that will fail the secondary containment.

The primary containment MAWP is 3000 psi at 643 K (370°C). The vessel, bulkhead, and passthroughs will be tested to 2 x MAWP for yielding and 4 x MAWP for rupture. If a failure is assumed to occur in the primary boundary, it is difficult to determine which mode and location of failure would be most likely since all development and proof tests show integrity well above 4 x MAWP.

If the upper bulkhead were to fail (such as occurred at the weld in the D-test at >4 x MAWP), the secondary volume above the bulkhead would be immediately pressurized. Although the volume being pressurized increases considerably (23.5 to 30.5 l), the pressure does not decrease proportionately. This is due to the fact that the main portion of the energy in the primary system is contained in the liquid. During the blowdown, a small amount of liquid is flashed to steam and a new saturation point is obtained. Figure 6.3-3 shows the calculated total (liquid and vapor at saturation) internal energies for the primary and secondary volumes assuming a liquid mass of 9.5 kg. With the primary system operating 2500 psi, the internal energy is 16.6 MJ. An adiabatic blowdown would adjust rapidly to a new saturation point with the secondary volume included, which in turn would reduce the pressure to 2200 psi. Therefore, the secondary containment MAWP is established as 2200 psi at 643 K (370°C).

#### 6.3.1.3 Destructive Test

Based on the previous accident analyses, the DCC-1 containment vessels were designed, built, and tested to be consistent with the specified MAWP values. Three tests completed on the vessels during the quarter were proof tests to at least

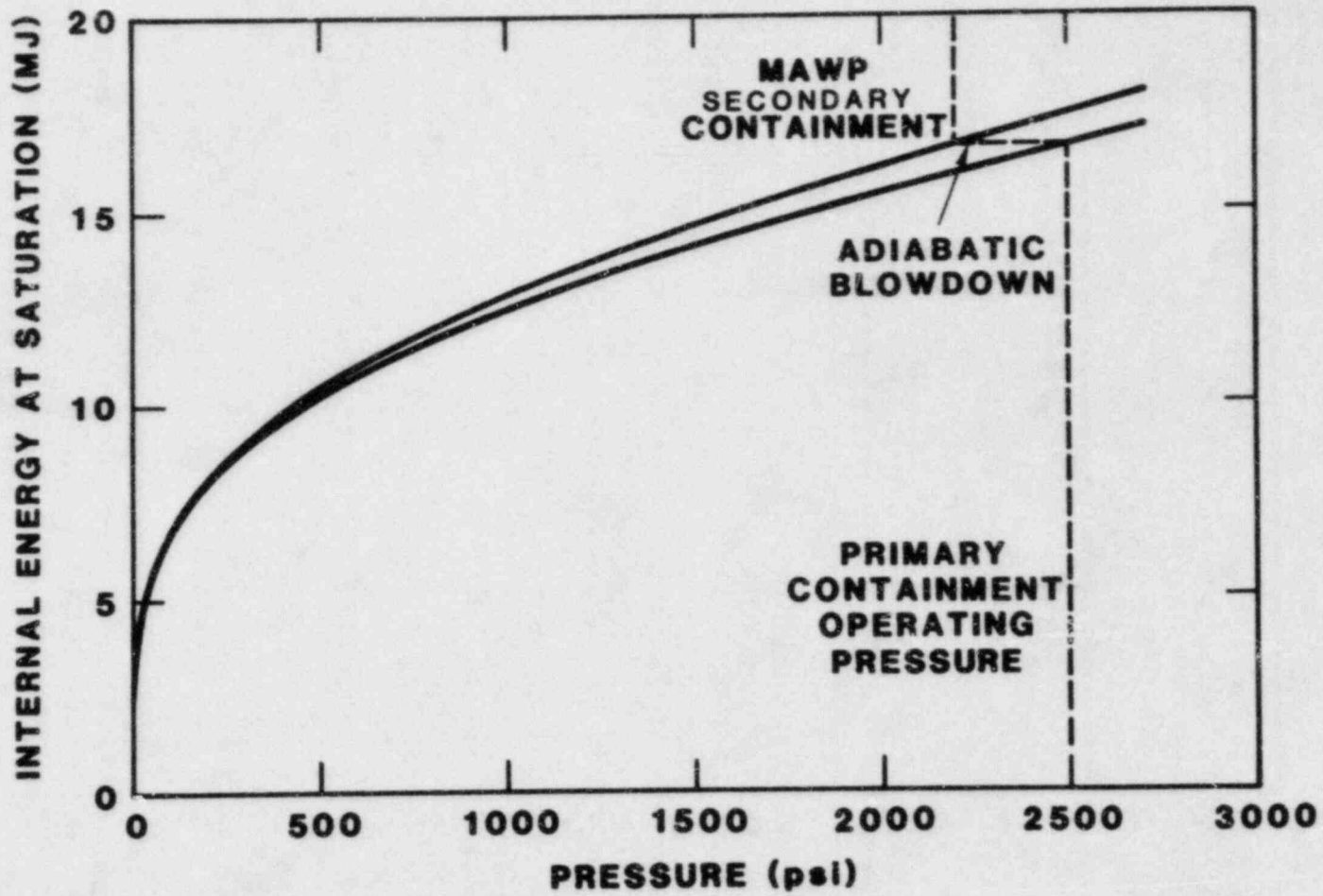


Figure 6.3-3. Primary and Secondary Internal Energies during Adiabatic Blowdown



2 x MAWP for each vessel, primary and secondary, and a destructive test of a nearly identical vessel as the primary containment. In order to insure that the primary vessel could be operated to 3000 psi at 643 K (370°C), the D-test vessel had to survive at least 4 x MAWP. With temperature correction, the required hydrostatic rupture pressure was increased to 13,800 psi. The D-test was terminated when the vessel ruptured at 17,700 psi due to a failure of one of the welds of the closure bulkhead. The Inconel-625 vessel fully demonstrated the characteristics expected from this material (high strength and ductility). The D-test was successful and confirmed the method and properties used in the design stress analysis.

### 6.3.2 Analysis of the DCC Program

#### 6.3.2.1 Momentum Flow Equations

Generalized momentum flow equations for separated two-phase flow through porous media were derived for use in MELPROG. These equations should provide a basis for a numerical treatment of debris beds whenever debris characterization is not handled in a separate module.

In one dimension, momentum equations become  
for the gas:

$$\alpha_g \rho_g \left[ \frac{\partial v_g}{\partial t} + v_g \frac{\partial v_g}{\partial x} \right] = -\alpha_g \frac{dP}{dx} - \sum (f_{gl} + f_{gs}) - \alpha_g \rho_g G, \quad (6.1)$$

for the liquid:

$$\alpha_l \rho_l \left[ \frac{\partial v_l}{\partial t} + v_l \frac{\partial v_l}{\partial x} \right] = -\alpha_l \frac{dP}{dx} - \sum (f_{lg} + f_{ls}) - \alpha_l \rho_l G, \quad (6.2)$$

and for the solid particles:

$$\alpha_s \rho_s \left[ \frac{\partial v_s}{\partial t} + v_s \frac{\partial v_s}{\partial x} \right] = -\alpha_s \frac{dP}{dx} - \sum (f_{sg} + f_{sl} + f_{ss}) - \alpha_s \rho_s G. \quad (6.3)$$

The number of force terms appearing in Eq. 6.1 through 6.3 can be reduced by observing that

$$f_{gl} = -f_{lg}$$

$$f_{ls} = -f_{sl}$$

and

$$f_{gs} = -f_{sg} .$$

It has been experimentally determined that during steady-state, concurrent two-phase flow through a porous medium, the pressure drops in the liquid and gaseous phases are given, in one dimension, by

$$\frac{dP_l}{dx} = - \frac{\mu_l u_l}{K K_l(s)} - \frac{\rho_l u_l |u_l|}{\eta \eta_l(s)} , \quad (6.4)$$

$$\frac{dP_g}{dx} = - \frac{\mu_g u_g}{K K_g(s)} - \frac{\rho_g u_g |u_g|}{\eta \eta_g(s)} , \quad (6.5)$$

where the pressure in the liquid is related to the pressure in the gas by

$$P_g = P_l + F(s) \equiv P_l + \frac{\sqrt{150}\sigma(1-\epsilon)(s^{-1}-1)^{.175}}{\sqrt{5}\epsilon d} \quad (6.6)$$

It seems a good assumption that the pressure in the liquid is equal to the pressure in the solid (the bed particulate), since they are in contact in the steady-state situations for which these equations were derived and because this is the case when only liquid is present. Thus,

$$P_s = P_l , \quad (6.7)$$

where  $P_s$  is the pressure in the solid.  $u_g$  and  $u_l$  are the superficial velocities of the gas and liquid and are related to the microscopic velocities that appear in Eq. 6.1 through 6.3 by

$$u_g = \varepsilon(1 - s)v_g = \alpha_g v_g \quad (6.8)$$

and

$$u_l = \varepsilon s v_l = \alpha_l v_l \quad (6.9)$$

One can equate  $P$ , appearing in Eq. 6.1 through 6.3 with  $P_l$  and compare Eq. 6.1 through 6.3 for steady-state flow with Eq. 6.4 through 6.7 to arrive at the following relationships for the exchange forces, the  $f$ 's:

$$f_{lg} + f_{ls} = \alpha_l \frac{\mu_l u_l}{K K_l} + \alpha_l \frac{\rho_l u_l |u_l|}{\eta \eta_l} \quad (6.10)$$

$$f_{gl} + f_{gs} = \alpha_g \frac{\mu_g u_g}{K K_g} + \alpha_g \frac{\rho_g u_g |u_g|}{\eta \eta_g} + \alpha_g \frac{dF}{dx} \quad (6.11)$$

$$\alpha_s (f_{lg} + f_{ls}) = \alpha_l (f_{sg} + f_{sl} + f_{ss}) \quad (6.12)$$

$$\alpha_g (f_{lg} + f_{ls}) = \alpha_l (f_{gl} + f_{gs}) \quad (6.13)$$

From Eq. 6.10 through 6.13, it can be shown, first, that  $f_{sg}$  and  $f_{sl}$  cannot be separated.  $f_{lg}$  would be known from

$$f_{lg} = \frac{-\alpha_l f_{sg} + \alpha_g f_{sl}}{\alpha_g + \alpha_l} \quad (6.14)$$

which is the consequence of Eq. 6.13. Second, it can be shown that

$$\begin{aligned} f_{sg} + f_{sl} &= -(1 - \alpha_s) \left( \frac{\mu_l u_l}{K K_l} - (1 - \alpha_s) \frac{\rho_l u_l |u_l|}{\eta \eta_l} \right) \\ &= -(1 - \alpha_s) \left[ \frac{\mu_g u_g}{K K_g} + \frac{\rho_g u_g |u_g|}{\eta \eta_g} + \frac{dF}{dx} \right] \quad (6.15) \end{aligned}$$

Finally, it can be shown that

$$f_{sg} + f_{sl} + f_{ss} = - \frac{\alpha_s}{1-\alpha_s} (f_{sg} + f_{sl}) . \quad (6.16)$$

Thus, the separated flow momentum equations used for steady-state debris bed modeling, which neglect terms due to condensation and evaporation of gas and liquid, are given:

for the gas:

$$0 = -\alpha_g \frac{dP}{dx} - \alpha_g \frac{\mu_g u_g}{K K_g} - \alpha_g \frac{\rho_g u_g |u_g|}{\eta \eta_g} - \alpha_g \rho_g G - \alpha_g \frac{dF(s)}{dx} , \quad (6.17)$$

for the liquid:

$$0 = -\alpha_l \frac{dP}{dx} - \alpha_l \frac{\mu_l u_l}{K K_l} - \alpha_l \frac{\rho_l u_l |u_l|}{\eta \eta_l} - \alpha_l \rho_l G , \quad (6.18)$$

and for the solid:

$$0 = -\alpha_s \frac{dP}{dx} - \alpha_s \frac{\mu_l u_l}{K K_l} - \alpha_s \frac{\rho_l u_l |u_l|}{\eta \eta_l} - \alpha_s \rho_s G . \quad (6.19)$$

In the case of a nonfluidized bed, the steady-state equation for the particulate is given by Eq. 6.19. The condition for fluidization of the bed is that the force between particles,  $f_{ss}$ , must be equal to zero. Using Eq. 6.15 in the steady state and Eq. 6.3, a steady-state equation for the particulate can be formulated to test for this condition.

Equations 6.10, 6.11, and 6.16 can be used to formulate the one-dimensional non-steady-state momentum equations for separated flow of liquid, gas, and particulate. For a non-fluidized bed, the proper momentum equations are:

for the gas:

$$\alpha_g \rho_g \left[ \frac{\partial v_g}{\partial t} + v_g \frac{\partial v_g}{\partial x} \right] = -\alpha_g \frac{dP}{dx} - \alpha_g^2 \frac{\mu_g v_g}{K K_g} - \alpha_g^3 \frac{\rho_g v_g |v_g|}{\eta \eta_g} - \alpha_g \rho_g G - \alpha_g \frac{dF(s)}{dx}, \quad (6.20)$$

for the liquid:

$$\alpha_l \rho_l \left[ \frac{\partial v_l}{\partial t} + v_l \frac{\partial v_l}{\partial x} \right] = -\alpha_l \frac{dP}{dx} - \alpha_l^2 \frac{\mu_l v_l}{K K_l} - \alpha_l^3 \frac{\rho_l v_l |v_l|}{\eta \eta_l} - \alpha_l \rho_l G, \quad (6.21)$$

and for the solid particles:

$$\alpha_s \rho_s \left[ \frac{\partial v_s}{\partial t} + v_s \frac{\partial v_s}{\partial x} \right] = -\alpha_s \frac{dP}{dx} - \alpha_s \alpha_l \frac{\mu_l v_l}{K K_l} - \alpha_s \alpha_l^2 \frac{\rho_l v_l |v_l|}{\eta \eta_l} - \alpha_s \rho_s G. \quad (6.22)$$

The momentum exchange terms due to evaporation and condensation of liquid and gas have been neglected from these equations but can be added in the obvious manner.

The notation for Eq. 6.1 through 6.22 is:

$\alpha_g$  = volume fraction of gas, equal to  $\epsilon(1 - s)$

$\alpha_l$  = volume fraction of liquid, equal to  $\epsilon s$

$\alpha_s$  = volume fraction of the solid particles, equal to  $(1 - \epsilon)$

$\rho_l$  = density of the liquid

$\rho_g$  = density of the gas

$\rho_s$  = density of the solid

$\epsilon$  = bed porosity

$v_g$  = local velocity of the gas

$v_l$  = local velocity of the liquid

$v_s$  = local velocity of the solid

$P$  = ambient pressure

$G$  = gravitational constant

$s$  = liquid volume fraction (within the porous volume)

$K_l$  = liquid laminar relative permeability, equal to  $s^3$

$K_g$  = vapor laminar relative permeability, equal to  $(1 - s)^3$

$\eta_l$  = turbulent liquid relative permeability, equal to  $s^5$

$\eta_g$  = turbulent vapor relative permeability, equal to  $(1 - s)^5$

$f_{ij}$  = force on material  $i$  due to material  $j$

$$K = \frac{d^2 \epsilon^3}{150(1 - \epsilon)^2}$$

$$\eta = \frac{d \epsilon^3}{1.75(1 - \epsilon)}$$

#### 6.3.2.2 Experiment Calculations-Thermocouple Placement and Radiolysis of Coolant

Two calculations were performed in support of the experiment planning and safety analyses. In the first, an estimate of the perturbing effect of the 40 TCs used to instrument DCC-1 on the dryout heat flux measurement was made. It was estimated that the effect was important enough to cause an overestimate of the dryout heat flux by a factor of up to 1.08. In the second calculation, an evaluation of the hydrogen production in the capsule due to radiolysis of  $H_2O$  was made and was found to be minimal.

##### a. Thermocouple Placement

During the DCC experiments, the principal bed diagnostic equipment will consist of 40 TCs (63-mil outer diameter), which are introduced into the bed crucible along the inner wall in groups of 4. They will be pressed to the side of the crucible inner wall at the top of the crucible (~1 in. above the bed) using a clamp as shown in Figure 6.3-4.

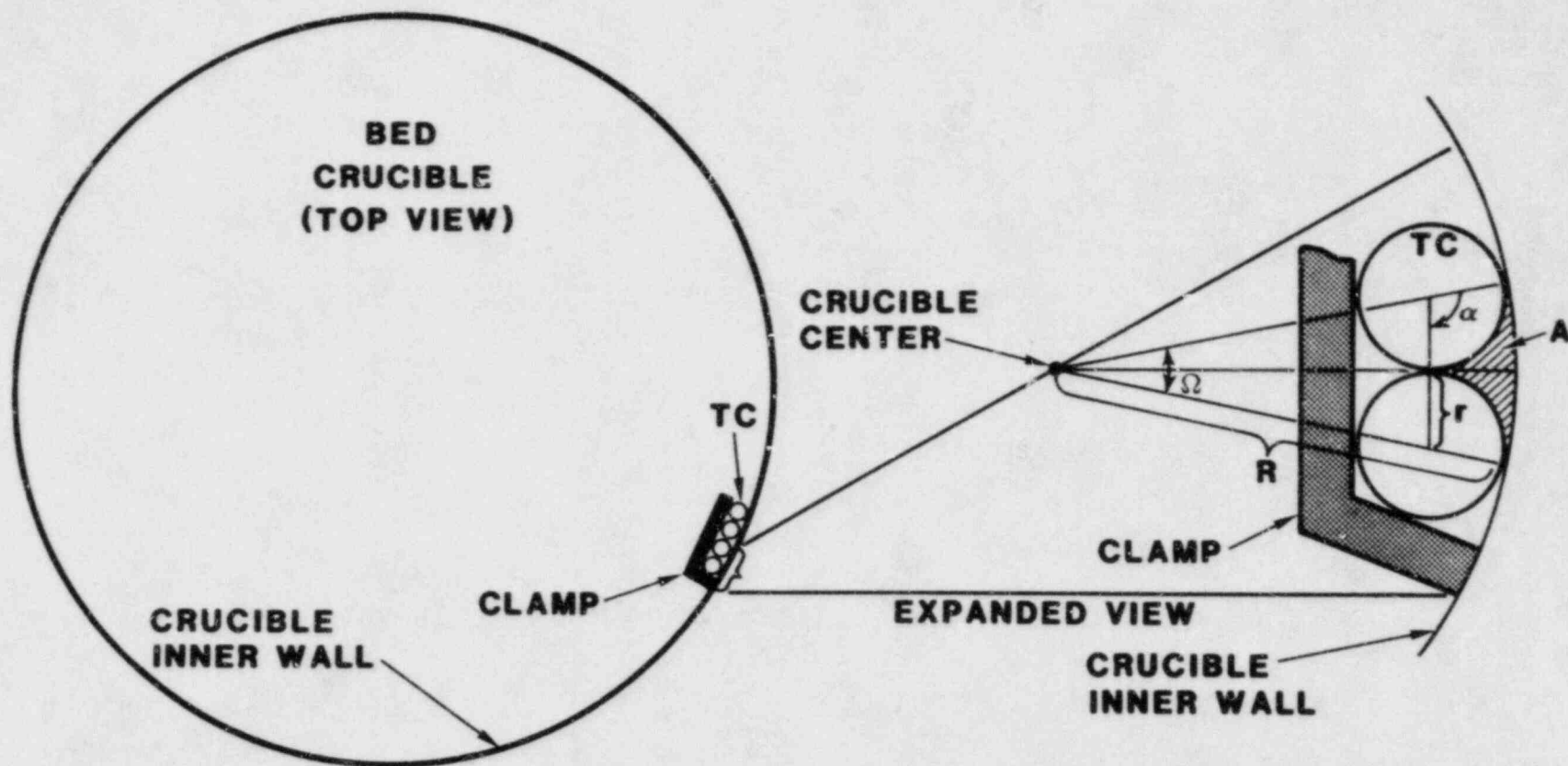


Figure 6.3-4. Schematic of the Bed Crucible Showing the Placement of the Thermocouples and the Flow Passageways

Tiny passageways for liquid or vapor flow are formed between the TCs and the wall and allow escape of vapor from the bed. Although not all of the passageways extend to the bed bottom, all of them exist at the bed top, where the greatest amount of vapor must escape from the bed and where the vapor flow restriction that determines the coolability limit of the bed exists.

The cross-sectional area of a single passageways is given by

$$A = \pi R^2 \left( \frac{\Omega}{2\pi} \right) - \pi r^2 \left( \frac{2\alpha}{2\pi} \right) - r(R - r) \cos\left(\frac{\Omega}{2}\right), \quad (6.23)$$

where

$$\alpha = \frac{\pi}{2} + \frac{\Omega}{2}, \text{ and } \sin\frac{\Omega}{2} = \frac{r}{R - r}. \quad (6.24)$$

For the DCC test geometry  $R = 0.0508$  m and  $r = 1.59 \times 10^{-3}$  m, yielding  $A = 2.8 \times 10^{-7}$  m<sup>2</sup>, whereas the total cross-sectional area of the bed,  $A_{\text{crucible}}$ , is  $8.11 \times 10^{-3}$  m<sup>2</sup> ( $\pi R^2$ ).

Since the restriction on the coolability of the bed is the restriction to vapor flow from the bed, the coolability would be increased the most if the passageways behind the TCs contained all vapor. Assuming this to be the case, the ratio of the mass flux of vapor through the passageways to the mass flux through the bed will be given by the ratios of the superficial vapor velocities times the cross-sectional areas of these parts, given the same differential pressure drop with elevation. The superficial velocity of the vapor through the bed close to dryout is given by

$$v_{\text{bed}} = \left( \frac{d^2 \epsilon^3}{150(1 - \epsilon)^2 \mu_v (1 - s)^3} \right) \left( \frac{dP}{dz} \right) \quad (6.25)$$

and through the passageways

$$v_{\text{sides}} = \left( \frac{D^2}{32 \mu_v} \right) \left( \frac{dP}{dz} \right) \times 35, \quad (6.26)$$



where  $d$  is the effective diameter for the particle bed (0.0004 m for DCC-1),  $\epsilon$  is the bed porosity (about 0.34 for DCC-1), and  $\mu$  is the vapor dynamic viscosity ( $1.21 \times 10^{-5}$  ns/m<sup>2</sup> at 1 bar;  $2.2 \times 10^{-5}$  ns/m<sup>2</sup> at 170 bar),  $s$  is the bed saturation (equal to

$$s = \frac{1}{1 + \left[ \frac{\mu_v \rho_l}{\mu_l \rho_v} \right]^{1/4}} \quad (6.27)$$

at dryout),  $\mu_l$  is the dynamic viscosity of the liquid ( $2.79 \times 10^{-4}$  ns/m<sup>2</sup> at 1 bar,  $7 \times 10^{-5}$  ns/m<sup>2</sup> at 170 bars),  $\rho_v$  and  $\rho_l$  are the vapor and liquid densities (0.6 and 960 kg/m<sup>3</sup>, respectively, at 1 bar and 119 and 566 kg/m<sup>3</sup> at 170 bars),  $D$  is the hydraulic diameter of the triangular-shaped passageways ( $\pi D^2/4 = A$ ),  $P$  is ambient pressure, and  $z$  is elevation in the bed. The expression for  $v_{\text{sides}}$  is multiplied by 35 to take into account the separate passageways. Then, the ratio of the vapor mass flux through the passageways to the mass flux through the bed is given by

$$\text{ratio} = \frac{150D^2(1-\epsilon)^2(1-s)^3}{32d^2\epsilon^3} \times 35 \frac{A}{A_{\text{crucible}}} \quad (6.28)$$

This is equal to 0.076 at 1 bar and 0.028 at 170 bars. Since the vapor flux from the bed at dryout is proportional to the true dryout heat flux, the heat flux that will be measured in the DCC-1 will be 1.08 times the dryout heat flux at 1 bar and 1.03 times the dryout heat flux at 170 bars.

Putting tiny wires into the passageways between the TCs and the crucible wall will reduce the flow in the passageways drastically and virtually eliminate this source of error in measuring the dryout heat flux. These wires need to be installed only in the top few inches of the bed in order to block flow through the passageways.

Finally, the use of an equivalent hydraulic diameter in calculating the flow through the triangular passageways represents an overestimate of the flow velocity and thus an overestimate of the error produced in the measurement of the dryout heat flux.[6-1]

#### b. Radiolysis of Coolant

The radiolysis of water or steam by fast neutrons to produce H<sub>2</sub> gas is not completely understood.[62] However,

limited experimental studies permit assignment of upper limits to the quantity that can be produced.

Generally, during exposure to ionizing radiation, certain radicals are formed from the water molecules and the molecules of other impurities present in solution or in close contact with the water. If the water is relatively pure, as is the case in the DCC experiments, the radicals will recombine to form molecules, the two gaseous products being  $H_2$  and  $O_2$ . Since  $H_2$  and  $O_2$  will, in turn, recombine to form  $H_2O$  during steady-state irradiation, a steady concentration of  $H_2$  and  $O_2$  will be set up. The size of the concentration will depend on the creation rate of radicals, the recombination mechanisms for radicals, the recombination rate of  $H_2$  and  $O_2$ , all of which depend on the type of radiation, the quality (vapor fraction) of the fluid, and the presence of impurities in solution with the fluid.

If reducing agents are present in the water, the  $O_2$  can be eliminated from solution in the water or steam and the recombination of  $H_2$  with  $O_2$  cannot occur. In this case, under steady irradiation, the amount of  $H_2$  generated will not reach a steady concentration in the water but will increase indefinitely.

A review of the potential for oxidation reactions to occur in the DCC experiments has concluded that at low temperatures (625 K [352°C]), there is little possibility of such reactions. It is assumed that some unexpected material is present in the water, which combines with all the  $O_2$  produced from radiolysis, and that the  $H_2$  concentrations will increase steadily throughout the experiment.

The rate of increase of  $H_2$  can be obtained using estimates of the G value (the number of molecules of  $H_2$  produced per 100 eV of absorbed energy). Since the absorbed energy per unit irradiated volume is much greater for pure water than for steam, it will be assumed that the amount of  $H_2$  produced is the same as if the entire volume of the DCC capsule, except for the space occupied by the particles of the debris bed, contained water. Under conditions similar to those found in the upper plenum (above the bed) in the DCC experiments, G has been measured to be 0.6 for pure water at 373 K (100°C). In the bed, it is recommended that a value of 1 be used for G at temperatures below 423 K (150°C) and a value of 2 be used above 423 K (150°C), as a conservative estimate. The irradiated volume occupied by water above the bed is about  $5 \times 10^3$  cm<sup>3</sup>. The rate of production of hydrogen gas is then given:[6-3]

$$R(\text{cm}^3/\text{s}) = 3.74 \times 10^{-22} \text{ E M G} , \quad (6.29)$$

where E is the energy deposition per gram of water (eV/s/g) and M is the mass of water present (g). In Reference 6-3, it is recommended that for a fast neutron flux of  $>1$  MeV neutrons, E is given by

$$E = 2.3 \times 10^5 \times \text{neutron flux}(\text{n/cm}^2/\text{s}) . \quad (6.30)$$

With E given as in Eq. 6.30, assuming that the reactor power is at 2 MW (the flux of neutrons  $>1$  MeV being approximately  $2 \times 10^{12}$  n/cm<sup>2</sup>/s, and assuming that the water above the crucible sees 1/10 the neutron flux as the water in the bed, R would be less than 0.3 cm<sup>3</sup>/s at all pressures. With the assumption that the energy deposition in the water in the bed is equal to the volumetric proportion of water in the bed times the total power generated in the bed at a power of 1 W/cm<sup>3</sup> and that the water generation in the upper plenum of the test capsule is calculated as above, R would be less than 0.07 cm<sup>3</sup>/s at all pressures.

For 100 hr of operation at 1 MW power (an overestimate), the total quantity of hydrogen gas generated would be equal to 6.4 and 1.5 g, respectively, for the two values of R calculated. If the oxygen generated were not reacted by impurities, then a steady-state value of hydrogen gas concentration would be reached in about 10 hr or less.

At 1 bar steam partial pressure, 12% of the H<sub>2</sub> would be in solution in the water. A hydrogen partial pressure of 30 and 7 bars, respectively, would be produced and would be detectable. At 170 bars steam partial pressure, 85% of the H<sub>2</sub> would be in solution in the water, and hydrogen partial pressures of 23 bars and 5 bars would be produced but might not be detectable. If the reactor power were suddenly cut off, this hydrogen could hypothetically react with O<sub>2</sub>. However, in order to postulate a constant buildup of H<sub>2</sub>, it was assumed that the O<sub>2</sub> is combined with impurities.

If the O<sub>2</sub> had not combined with impurities, a steady-state concentration of H<sub>2</sub> and O<sub>2</sub> of less than 2 cm<sup>3</sup> each per liter of H<sub>2</sub>O present would have been set up. This is equivalent to less than  $8 \times 10^{-4}$  g H<sub>2</sub> for the DCC test capsule at 1 bar steam partial pressure. This amount of H<sub>2</sub> and O<sub>2</sub> could recombine if the reactor power were suddenly turned off, releasing a total of about 110 J energy. At 170 bars, about twice the steady-state concentration of hydrogen would be produced as at 1 bar; however, 85% would be in solution in the liquid. Thus, sudden reactor shutdown and combustion of H<sub>2</sub> would release even less energy than at 1 bar.

### 6.3.2.3 Uncertainties in DCC Coolability Predictions for Accident Analysis

Predictions of the coolability limits of debris beds are being made and applied to LWR reactor accident analyses with increasing accuracy. A systematic evaluation is presented of the accuracy of existing models, the way in which they are currently applied to reactor calculations, and the needs for accident calculations. The purpose is to point out the remaining areas of uncertainty in making coolability predictions. The importance of these uncertainties to overall accident sequence analyses can also be estimated. Areas requiring further study can be identified with potential sources for the required information from existing research programs in the U.S. and Europe.

Significant uncertainties remain in the ability to predict the long-term coolability limits of a degraded reactor core. Most of them are related to the lack of understanding of the conditions within degraded reactor cores, though uncertainties also occur because of untested models. The dryout heat flux is very sensitive to the exact porosity of the bed; however, the porosity can reasonably be expected to vary over a limited range in values. The parameter of most importance in determining the coolability of a particle bed is the effective particle diameter. The dryout heat flux is proportional to the particle diameter in large ( $d_{eff} > 2$  mm) particle beds and the square of particle diameter in small ( $d_{eff} < 2$  mm) particle beds. The effective particle diameter  $d_{eff}$  can reasonably be expected to vary from about 0.1 to about 2 mm or more.

Recent modeling has been successful in predicting the coolability limits of beds of single-size spheres on impermeable supports. Limited success has also been obtained in predicting the coolability of beds of spheres subject to forced liquid flow, uniform mixtures of various-sized spheres or rough particles, and stratified beds for a limited number of experiments and conditions. Finally, a few poorly understood history-dependent phenomena are identified as potential sources of uncertainty. Existing experimental programs are capable of resolving most of these, although emphasis should be placed on systematic investigations of the most important phenomena. These include knowledge of the debris configurations that can exist in LWRs, including possible particle size distributions, shape factors, and stratification. Verification of modeling of the effects of stratification, ambient pressure, and bottom coolant flow is also of importance.

### 6.3.2.4 Analysis of a Traveling Liquid Slug in DCC In-Pile Experiments

Creation of an upward-traveling liquid slug of high kinetic energy within the DCC experiment capsule would require rapid mixing of hot particulate debris from the bed with

coolant and equally rapid vaporization and pressurization of the coolant below the main liquid pool. Figure 6.3-5 shows the essential geometry of the (enclosed) experiment capsule, the debris bed, the overlying liquid pool, and the steam/gas chamber at the top of the capsule. This investigation concludes that hot debris from a dry portion of the DCC experiment cannot become intimately mixed with cool water on a time scale of less than 100s of seconds. In that time scale, pressure equilibration throughout the entire capsule will be maintained, and no large-scale motion of the debris itself or the overlying liquid pool can be induced. Essential evidence for this conclusion is derived from

- a. Experience with debris beds--a large literature field can be quoted that shows that even the most disruptive bed disturbances do not produce sudden heat transfer between hot debris and water, and
- b. Simple calculations using basic properties of debris beds to show why this mixing cannot occur.

Types of bed disturbances known to occur are (1) superheat disturbances and (2) unusual or forced liquid entry into the bed that causes a water hammer-type phenomenon. The first of these occurs in saturated (thus cool) beds. Both are benign phenomena. In addition, type (2) disturbances most generally occur in geometries with bottom forced flow, which is different from the bed and coolant geometry in DCC-1 and DCC-2.

Closed volume (thus pressurized) quench experiments with 1173 K (900°C) stainless-steel particles have been performed. No strange pressurization events occurred. Gradual rewet of the bed occurred in about 600 s.

Rewet of hot debris occurs to some extent in all dryout experiments. It is well known that this occurs very slowly if the bed is very hot. Closed volume debris bed dryout experiments have been performed at Sandia with liquid sodium coolant and debris temperatures of up to 1373 K (1100°C) have been reached. No violent mixing of debris and coolant has occurred.

To force one-half of a hot bed to rewet in the time of 1 s (about the time required to create rapid mixing of hot debris and coolant, a "steam explosion" and a traveling pressure pulse) would in turn require a pressure pulse of 1 s duration of 41,000 psi from above the liquid pool. No mechanism exists for this to happen.

#### a. Disruptive Bed Events

Superheat disturbances have been observed in a number of sodium-debris bed experiments at Sandia.[6-5] Analysis shows

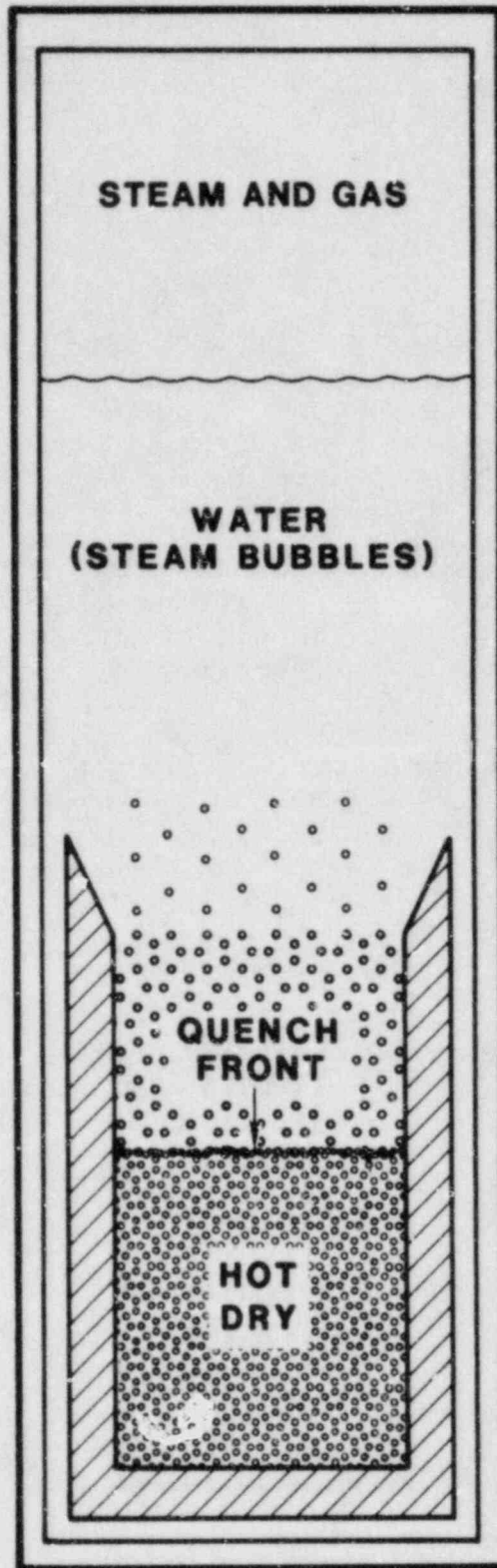


Figure 6.3-5. Schematic of the Experiment Capsule

that superheat disturbances are less likely to occur with water-debris beds and the superheat likely to be attained is much lower than for sodium beds. The most violent superheat disturbance resulted from a superheat of 318 K (45°C) and produced a pressure increase in the capsule of about 5 psi. It was calculated that the bed height was increased, as a result of the disturbance, from about 1.13 to about 1.22 cm. The only direct evidence that superheat disturbances occur in water-debris beds is from Reference 6-6. The superheats observed are about 274 to 275 K (1 to 2°C) and the bed movement small and lasts only about 1 s. This is demonstrated by runs 12 and 14 where the temperature definitely indicates disturbances that were not observed visually. Further, it is stated that for the most pronounced ones, the bed surface lifted shortly (1 s) by about 0.5 cm. After the release of vapor generated by the flashing, the bed height increase in run 8 was <0.2 cm. In order for a bed superheat to occur, the bed must be saturated with liquid. Thus, no mixing of hot debris and coolant can occur. Only brief and small pressure pulses can occur.

An anecdotal account of bed disturbance has been reported in Reference 6-7. Liquid was forced into a hot debris bed from below. When the rate of liquid injection was very large, a pressure buildup and oscillating liquid-vapor interface were observed in the bottom of the bed. In most instances the pressure pulse resulted in fluidization of the upper portion of the bed. Once fluidization occurred, the upper portion of the bed remained fluidized until the lower portion was completely quenched. Since the DCC-1 test has an impermeable bottom, these effects are not expected to occur.

Another account of a bed disturbance due to unusual liquid entry into a hot bed was reported.[6-8] This occurred after dry out when liquid was introduced into the bed by a pathway caused by tilting the bed. The liquid built up until it came into contact with a hot portion of the bed whereupon it flashed to vapor. The escaping vapor fluidized the entire bed. However, the bed did not mix with the overlying liquid pool but remained fluidized by flowing vapor until the vapor escaped.

Also, an account of surging in a saturated bed was offered by Reference 6-8. The phenomenon (a periodic liquid surging) was observed only for the large particle sizes (4783 and 3175  $\mu\text{m}$ ) and with acetone as the coolant. No fluidization phenomenon was mentioned.

#### b. Normal Bed Behavior

To date, approximately a dozen experiments have been conducted over the past 2 yr on quenching of hot particulate debris from above. Two different experimenters were involved. No unusual pressure spikes, bed disturbances, or violent

phenomena have been observed. The debris has been heated to 1173 K (900°C) and quenched by dumping subcooled or saturated water on top of the debris. Beds from 30 to 80 cm deep have been involved. The results are reported in Reference 6-9. They have provided a physical understanding of the quenching phenomena--the liquid entry into the bed is limited by the need of the vapor to exit from the bed via the top of the bed. If the vapor does not exit, pressure builds up in the bed and liquid is prohibited from flowing in. Thus, the vapor continually bubbles out of the bed as the liquid enters the bed, cools the debris, and produces more vapor.

The 1. or so dryout experiments that have been conducted are also rewet experiments, since dryout is not detected until a hot, dry portion of the bed is created. Explosive interaction of the hot debris and coolant has never been reported.

### c. A Simple Calculation

It can be calculated how much pressure is required to force an overlying pool of liquid into a 1273 K (1000°C) bed of  $\text{CO}_2$  without letting the vapor that is created by the quenching of the hot bed escape upward through the liquid pool. If the pool is forced into the top half of the 0.5-m-high debris bed (of porosity 0.35), the mass of liquid that will be vaporized and forced into the bottom half of the bed is about 1.1 kg. The ideal gas law can be used to predict that if this much vapor at 373 K (100°C) were forced into the bottom half of the bed, the pressure required would be 41,000 psi, or 2,843 atm.

The only method to obtain rapid mixing of hot debris with coolant is some forced entry of liquid into the bed. This cannot occur because of the need for the vapor produced by the quenching process to escape from the bed. If it does not escape, the bed will pressurize and prevent further entry of liquid. This is the natural limiting process seen in the quench experiments requiring that liquid enter the bed only as fast as the vapor can escape from the bed.



#### 6.4 REFERENCES

- 6-1 Y. P. Shylkov and S. N. Tsarevskii-Dyakin, "Turbulent Flow and Heat Exchange in Smooth Straight Channels of Any Cross-Section," Thermal Engineering, 13, pp. 90-96 (1966).
- 6-2 C. J. Hochanadel, "Radiation Chemistry of Water," Comparative Effects of Radiation, edited by Burton, Kirby-Smith, and Magee; (Wiley and Sons, Inc., New York, 1960).
- 6-3 E. Cerrai, F. Gadda, C. Ronchetti, and A. Scaroni, "Radiolysis of Steam-Water Mixtures: Effect of Steam Quality," Energia Nucleare, 16, pp. 768-774 (1969).
- 6-4 E. Bergeron, Uncertainties in DCC Coolability Predictions for Accident Analysis, (Albuquerque, NM: Sandia National Laboratories, to be published).
- 6-5 J. E. Gronager, M. Schwarz, and R. J. Lipinski, PAHR Debris Bed Experiment D-4, SAND80-2146 (Albuquerque, NM: Sandia National Laboratories, January 1981).
- 6-6 L. Barleon, K. Thomauske, and H. Werle, Particle Bed Experiment 82/2/3-3/15: Dryout Before Channel Penetration and Boiling-Induced, Irreversible Bed Changes, (KfK: Karlsruhe, FRG, June 1982).
- 6-7 V. X. Tung and V. K. Dhir, Quenching of a Hot Particulate Bed by Bottom Flooding, (Los Angeles, CA: UCLA)
- 6-8 I. Catton et al, An Experimental Study of Debris Bed Coolability under Pool Boiling Conditions, (Los Angeles, CA: UCLA)
- 6-9 D. Cho et al, Debris Bed Quenching Studies (Argonne, IL: Argonne National Laboratory)
- 6-10 T. Ginsberg et al, Transient Core Debris Bed Heat Removal Experiments and Analysis (Upton, NY: Brookhaven National Laboratory)

## 7. TEST AND FACILITY TECHNOLOGY

### 7.1 ACRR STATUS

This section contains comments on the general status of overall ACRR operation and remarks concerning experimental activities involving the ACRR.

The ACRR is operating normally in support of weapons program research and advanced reactor safety experiments.

DISTRIBUTION:

Division of Technical Information and Document Control  
NRC Distribution Contractor  
USNRC  
15700 Crabbs Branch Way  
Rockville, MD 20850  
(370 Copies for R3 and R7)

US Nuclear Regulatory Commission (4)  
Division of Accident Evaluation  
Office of Nuclear Regulatory Research  
Washington, DC 20555  
Attn: C. N. Kelber, Assistant Director  
Advanced Reactor Safety Research  
R. T. Curtis, Chief  
Analytical Advanced Reactor Safety Research, ARSR  
G. Marino, Chief  
Experimental Fast Reactor Safety  
R. W. Wright  
Experimental Fast Reactor Safety

R. W. Barber  
US Department of Energy  
Office of Nuclear Safety Coordination  
Washington, DC 20545

US Department of Energy (2)  
Albuquerque Operations Office  
PO Box 5400  
Albuquerque, NM 87185  
Attn: J. R. Roeder, Director  
Operational Safety Division  
D. L. Krenz, Director  
Energy Research & Technology Division  
For: C. B. Quinn  
R. N. Holton

T. Ginsberg  
Department of Nuclear Energy  
Bldg. 820  
Brookhaven National Laboratory  
Upton, NY 11973

University of Michigan  
Nuclear Engineering Department  
Ann Arbor, MI 48104

General Electric Corporation (3)  
Advanced Reactor Systems Department  
PO Box 3508  
Sunnyvale, CA 94088  
Attn: K. Hikido, Mgr., Safety Engineering - M/C S-18  
D. M. Switick, Mgr., Plant Safety  
M. I. Temme, Mgr., Probabilistic Risk Assessment

DISTRIBUTION (Continued):

W. E. Nyer  
P.O. Box 1845  
Idaho Falls, ID 83401

W. Tarbell  
K Tech Corp  
901 Pennsylvania NE  
Albuquerque, NM 87110

Projekt Schneller Brueter (4)  
Kernforschungszentrum Karlsruhe GMBH  
Postfach 3640  
D75 Karlsruhe  
West Germany  
Attn: Kessler (2)  
Heusener (2)

UKAEA Safety and Reliability Directorate (6)  
Wigshaw Lane  
Culcheth  
Warrington WA3 4NE  
Cheshire  
England  
Attn: Mr. J. G. Collier, Director  
Dr. M. J. Hayn  
Mr. E. V. Gilby  
Dr. R. S. Peckover

AERE Harwell (2)  
Didcot  
Oxfordshire OX11 0RA  
England  
Attn: Dr. J. Gittus, AETB  
J. R. Matthews, Theoretical Physics Division

UKAEA (2)  
Risley  
Warrington WA3 6AT  
Cheshire  
England  
Attn: B. Cowking, FRDD  
D. Hicks, TRDD

Dr. F. Briscoe  
Culham Laboratory  
Culham  
Abingdon  
Oxfordshire OX14 3DB  
England

DISTRIBUTION (Continued):

Mr. C. P. Gratton  
Division Head, SESD  
Atomic Energy Establishment (2)  
Winfrith,  
Dorset DTZ 8DH  
England

A. J. Manley  
EG&G Idaho, Inc.  
T.S.B.  
LWR Fuel Research Div.  
P.O. Box 1625  
Idaho Falls, ID 83415

K. S. Norwood  
Mail Stop B 12  
Bldg 4500 N  
Oak Ridge National Laboratory  
P. O. Box X  
Oak Ridge, TN 37830

Joint Research Centre (3)  
Ispra Establishment  
21020 Ispra (Varese)  
Italy  
Attn: R. Klersy  
H. Holtbecker  
P. Fasoli-Stella

Power Reactor & Nuclear Fuel  
Development Corporation (PNC) (3)  
Fast Breeder Reactor Development Project (FBR)  
9-13, 1-Chome, Akasaka  
Minato-Ku, Tokyo  
Japan  
Attn: Dr. Watanabe

Sandia National Laboratories  
1230 J. E. Powell  
1231 T. P. Wright  
1510 J. W. Nunziato  
1530 L. W. Davison  
1534 J. R. Asay  
1541 H. C. Hardee  
1830 M. J. Davis  
1840 R. J. Eagan  
1846 R. A. Sallach  
1846 R. K. Quinn  
2150 J. A. Hood  
3141 C. M. Ostrander (5)  
3151 W. L. Garner  
6310 T. O. Hunter  
6320 R. M. Jefferson

DISTRIBUTION (Continued):

6400 A. W. Snyder  
6410 J. W. Hickman  
6412 J. W. Hickman, acting  
6415 D. C. Aldrich  
6420 J. V. Walker (3)  
6420 M. M. Watkins  
6420A J. B. Rivard  
6421 T. R. Schmidt  
6421 K. R. Boldt  
6421 J. T. Hitchcock  
6421 G. W. Mitchell  
6421 C. A. Ottinger  
6422 D. A. Powers  
6422 J. E. Brockman  
6422 E. R. Copus  
6422 R. M. Elrick  
6422 J. E. Gronager  
6422 E. Randich  
6422 A. R. Taig  
6423 P. S. Pickard  
6423 A. C. Marshall  
6423 D. A. McArthur  
6423 K. Muramatsu  
6423 K. O. Reil  
6423 S. A. Wright  
6425 W. J. Camp  
6425 D. R. Bradley  
6425 J. E. Kelly  
6425 R. J. Lipinski  
6425 P. K. Mast  
6425 M. Pilch  
6425 A. Suo-Anttila  
6425 M. F. Young  
6427 M. Berman (5)  
6427 B. W. Marshall  
6427 L. S. Nelson  
6427 M. P. Sherman  
6427 S. R. Tieszen  
6427 C. C. Wong  
6430 N. R. Ortiz  
6440 D. A. Dahlgren  
6442 W. A. Von Rieseemann  
6449 K. D. Bergeron  
6450 J. A. Reuscher  
6451 T. Luera  
6452 M. Aker  
6453 W. J. Whitfield  
6454 G. L. Cano

DISTRIBUTION (Continued):

7100 C. D. Broyles  
7530 T. B. Lane (1)  
Attn: N. R. Keltner, 7537  
R. U. Acton, 7537  
T. Y. Chu, 7537  
7550 F. W. Neilson (1)  
Attn: O. J. Burchett, 7551  
J. H. Gieske, 7552  
8224 M. A. Pound

NRC FORM 328 (2-84) NRCM 1102 3201, 3202 <b>BIBLIOGRAPHIC DATA SHEET</b> SEE INSTRUCTIONS ON THE REVERSE		U.S. NUCLEAR REGULATORY COMMISSION 1 REPORT NUMBER (Assigned by TIDC add Vol No. if any) NUREG/CR- 3589 (2 of 4) SAND84-2425 (2 of 4)	
2 TITLE AND SUBTITLE Reactor Safety Research Quarterly Report April-June 1983 Vol. 26		3 LEAVE BLANK	
5 AUTHOR(S) Reactor Safety Research Department		4 DATE REPORT COMPLETED MONTH YEAR May 1984	
7 PERFORMING ORGANIZATION NAME AND MAILING ADDRESS (Include Zip Code) Sandia National Laboratories Albuquerque, NM 87185		6 DATE REPORT ISSUED MONTH YEAR July 1984	
10 SPONSORING ORGANIZATION NAME AND MAILING ADDRESS (Include Zip Code) Division of Accident Evaluation Office of Nuclear Regulatory Research USNRC Washington, DC 20555		8 PROJECT/TASK/WORK UNIT NUMBER 9 FIN OR GRANT NUMBER A-1016, etc.	
12 SUPPLEMENTARY NOTES		11a TYPE OF REPORT technical, quarterly b PERIOD COVERED (Inclusive dates) April-June 1983	
13 ABSTRACT (200 words or less) <p>Sandia National Laboratories is conducting, under USNRC's sponsorship, phenomenological research related to the safety of commercial nuclear power reactors.</p> <p>The overall objective of this work is to provide NRC a comprehensive data base essential to (1) defining key safety issues, (2) understanding risk-significant accident sequences, (3) developing and verifying models used in safety assessments, and (4) assuring the public that power reactor systems will not be licensed and placed in commercial service in the United States without appropriate consideration being given to their effects on health and safety.</p> <p>Together with other programs, the Sandia effort is directed at assuring the soundness of the technology base upon which licensing decisions are made.</p> <p>This report describes progress in a number of activities dealing with current safety issues relevant to both light water and breeder reactors. The work includes a broad range of experiments to simulate accidental conditions to provide the required data base to understand important accident sequences and to serve as a basis for development and verification of the complex computer simulation models and codes used in accident analysis and licensing reviews. Such a program must include the development of analytical models, verified by experiment, which can be used to predict reactor and safety system performance under a broad variety of abnormal conditions.</p> <p>Current major emphasis is focused on providing information to NRC relevant to (1) its deliberations and decisions dealing with severe LWR accidents, and (2) its safety evaluation of the proposed Clinch River Breeder Reactor.</p>			
14 DOCUMENT ANALYSIS - KEYWORDS/DESCRIPTORS b IDENTIFIERS/OPEN ENDED TERMS		15 AVAILABILITY STATEMENT unlimited 16 SECURITY CLASSIFICATION (This page) U (This report) U 17 NUMBER OF PAGES 166 18 PRICE	



ORG.	BLDG.	NAME	REC'D BY*	ORG.	BLDG.	NAME	REC'D BY*

120555070077  
 US NRC  
 ADM-DIV OF TIDC  
 POLICY & PUB MGT  
 W-501  
 WASHINGTON

IAN1R31R7  
 BR-PDR NUREG  
 DC 20555

